Receive Radio-Frequency Coils for a Parallel B_0 Linac-MR

by

Radim Barta

A thesis submitted in partial fulfillment of the requirements for the degree of

Doctor of Philosophy

in

Medical Physics

Department of Oncology
University of Alberta

Abstract

The rotating B_0 linac-MR is a new type of radiotherapy treatment machine that combines radiation delivery from a linear accelerator (linac) with a magnetic resonance imaging (MRI) system for real-time tumour tracking. This kind of combined technology aims to achieve tighter margins in cancer treatments with better tumour control and reduced damage to healthy tissue.

A combination system like the linac-MR still requires receive radio-frequency (RF) coils to capture MRI images before and during the treatment. All of the standard requirements, like high efficiency coils for high SNR images, apply for RF-coils for the rotating B_0 linac-MR. In addition, two additional design hurdles need to be considered: one, if RF-coils are in the path of the radiation beam, they will interact with the radiation to increase the radiation dose to the skin, and two, specific to the Alberta linac-MR design, the shared gantry of the main magnet and linac means the orientation of B_0 will change as the treatment beam angle changes, which also changes the orientation of the MRI's signal detection plane. RF-coils must be sensitive to this plane through 360° of linac rotation.

In this work the impact on surface dose due to copper and aluminum conductors of various thicknesses is investigated. The surface dose increase due to aluminum is three times lower than with copper of the same thickness. The increase in surface dose is determined to be linear with thickness below 25 micrometers. Beyond this, the surface dose increases more slowly and non-linearly with increasing thickness of conductor.

A further investigation looked at the resulting image quality penalty in terms of

signal-to-noise ratio (SNR) when using thin aluminum and copper conductors. This work investigates the practical limits for using thin conductors in RF-coils for the linac-MR. This work includes an experimental verification of the relationship between bench measured coil efficiency and the achieved image SNR, which is relevant in a variety of novel coil applications.

The second challenge, the rotating B_0, is investigated through a proposed solution which combines three orthogonal RF-coils into a three channel array. A single turn coil is combined with two figure-eight or butterfly coils. The butterfly coil consists of two D-shaped loops connected in parallel across a capacitor. The three coils are stacked in a pancake arrangement, with the two butterfly coils rotated 90° with respect to one another. The stack sits in the transverse plane adjacent to the patient and the butterfly coils are thus sensitive to the transverse plane. The vertical butterfly coil is primarily sensitive to magnetization along the patient anterior-posterior (AP) axis, while the horizontal butterfly coil is sensitive to magnetization along the patient left-right (LR) axis. The single turn coil is primarily sensitive to magnetization along the patient superior-inferior (SI) axis.

This array approximately maintains uniform SNR across all gantry angles (θ) of the rotating B_0 linac-MR, where the magnetic field B_0 rotates in the patient's transverse plane. Consequently, the SI axis is perpendicular to the transverse plane at all gantry angles and the magnitude of the component of transverse magnetization along the SI axis is also the same at all gantry angles. The signal received by the single turn coil is therefore constant across gantry angles. Each individual butterfly coil, however, will perform best when B_0 is perpendicular to its sensitive axis and worst when B_0 is parallel. The performance varies as the cross-product of B_0 and the sensitive axis: $\cos(\theta)$ for the horizontal butterfly coil and $\sin(\theta)$ for the vertical butterfly coil. Due to the identical structure, but 90° rotation of the two butterfly coils, the root sum of squares of the two butterfly coils is constant with θ. The sum of the two butterfly coils gives the component of magnetization in the transverse plane, thus combining it with the single turn coil, the array achieves quadrature-like reception with constant SNR at all gantry angles.

This work thus describes several essential elements of surface coils and surface arrays for the linac-MR. It describes how interactions between the radiation and the coils can be reduced without sacrificing image quality and how a combination of coils with orthogonal sensitive axes leads to uniform SNR across gantry angles in a rotating B_0 linac-MR.

Preface

This thesis is an original work by Radim Barta. A version of Chapter 3 detailing the effects of copper and aluminum on the surface dose in a magnetic field has previously been published as:

Barta R, Ghila A, Rathee S, Fallone BG, De Zanche N. Impact of a Parallel Magnetic Field on Radiation Dose Beneath Thin Copper and Aluminum Foils. Biomed. Phys. Eng. Express 2020;6:037002.

Also, a version of Chapter 4 describing the bench and imaging performance of thin copper and aluminum coils was previously published as:

Barta R, Volotovskyy V, Wachowic K, Fallone BG, De Zanche N, How Thin Can You Go? Performance of Thin and Non-copper RF Coil Conductors. MRM 2021 Apr;85(4):2327-2333.

For all the publications, I was responsible for collecting, producing, and analysing the data, as well as for the composition and writing of the manuscript. Dr. A. Ghila was a collaborator on the collection of data for the first manuscript. Dr V. Volotovskyy contributed RF-coil specific knowledge and constructed the pre-amplifiers used in imaging. Dr. N. De Zanche, and Dr. B. G. Fallone were supervisory authors, involved with the formulation of the research project, and with the review and editing of the manuscripts. Dr. K. Wachowicz and Dr. S. Rathee contributed their specific expertise and insight into imaging with the Alberta Linac-MR and measuring surface dose, respectively.

To Nicole who kept me motivated through what seemed like an endless degree. And to all our foster cats current, past, and especially those we have lost.

Acknowledgements

I would like to extend my gratitude to my supervisors Dr. De Zanche and Dr. Fallone. They both invested innumerable amounts of time and energy into my project, from helping me get started as a fresh Masters student, to challenging me to finish a quality thesis. This project would not be possible without them. I further would like to acknowledge my committee members for their support. Dr. Wachowicz for his support on operation of the Linac-MR, Dr. Rathee for his expertise on ion chamber and surface dose measurement, Dr. Sharp for his many insights into the physics theory and applications.

I want to extend special thanks to Dr. Ghila and Dr. Volotovskyy who acted as partners during my research. Dr. Ghila also provided much needed support and encouragement throughout my degree. Dr. Volotovskyy was a constant source of practical RF-coil advice and reminded me to rest and recover regularly even though he works too hard himself.

A further special thanks to Dr. Steciw and Dr. Schreiner, the arms length and external on my examination committee. Their evaluation and critical analysis of my manuscript challenged me to make my thesis a piece of work I can truly be proud of.

Additionally, I want to thank the whole team at the CCI and the UAlberta, it would take too long to list everyone who made this thesis possible and helped me maintain my sanity. My thanks go to my fellow graduate students, to the Graduate Student's Association, to all the medical physics professors, the machine shop, the linac-MR engineers, and many others.

I am also grateful to Dr. Mackenzie for taking a chance on me and giving me a

position in Grande Prairie where I could work full time and live with my wife while finishing my thesis. Dr. Mackenzie and the entire Community Oncology Medical Physics group have been an unexpected but critical support for me.

Many thanks to my parents, Pavel and Renata, who made it possible for me to even be doing this degree. Without their lifelong motivation and help, I would not have gotten to where I am. A special thanks to my dad, Pavel Barta, who made the amazing figures featured throughout my thesis. And to my brother Ben for the games to help me take real breaks now and then.

The completion of my dissertation would not have happened without the support of my wife, Nicole, and our cats: Sheena, Cassandra, Tina, Cassie, Sia, Sniff, Bigface, Chloe, Zoey, Noodle, all our fosters including Petra, Puff, Josie, Jenny, Littlefoot, Valentitna, Damacles, Dorian, Aslan, Fatima, Vanessa, Daphne, Farrah, Chartreuse, and those that are sadly not with us including Marble and Charcoal; I miss you dearly. My family is what got me through this degree. I love my family with all my heart; and I thank them for their support.

Table of Contents

List of Tables

List of Figures

List of Symbols

Constants

$\hbar$	Reduced Plank's constant	$1.05 \times 10^{-34}\,Js$
μ_0	Vacuum permeability	$1.26 \times 10^{6}\,H/m$
c	Speed of light in free space	$3.00 \times 10^{8}\,m/s$
h	Plank's constant	$6.62 \times 10^{-34}\,J/Hz$
k_B	Boltzmann's constant.	$1.380649 \times 10^{-23}\,J/K$
m_e	Rest mass of an electron.	$0.511\,MeV$
N_A	Avogadro's number	6.022×10^{23}
r_e	Classical electron radius	$2.82 \times 10^{-15}\,m$

Symbols

$(\frac{L}{\rho})$	Mass stopping power
α	RF-pulse flip angle
β	Ratio of dose to KERMA
δ	Small shift
ϵ	Electromotive force or emf
η	Efficiency of an RF-coil
$\frac{d\sigma}{d\Omega}$	Differential cross-section as a function of solid angle
γ	Gyromagnetic ratio

μ_{en}	Linear energy absorption attenuation coefficient
μ_{tot}	Linear attenuation coefficient
μ_{tr}	Linear energy transfer attenuation coefficient
ν	Frequency
ω	Angular frequency
ω_0	Larmor frequency
ω_s	Frequency of a resonant circuit
Φ	Photon beam energy fluence
ϕ	Phase shift
ϕ_B	Magnetic flux
ψ	Noise covariance matrix
Ψ_Q	Transmit efficiency
ρ_{eff}	Effective spin density
σ	Interaction cross-section
σ_{con}	Conductivity
θ	Angle of scatter or gantry angle
$\vec{\mu}_{nuc}$	Nuclear magnetic moment
$\vec{A}_{mag}$	Magnetic vector potential
$\vec{G}(\vec{r},t)$	Magnetic field gradient
$\vec{M}$	Magnetization density (vector)
$\vec{s}_{am}$	Spin angular momentum
A_M	Mass number
B	Magnetic field

B_0	Main magnetic field
B_1	RF excitation and receive fields
B_k	Magnetic field along $\hat{k}$
C	Capacitance
D	Dose
d	Depth
D_{max}	Maximal dose along central axis percentage depth dose.
d_{max}	Depth (cm) of D_{max}
dS	Infinitesimal surface segment
E	Energy
e^-	Electron
f	Inversion factor to describe initial position of longitudinal magnetization after an excitation
I_k	Data set for image k
i_{unit}	Unit current
K	Kinetic energy released per unit mass (KERMA)
k_i	Spatial frequency for the i axis
L	Inductance
M	Magnetization density (scalar)
M_k	Component of magnetization density along $\hat{k}$
N	Number of something, typically nuclei or atoms
n	Noise
P	Power

p	Pixel value
q	Charge
R	Geometry term in resistance components.
r	Resistance
S_p	Spatial term describing RF-coil geometric sensitivity to magnetization in the sample
S_L	A surface in space that is bounded by the loop defined by L
s_{rf}	Signal detected by an RF-coil
T	Temperature
t	Time
T_1	Spin-lattice relaxation time
T_2	Spin-spin relaxation time
T_2^*	Spin-spin relaxation time including decoherence due to B_0 inhomogeneity
TE	Echo time
TR	Repetition time
V	Volume
v	Velocity
X	Reactance
Y	Data set for a region of interest that is a subset of I_k
Z_A	Atomic number
Z_0	Characteristic impedance
Z_{coil}	Coil impedance
Z_{opt}	Optimal input impedance of an RF-amplifier

S_{11}	Return loss (scattering parameter)
S_{21}	Transmission or coupling (scattering parameter)

Abbreviations

rect Rectangular function.

sinc Sinc function.

ADC Analog to digital converter.

CPE Transient charged particle equilibrium.

CSDA Continuous slowing down approximation.

CT Computed tomography.

emf Electromotive force.

FT Fourier transform.

IFT Inverse Fourier transform.

IS Inverse-square factor.

Linac Linear accelerator.

Linac-MR/MR-linac Combination of a linear accelerator and magnetic resonance imaging system.

MLC Multi-leaf collimator.

MRI Magnetic resonance imaging.

MRIgRT Magnetic resonance imaging guided radiation therapy.

PCB Printed circuit board.

PDD Percentage depth dose.

PET Positron emission tomography.

PET-MRI Combination PET and MRI system.

ppm Parts per million.

RF Radio-frequency.

RIC Radiation induced current.

ROI Region of interest.

RT Radiation therapy.

Rx Receive.

SNR Signal-to-noise Ratio.

SSD Source-to-surface distance.

TCPE Transient charged particle equilibrium.

TE Echo time.

TR Repetition time.

Tx Transmit.

VNA Vector network analyzer.

Chapter 1

Introduction and Background

1.1 Cancer

Cancer is the leading cause of death in Canada[1]. It impacts all of us, whether it is a personal experience or that of a family member. Approximately two in five Canadians will get cancer at some point in their life and one quarter of Canadians will die as a consequence of their cancer[2]. Cancer is a grouping of various diseases, with diverse underlying causes with the common manifestation of uncontrolled cellular growth[3]. Cancer impacts all demographics, from children to the elderly, across the spectrum of individual diversity[2].

Cancer treatment focuses on trying to eliminate cancer cells or arresting their uncontrolled growth. Identified solid growths of cancer cells are called tumours. Cancer can also be found diffusely throughout a patient, for example blood cancers typically don't form large solid tumours[3].

The challenges of cancer are detection, diagnosis, and treatment. Detection occurs during regular medical check-ups, or when a patient shows tumour symptoms arising from disruption of normal tissue and organ function. Diagnosis is typically validated through biopsy to confirm that the tumour or diffuse cellular growth is cancerous. Treatment usually consists of some combination of surgery, radiation therapy, and/or chemotherapy.

The goal of cancer treatment is to force the cancer into remission, which is when a patient no longer experiences significant symptoms of the disease. The high 10 year survival rate of some cancers (90% for prostate and 82% for female breast) speaks to the strength of the expertise and technology that are now available. However, it is clear that improvements in treatments are needed; for example, lung and bronchus cancers, the second most common cancers, come with a crushing prognosis: a 10 year survival rate of only 15%[4].

1.1.1 Cancer Imaging

Cancer imaging is a dynamic and evolving field. Having quality images for treatment planning is absolutely essential for radiotherapy. It is vital for detection and treatment of cancer, and plays an important role in diagnosis as well. Magnetic Resonance Imaging (MRI) plays an increasingly important role in cancer treatment. It is used alongside other modalities like Computed Tomography (CT) and Positron Emission Tomography (PET) to identify and locate cancer in the body, and distinguish it from healthy tissue.

MRI is valuable because it is non-invasive, does not use ionizing radiation, and offers a range of contrast mechanisms for soft tissue imaging. It is used to detect suspected cancers and aid in diagnosis of cancers based on the appearance of abnormalities[5–7]. MRI can also be used alongside CT to delineate the tumour from healthy tissue for planning surgery or radiation therapy[6, 8–10]. MRI further plays an important role in evaluating treatment response, such as determining tumour shrinkage or detecting recurrence months and years following treatment. New approaches also allow for MRI based treatment planning for radiation therapy[6]. At the present CT is the primary modality used for planning radiotherapy, but MRI in combination with CT is becoming more common and MRI alone can be used exclusively in some cases[6, 8, 9].

1.1.2 Radiation Therapy

Up to half of all cancer treatments include some form of radiation therapy, the majority of which is external beam radiation therapy[11]. In external beam radiation therapy, the tumour cells are damaged by delivering radiation to the tumour from a source outside the patient, typically a linear accelerator. Radiation, typically in the form of photons, is directed at the tumour by shielding healthy tissue and the environment. The radiation beam (the collection of unblocked photons) strikes the patient delivering dose (energy per mass) along its path of travel. The beam loses energy (attenuates) as it travels through tissue and deposits energy, leading to a decrease in dose with depth. Additionally, photons transfer energy indirectly to tissue by exciting electrons and ionizing atoms, and as a result the dose reaches a maximum a short depth into the patient rather than at the surface. The initial rise of dose with depth is called *build-up*.

By applying multiple radiation beams from multiple points on an arc centered on the tumour, dose is added to the tumour by each beam, while healthy tissue is irradiated only with a few of the beams. The goal is to deliver enough dose to cause irrepairable damage the cancerous cells, but deliver small enough dose to healthy tissue, so that the healthy tissue is spared, meaning it can repair itself and continue to function.

1.2 Linac-MR

The linac-MR or MR-linac is a novel technology that combines a linear accelerator (linac) and a magnetic resonance imaging system for the delivery of real-time adaptive image-guided radiation therapy. The fact that several such systems are being developed around the world [12–16] emphasizes the importance and potential benefit of such systems. These systems aim to achieve MR guided radiation therapy (MRgRT) to ensure accuracy of treatment delivery that considers intra-fraction movement.

This will spare the maximum normal tissue when boosting dose to the target. These systems are expected to provide patients with improved quality of life and treatment outcomes. The linac-MR is equipped to treat patients in fewer fractions, like in escalated dose gated SBRT treatments, and in the future will allow the patient's tumour to be visualized and tracked each day, potentially speeding up treatments by eliminating the need for gating with tracked treatment. Active areas of linac-MR research include measuring and calculating dose deposition in a magnetic field[17–20], rapid imaging and tumour tracking[21, 22], and more.

1.2.1 Categories of Linac-MR

Linac-MR systems can be categorized as either parallel or perpendicular, depending on whether the main magnetic field (B_0) is aligned with the axis of the radiation beam or perpendicular to it (Figure 1.1). The Alberta Linac-MR (same design is used by the Aurora RT from MagnetTx)[12, 23] and the Australian MRI-Linac[15, 24] are examples of parallel systems. For the Alberta Linac-MR, the entire MRI scanner and linac are mounted on a gantry to allow the treatment beam to rotate around the treatment couch. The system has a 0.56 T magnet and a 6 MV unflattened beam with a dose rate of 600 cGy/min at isocenter. In the Australian system, the linac and MR are fixed and the patient is rotated to achieve different delivery angles. The Australian system uses a 1.0 T magnet and a linac that can generate 4 MV and 6 MV unflattened photon beams[24]. In both cases the main magnetic field is generated by the current in a pair of superconducting coils mounted on pole plates with the field pointing from one pole to the other. The linear accelerator is mounted exterior to one of the poles, delivering radiation through a hole in the pole plate (Figure 1.1). The photon beam is thus parallel to the main magnetic field.

In perpendicular systems, the radiation beam axis and the main magnetic field are perpendicular (Figure 1.1). Two commercially available MR-linacs, Electa Unity MR-Linac [13] and the MRIdian ViewRay MRI-guided Linac[25], are both perpendicular

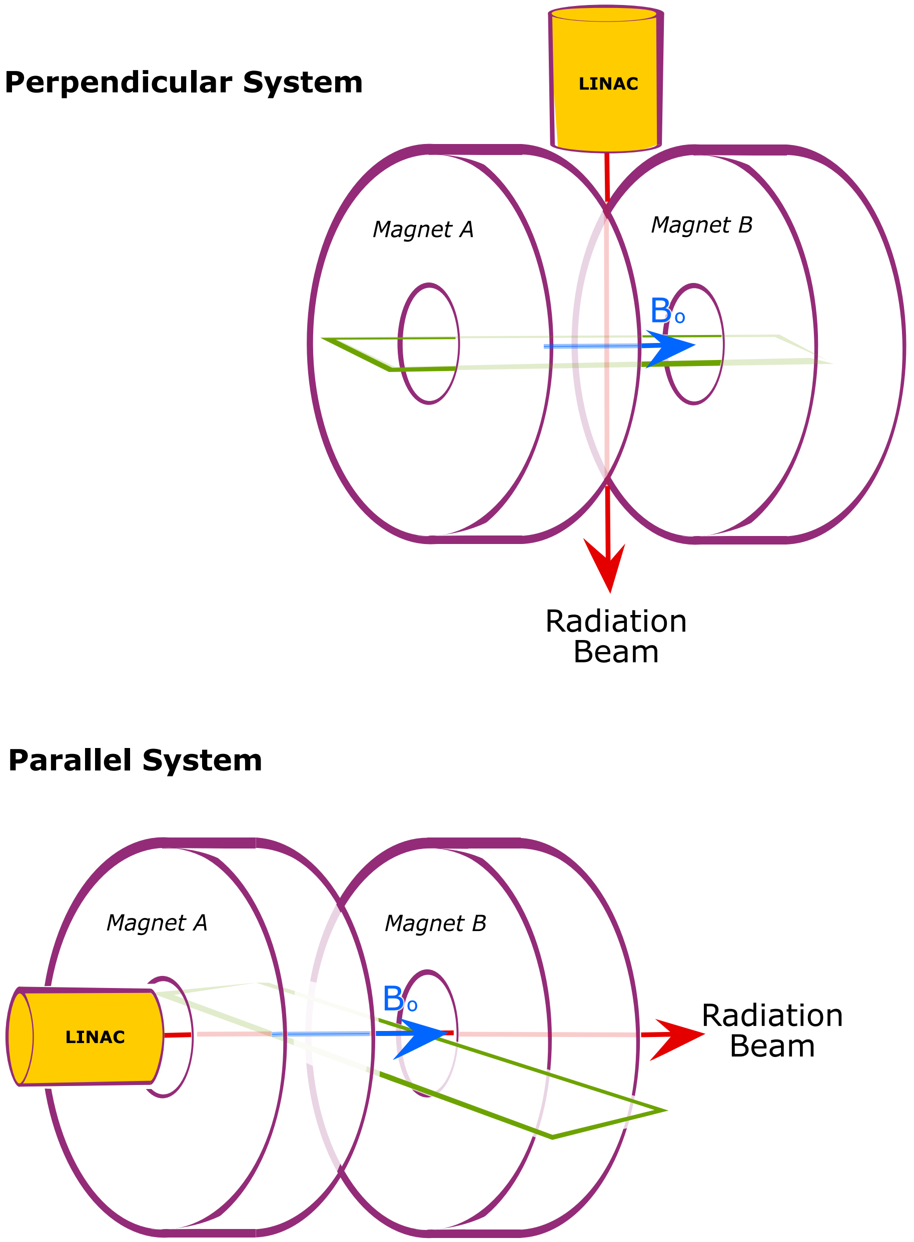

Perpendicular System

Parallel System

Figure 1.1: A comparison of a perpendicular arrangement of magnetic field and linear accelerator (top) and a parallel arrangement of the magnetic field and the linear accelerator (bottom).

systems. The Unity system consists of a 1.5 T cylindrical bore solenoid magnet (B_0 parallel to the bore axis) with a 7MV linac mounted on a gantry that rotates around the cylinder surface at the center of the bore[13]. The 7MV linac is an unflattened beam and has a reported isocenter dose rate of 350 cGy/min at isocenter [26]. The ViewRay system has a 0.35 T magnetic field generated by two donut magnets and in the gap between them a gantry holds a 6MV linac that can rotate around the patient[25]. The 6MV linac is an unflattened beam with up to 600 cGy/min at isocenter[25].

The orientation of the magnetic field with respect to the radiation beam leads to dosimetric differences from non-MR linac systems. Electrons, because they are charged particles, experience a Lorentz force when travelling through a magnetic field which causes them to curve along a helical path (see Section 2.2.2.2).

In parallel systems electrons traveling at an angle to the main magnetic field will follow a helical path whose radius is dictated by the perpendicular velocity of the electron and the strength of the magnetic field. In the patient, this leads to a slight confinement of the dose towards the central axis, reducing the penumbra. The amount of perturbation from the situation without a magnetic field depends on the strength of the magnetic field, with stronger fields leading to more confinement of dose. In lung, the presence of a parallel 0.5 T magnetic field showed a 10% increase in dose in the beam, and had hot spots where dose increased up to 20% compared to the 0 T magnetic field case [27]. In the air on the entrance side, the curved path reduces the lateral scatter of electrons, trapping a portion of them within the treatment field, resulting in an increased the dose to the skin in the treatment field. If the magnetic field extends significantly into the head of the linac, where electrons are readily produced as the beam strikes collimating structures, the surface dose increase can be significant[17, 28]. On the exit side of the patient, there is minimal difference between parallel systems and zero-magnetic field systems. The electrons exiting the patient will travel in helical or straight paths away from the patient, respectively.

In perpendicular systems, the Lorentz force acts to curve the component of the electron velocity along the beam axis. From the perspective of an electron traveling along the beam axis, with the magnetic field left to right, the electron will feel deflected upwards. In the patient, this results in a shifted dose deposition relative to treatment in the absence of a magnetic field, and can lead to hot spots and cold spots, especially at tissue boundaries. At 0.5 T in lung, in terms of relative dose difference, the hot and cold spots are up to ± 20% compared to the zero-magnetic field dose distribution[27]. On the entrance side, the electrons curve along an arc whose radius is set by the electron energy and the strength of the magnetic field. Electrons originating further from the surface than this radius will curve away from the surface and will not contribute to patient skin dose. Thus in a perpendicular system, there is no entrance surface dose increase due to the magnetic field. There may even be a decrease in the entrance dose. On exit surfaces, however, electrons generated in the patient that would normally travel away from the patient, will now be curved by the main magnetic field to strike the patient's exit surface. This can lead to significant and unacceptable dose increases on the exit surface that must be mitigated[29–31].

1.2.2 RF-Coils for Imaging on a Linac-MR

For all MRgRT systems their imaging capabilities are a key piece of the design, because without imaging there is no guidance. MR images are acquired by capturing the rotation of magnetization in a magnetic field with RF-coils (see Section 2.1). RF-coils designed specifically for these systems are under development. Early studies investigated the feasibility of using conventional RF-coils and found that while the impact on the treatment region from traditional arrays was minimal[32], there was a large impact on the surface dose[33], raising concerns about skin reactions. In other studies, image SNR reduction were noted due radiation induced current (see Section 2.1.7) generated when radiation struck the conductors of RF-coils during imaging[34, 35]. Potential solutions were proposed in each case. A common solution to both is to design "open" RF-coils that are positioned outside of the radiation beam at all times during treatment. This method has been employed successfully in several systems[36, 37].

When collisions between the coil and beam cannot be avoided the interaction between the radiation beam and the RF-coil must be analyzed. There is a proposed software algorithm that can recover some of the RIC based SNR loss associated with in-beam designs. For a typical linac-mr imaging sequence and a 3 cm diameter solenoid coil, the algorithm reduced the SNR loss due to a 250 MU/min radiation beam from 17% SNR loss to 11% SNR loss[35]. At a given field strength, when the dose rate is increased, RIC increases, and leads to larger SNR losses. When RIC remains constant, however, at higher field strengths, RIC SNR loss is reduced as the MRI signal is increased at larger field strengths[31]. For in-beam design there is also a need to reduce the impact on surface dose. Mitigation of the surface dose increase caused by surface RF-coils depends on the relative orientation of the radiation beam and the magnetic field (Section 2.2.2.2).

For both parallel and perpendicular Linac-MR systems, surface RF-coils that are positioned directly on a patient will increase the surface dose. The build-up of dose begins in the RF-coils increasing the surface dose [33] (see Section 2.2.5 and Chapter 3).

For both parallel and perpendicular systems the surface dose increase due to RF-coils in the beam can be mitigated with out-of-field RF-coils. In this case there is no build-up that would increase the surface dose. This approach has been used in the Australian MRI-Linac project [37] and is explored in Chapter 5 of this PhD work as well. A challenge with this approach is that the distance between the coil and the imaging target is larger, reducing the potential maximum SNR (see Section 2.1.1).

The curving of electrons in a magnetic field (see Section 2.2.2.2) leads to a mitigation option that is only available for perpendicular systems. With the perpendicular arrangement of the radiation beam and the magnetic field, the surface dose increase from in-beam RF-coils can be mitigated by introducing an air gap between the coil and the patient surface[31, 33]. Electrons excited in the RF-coil are curved and with a sufficient gap will not strike the patient. The same mitigation is not seen in the parallel linac-MR system, since the Lorentz force in the airgap does not act on the component of the electron's velocity that is directed towards the patient surface[33]. RF-coils for a parallel Linac-MR that are in the beam must be made such that they minimally interact with the radiation beam. This thesis explores how this could be achieved with thin copper and aluminum conductors (see Chapter 3) and whether usable coils are even possible with such conductors (see Chapter 4).

1.2.3 Rotating B_0 Linac MR

As was highlighted, a unique aspect of the parallel rotating B_0 Alberta linac-MR is the rigid co-rotation of the magnet and the linac. In conventional MRI systems the fixed B_0 means the rotation (precession) of the magnetization is in a single plane. The changing magnetic field of the rotating magnetization can be detected with coils that are only sensitive to that plane. The rotating B_0 linac-MR, however, has a plane of rotation that is at a different angle depending on the angle of the gantry holding the magnet and the linac. Only the axial component of the two-dimensional rotation plane is constant with gantry angle.

For optimal image quality, it is desirable to detect both components of the precessing magnetization, which is known as quadrature reception (see Section 2.1.5). The RF-coil with quadrature-like detection for the linac-MR must be sensitive to signal in all the planes of precession that exist for a 360° rotation of the gantry. This challenge is explored in Chapter 5.

1.2.4 Motivation and Outline of Thesis

As outlined, there is a critical need for development of RF coils for the linac-MR and specifically for the unique challenges of the rotating B_0 linac-MR. The main goals of

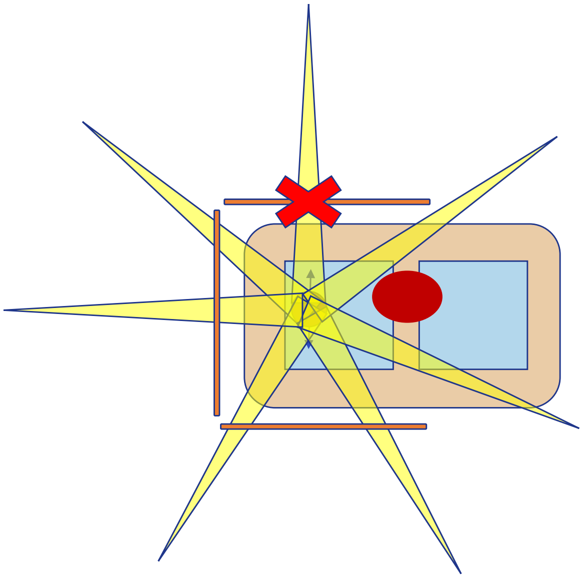

Figure 1.2: This is a depiction of a patient being treated in a parallel linac-MR. A patient cross-section with heart in red and lungs in light blue is shown. A small moving tumour is the target in the left lung. To image the tumour, coils (orange) are arranged on the patient surface. The treatment is delivered through a series of radiation beams (yellow) from different angles. One of the main goals of this thesis is to investigate the type of RF-coil materials that can be placed in the beam while avoiding a large increase in surface dose.

the work presented in this thesis are to determine how to mitigate the surface dose increase from surface RF-coils (Figure 1.2) and to develop a system of RF-coils that achieves good image quality using quadrature-like detection for the situation where the B_0 field is rotating along with the radiation gantry during treatment (Figure 1.3).

This thesis begins with the background theory of MRI and radiation in Chapter 2. The first goal is tackled in earnest through two published papers one on the topic of surface dose below copper and aluminum in Chapter 3 and one on the topic of image quality achieved with coils using thin copper and aluminum conductors in Chapter 4. The second goal is addressed in an unpublished paper on a RF-coil array for gantry angle independent imaging on the rotating B_0 linac-MR in Chapter 5. The thesis concludes with a summary of the key results, a look at applications of this work, and future avenues for research flowing from this thesis in Chapter 6 and Chapter 7.

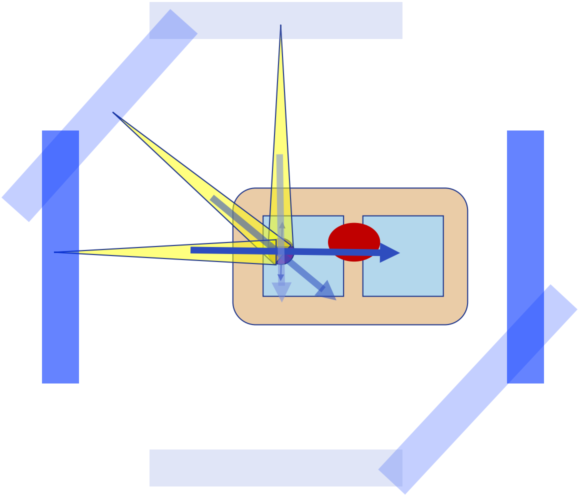

Figure 1.3: Depiction of a patient (cross-section with heart in red and lungs in light blue) being treated in a parallel linac-MR. A small tumour in the lungs is treated through a series of radiation beams (yellow) from different angles. The rotation of the superconducting coils (blue rectangles) that generate the main magnetic field, B_0 (blue arrows) is explicitly shown. The second main goal of this thesis is to investigate what kind of RF-coil design will allow quadrature-like detection of the MR signal independent of the magnetic field orientation.

Chapter 2

Theory

2.1 Magnetic Resonance Imaging

2.1.1 MRI Basics

Magnetic resonance imaging is a non-invasive form of diagnostic imaging. It is based on the phenomenon of nuclear magnetic resonance (NMR) which is observed in nuclei of atoms with a nuclear magnetic moment ($\vec{\mu}_{nuc}$). When a magnetic moment in a strong magnetic field is tipped from its equilibrium state (aligned with the magnetic field), it begins to precess, rotate about the main magnetic field. Since this is a small rotating magnet, it induces an alternating voltage in nearby conductors at a frequency that matches the rate of precession. Nuclear mangetic resonance is observed for nuclei that have an odd number of protons and/or neutrons as they have net spin angular momentum ($\vec{s}_{am}$) and the nuclear magnetic moment is then related by the gyromagnetic ratio (γ) unique to each nuclear species by:

$$\vec{\mu}_{nuc} = \gamma \vec{s}_{am} \tag{2.1}$$

If there are even numbers of protons and neutrons (all nucleons are paired) then the spins of all the nucleons sum to a net-zero spin, and have no nuclear magnetic moment.

The most common such nucleus in the human body is the ^{1}H-hydrogen proton found plentifully in dihydrogen oxide (H_2O or water) and other compounds in the body. Considering a large number of nuclei as a group, the relevant property is the net sum of their nuclear magnetic moments, which is a sample's magnetization per volume ($\vec{M}$). When a sample is placed in a constant external magnetic field (B), the constituent nuclei will tend to align with the magnetic field as it is the lowest energy state, but the thermal energy available to the system means the net magnetization is very small. At clinically relevant temperatures (T) the net magnetization is given by the Rayleigh and Jeans approximation [38] or Curie formula [39]:

$$M[A/m] = \frac{N}{V}\frac{\gamma^2 B\hbar^2}{4k_BT} \tag{2.2}$$

where N/V is the density of nuclei, γ is the gyromagnetic ratio, $\hbar$ is the reduced Plank constant, and k_B is the Boltzmann constant.

Key insights from this result are that the magnetization is proportional to the field strength and the magnetization depends on the nucleus of interest based on its gyromagnetic ratio. Notably, thermally-polarized MRI does not have particularly high sensitivity, because the effective number of excess nuclei is 70 ppm at room temperature and 1 tesla [T]. However, MRI is still an excellent imaging modality due to the incredible number of hydrogen nuclei in the human body (i.e., 6×10^{23} hydrogen nuclei for every 9 grams of water).

Detecting magnetization relies on the inherent angular momentum of the nuclei. If the magnetization is tipped away from alignment with B_0 (the process will be discussed later), the magnetic moments that make up the magnetization will feel a force due to B_0. By conservation of spin angular momentum ($\vec{s}_{am}$), the magnetic moments, and hence the magnetization, will experience a torque, and thus begin to precess about the B_0 axis. The evolution of the magnetization is described by the Bloch equations[39].

$$\frac{d\vec{M}}{dt} = \gamma\vec{M} \times \vec{B_0} \tag{2.3}$$

This relationship describes how magnetization will behave in a constant external magnetic field in the absence of relaxation. Without loss of generalization let B_0 be along the z-axis, and expand out in Cartesian co-ordinates.

$$\begin{aligned} \frac{dM_x}{dt} &= \gamma M_y B_0 \\ \frac{dM_y}{dt} &= -\gamma M_x B_0 \\ \frac{dM_z}{dt} &= 0 \end{aligned} \tag{2.4}$$

We can decouple the x and y components by taking a second time derivative and obtain the harmonic equations:

$$\begin{aligned} \frac{d^2M_x}{dt^2} &= -\gamma^2 B_0^2 M_x \\ \frac{d^2M_y}{dt^2} &= -\gamma^2 B_0^2 M_y \end{aligned} \tag{2.5}$$

Hence:

$$\begin{aligned} M_x(t) =& M_x(0)\cos(\gamma B_0 t) + M_y(0)\sin(\gamma B_0 t) \\ M_y(t) =& M_y(0)\cos(\gamma B_0 t) - M_x(0)\sin(\gamma B_0 t) \\ M_z(t) =& M_z(0) \end{aligned} \tag{2.6}$$

This describes the precession of the transverse magnetization (M_x and M_y) about the z-axis. The components of the magnetization perpendicular to the external magnetic field rotate around it, while the component in alignment with the external magnetic field is constant. The frequency of rotation of the perpendicular components is constant and given by the product of the gyromagnetic ratio and the magnetic field. This is the Larmor frequency:

$$\omega_0 = \gamma B_0 \tag{2.7}$$

This frequency ω_0 is not coincidentally the same as the frequency of the energy transition between high and low energy spin states of individual nuclei.

In reality, interactions between individual nuclei and between nuclei and their environment causes the net magnetization to relax back towards the equilibrium where the magnetization is aligned with the magnetic field. The transverse magnetization

(M_x and M_y) will decay over time to zero and the parallel magnetization (M_z) will recover to the equilibrium state (M_0) with magnitude given by Equation (2.2). This decay and recovery is typically approximated as exponential.

The rate of recovery of the M_0 is described by the time constant T_1. T_1 is the spin-lattice relaxation time constant and describes the return of the excited spins back into thermodynamic equilibrium with their environment. It depends on the interactions between individual nuclei (the spins) and the atoms that are not a part of the magnetization (the lattice). The rate of decay of the transverse magnetization is described by the time constant T_2. T_2 is the spin-spin relaxation time constant, and it describes the loss of coherence of magnetic moments due to local magnetic field effects and exchange of energy with other spins. A related constant T_2^* is a shorter relaxation time constant that describes the same loss of coherence, but also includes the effects of dephasing due to B_0 inhomogeneity. The use of spin echoes in MRI allows capturing of magnetization decaying with the T_2 time constant (see Section 2.1.6.1); however, if a sample is simply excited and detected, the signal will fall off at the rate of the T_2^* time constant.

A full description of magnetization under the influence of a time varying external magnetic field that is along the z-axis at equilibrium, is given by the full Bloch equations where terms for T_2 (assumes perfectly homogeneous B_0) and T_1 have been added to the z-axis and transverse components of magnetization[39].

$$\begin{aligned} \frac{dM_z}{dt} &= \gamma(\vec{M}(t) \times \vec{B}(t))_z - \frac{M_z(t) - M_0}{T_1} \\ \frac{dM_x}{dt} &= \gamma(\vec{M}(t) \times \vec{B}(t))_x - \frac{M_x(t)}{T_2} \\ \frac{dM_y}{dt} &= \gamma(\vec{M}(t) \times \vec{B}(t))_y - \frac{M_y(t)}{T_2} \end{aligned} \tag{2.8}$$

Solving this system as done above in Equation (2.6) for a constant magnetic field (B_0) along the z-axis with initial transverse magnetization $\vec{M}_i = (0, M_i, \sqrt{M_0^2 - M_i^2})$, $M_i <$

M_0 gives:

$$\begin{aligned} M_x(t) =& M_i \cos(\omega_0 t) e^{\frac{-t}{T_2}} \\ M_y(t) =& - M_i \sin(\omega_0 t) e^{\frac{-t}{T_2}} \\ M_z(t) =& M_0 (1 - f e^{\frac{-t}{T_1}}) \\ f =& 1 - \frac{\sqrt{M_0^2 - M_i^2}}{M_0} \end{aligned} \tag{2.9}$$

Where M_0 is once again the equilibrium magnetization and f is the inversion factor for a given excitation depending on the initial and equilibrium magnetization(Equation (2.2)).

It can be helpful to set $\hat{x}$ to 1 and $\hat{y}$ to j to form a complex variable M_{xy} where:

$$\begin{aligned} M_x =& Re(M_{xy}) \\ M_y =& Im(M_{xy}) \end{aligned} \tag{2.10}$$

The solution given in Equation (2.9) can then be written as:

$$\begin{aligned} M_{xy} =& M_i e^{-j\omega_0 t} e^{\frac{-t}{T_2}} \\ M_z =& M_0 (1 - f e^{\frac{-t}{T_1}}) \end{aligned} \tag{2.11}$$

In either form, the solution to the Bloch equations describes how the transverse magnetization (xy-plane component) undergoes precession at ω_0, and the longitudinal magnetization (along z) recovers towards M_0. As $t \to \infty$ we see that M_0 aligns along the z-axis as expected. These equations are valid for groupings of magnetization that experience the same magnetic field evolution. When determining contributions of magnetization from across a range of environments (e.g., spatial locations), as occurs in reception, the net effect is found by integrating the magnetization evolution (at each point) over the entire volume.

2.1.2 MR Signal Detection

The precession of the net magnetization vector is a changing magnetic field generated by the sample that is dependent on the density of the magnetic moments. This changing magnetic field can be detected using Faraday's Law, which describes the electromotive force or emf (ϵ) generated in a conductive loop in response to a changing magnetic flux (ϕ_B)[39, 40].

$$\epsilon_{loop} = -\frac{d\phi_B}{dt} \tag{2.12}$$

If a loop of wire is positioned near the subject being imaged, the precession of the magnetization will result in a flux through the loop that changes with time, inducing a measurable voltage in the wire. The induced voltage in the loop of wire is related to the magnetization available in the sample. The flux through the loop of wire is determined by integrating the magnetic field over a surface bounded by the loop (S_L)[40].

$$\phi_B = \int_{S_L} \vec{B} \cdot d\vec{S} \tag{2.13}$$

The magnetic field ($\vec{B}$) can be described as the curl of some magnetic vector potential ($\vec{A}_{mag}$) that is defined so that $\nabla \times \vec{A}_{mag} = \vec{B}$[40]:

$$\phi_B = \int_{S_L} (\nabla \times \vec{A}_{mag}) \cdot d\vec{S} \tag{2.14}$$

This allows us to change the integral from one over a surface to one along the loop[40]:

$$\phi_B = \int_{L} \vec{A}_{mag} \cdot d\vec{L} \tag{2.15}$$

The vector potential can be related to magnetization from Maxwell's equations by[40]:

$$\vec{A}_{mag}(\vec{r}, t) = \int_{\mathbb{R}^3} d^3\vec{r'} \frac{\mu_0}{4\pi} M(\vec{r'}, t) \times \vec{\nabla} \left(\frac{1}{\left| \vec{r'} - \vec{r} \right|} \right) \tag{2.16}$$

We combine Equation (2.14) and Equation (2.16), then change the order of integration, while noting magnetization does not exist outside our volume to get the following[40]:

$$\phi_B = \int_V d^3\vec{r'} \vec{M}(\vec{r'}, t) \cdot \frac{\mu_0}{4\pi} \int_L \vec{\nabla} \left(\frac{1}{\left| \vec{r'} - \vec{r}_l \right|} \right) \times d\vec{l} \tag{2.17}$$

The first term depends on the geometric distribution of the magnetization in the sample and the time evolution of this magnetization accounts for the changing magnetic field that induces a signal in our conductive loop. The second term, however, does not vary in time if the patient, B$_0$, and loop of wire, which in MRI is the radio-frequency (RF) coil (Section 2.1.5), do not move relative to one another during the imaging session. We can simplify the equation by introducing a constant spatial term, $\vec{S}_p$.

$$\vec{S}_p(\vec{r'}) = \frac{\mu_0}{4\pi}\int_L \vec{\nabla}\left(\frac{1}{\left|\vec{r'} - \vec{r}_l\right|}\right) \times d\vec{l} \tag{2.18}$$

The emf induced is then given by[40]:

$$\epsilon_{loop} = -\int d^3\vec{r'}\frac{d\vec{M}}{dt}\cdot\vec{S}_p(\vec{r'}) \tag{2.19}$$

Taking a derivative of Equation (2.11):

$$\begin{aligned}\frac{dM_{xy}}{dt} =& -j\omega_0 M_i e^{-j\omega_0 t}e^{\frac{-t}{T_2}} - \frac{M_i}{T_2}e^{-j\omega_0 t}e^{\frac{-t}{T_2}}\\ \frac{dM_z}{dt} =& \frac{M_0 f}{T_1}e^{\frac{-t}{T_1}}\end{aligned} \tag{2.20}$$

For common relaxation rates in the ms range and longer, the terms not containing ω_0 are at least 1000 times smaller than the terms with ω_0. The above then simplifies to:

$$\begin{aligned}\frac{dM_{xy}}{dt} \approx& -j\omega_0 M_i e^{-i\omega_0 t}e^{\frac{-t}{T_2}} = -j\omega_0 M_{xy}\\ \frac{dM_z}{dt} \approx& 0\end{aligned} \tag{2.21}$$

Hence the induced voltage is given by:

$$\epsilon_{loop} = -j\omega_0\int d^3\vec{r'}\vec{M}_{xy}\cdot\vec{S}_p(\vec{r'}) \tag{2.22}$$

Note that the introduction of a factor of $-j = e^{-j\frac{\pi}{2}}$ is simply a phase shift between the induced voltage and the magnetization.

The signal (emf) in MRI is proportional to the resonant frequency, the magnetization, and the spatial term. Considering that the maximum transverse magnetization is available when all of the equilibrium magnetization M_0 is excited, the signal available in MRI for a unitary spatial term can be determined by combining Equation (2.7) and Equation (2.22), resulting in:

$$\epsilon_{loop,max} = \frac{N\gamma^3 B^2 \hbar^2}{4k_B T} \tag{2.23}$$

The spatial term is primarily dominated by the distance between the magnetization and the conductive loop ($\vec{r}_l$ in Equation (2.17)). And in fact the spatial term can be thought of as the magnetic field generated at $\vec{r'}$ by the conductive loop, L, for a unit current, i_{unit}.

$$\vec{S}_p(\vec{r'}) = \frac{\vec{B}(\vec{r'})}{I} = \frac{\mu_0}{4\pi i_{unit}} \int_L \vec{\nabla} \left(\frac{I}{\left| \vec{r'} - \vec{r}_l \right|} \right) \times d\vec{l} \tag{2.24}$$

This spatial term is identical in form to the term that shows up in excitation of magnetization (Equation (2.25)), which reflects the reciprocal relationship between detection and excitation in MRI.

2.1.3 MR Signal Excitation

Consider some conductive loop L with an alternating current (I) flowing through it. The alternating current induces a changing magnetic field, B_1, which can be used to tip the magnetization. The magnetic field is given by

$$\vec{B_1}(\vec{r}) = \frac{\mu_0}{4\pi} \int_L \vec{\nabla} \left(\frac{i_{unit}}{\left| \vec{r'} - \vec{r}_l \right|} \right) \times d\vec{l} \tag{2.25}$$

The field generated depends on the spatial geometry of the coil in the exact same manner as the spatial term of the emf equation ($\vec{S}_p i_{unit} = \vec{B_1}$). This reciprocity can be exploited in evaluating RF-coils in the lab, as measuring the fields generated by an RF-coil tells us its detecting properties as well[41]. Another take away from the spatial term is that the coupling between the sample and coil, for both excitation and reception, will decrease with increased distance between them. Depending on the coil design, the shape of the fall-off will vary but some inhomogeneity will always be present.

By driving a coil with a current at the Larmor frequency, an alternating magnetic field, B_1, is generated. Since the frequency is commonly in the radio-frequency range, it is typically referred to as an RF-field, distinguishing it from the static main magnetic field B_0. The net magnetic field experienced by the magnetization is the vector sum of the B_0 field and the B_1 field. By precisely tuning the frequency and leaving the B_1 on for a precise amount of time, the magnetization can be rotated to form any desired angle between the magnetization and B_0, such as rotating it fully into the transverse plane.

As the B_1 field is typically applied only for a short time (e.g., 1 ms), for simplicity we consider the Bloch equations (Equation (2.3)) with $T_1, T_2 \to \infty$. The magnetic field during excitation is described by $\vec{B} = \langle B_1(t) \cos \omega_{rf} t, -B_1(t) \sin \omega_{rf} t, B_z \rangle$:

$$\frac{d\vec{M}}{dt} = \gamma((M(t) \times \langle B_1(t) \cos \omega_{rf} t, -B_1(t) \sin \omega_{rf} t, B_z \rangle) \tag{2.26}$$

The effect of applying B_1 at the Larmor frequency is best understood in the rotating frame. Following Chapter 1 of Handbook of MRI Pulse Sequences [42] the time evolution of the magnetization in a rotating frame of frequency of ω:

$$\left(\frac{d\vec{M}}{dt}\right)_{rot} = \gamma \vec{M} \times \left[B_1(t) \left(\hat{x} \cos((\omega_{rf} - \omega)t) - \hat{y} \sin((\omega_{rf} - \omega)t) \right) + \hat{z}(B_0 - \frac{\omega}{\gamma}) \right] \tag{2.27}$$

The square brackets describe the effective magnetic field in the rotating frame. If we consider the frame of precession in the main magnetic field, that is ($\omega = \omega_0 = \gamma B_0$) then the effect of B_0 is completely accounted for by the rotating frame, and only the B_1 component impacts the evolution of the magnetization. The difference between the angular frequency of the reference frame and that of the applied B_1 field determines the rotation of the effective B_1 field in the rotating frame. However if the RF-field is applied on-resonance ($\omega_{rf} = \omega_0$), then the B_1 is static and merely changes amplitude as we change the amplitude of the applied B_1 field. If the amplitude remains constant, B_1, then:

$$\left(\frac{d\vec{M}}{dt}\right)_{rot} = \gamma \vec{M} \times B_1 \hat{x} \tag{2.28}$$

In the rotating frame the magnetization precesses around $\hat{x}$ at a frequency given by γB_1 so to rotate a magnetization from the equilibrium position along $\hat{z}$ into the transverse plane, the constant amplitude RF-field needs to be applied for a quarter period or $\frac{\pi}{2\gamma B_1}$. This is called a 90° pulse.

2.1.4 MRI System

Polarization and manipulation of magnetization is achieved with an MRI system. Its basic components (Figure 2.1) consist of a main magnetic field and associated cooling and driving systems; gradients, gradient amplifiers; RF-coils, including body coil, transmit and receive coils, pre-amplifiers, RF-amplifiers, and cabling; analog to digital converter (ADC); spectrometer that controls the gradients, RF-amplifier, and ADC; and a computer system to re-construct and display the collected images. [43]

The main magnetic field is typically generated by a dense winding of superconducting wires. Often cryogens are necessary to keep the wires in a superconducting state, thus eliminating ohmic heating despite the very high currents needed to generate strong magnetic fields. Persistent superconducting systems are not designed to be turned on and off, and hence require a steady supply of cryogens or very efficient cyrogen capture. Superconducting magnets are typically the most expensive of the available magnet styles, but their benefit is that they are able to generate the highest field strengths and the most homogenous fields.

Other systems use high temperature superconducting windings that do not require cryogens, eliminating the need for quench piping and quench protection systems, but still use pumps and conduction cooling to keep conductors superconductive. The elimination of quenching elements lowers the cost, while the homogeneity can still be well controlled. Yet other systems use permanent magnets rather than current carrying windings. These are typically the least expensive, but give the least flexibility in design, have the highest inhomogeneity, and are very heavy. They also cannot be turned on or off and are typically limited to low-fields because of the limited remnant

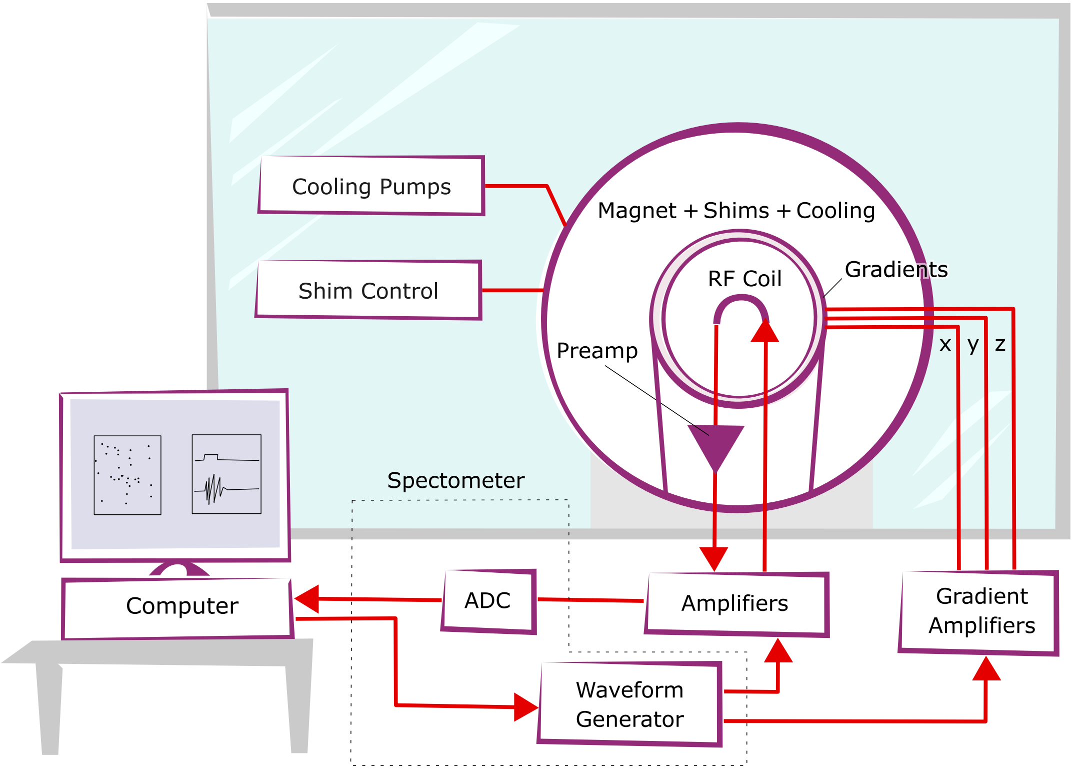

Figure 2.1: A basic diagram of the components of an MRI scanner and how they interconnect to provide controlling signals to the MR system and how signals from the system are relayed to the computer system. Pavel Barta ©. Used with Permission.

magnetization of the materials from which they are assembled.

The main magnet strength, type, and orientation are typically the defining characteristics of an MRI system. A common design is a cylindrical magnet where the superconducting wire is wound along the surface of a cylinder generating a main magnetic field along the inside of the cylinder or bore (Figure 2.2). This design of magnet is used for a broad range of field strengths, from fractions of a tesla up to 10.5 tesla. 1.5 T and 3 T are the most common field strengths in clinical cylindrical systems. Another style of magnet is where two dense windings (“donuts”) are separated by some distance, creating an open gap (Figure 2.3). The two windings are co-axial, and generate a main magnetic field along this common axis. This style of magnet is used in the Viewray system[25]. In the Alberta Linac-MR, two co-axial windings are connected by a iron yoke which shapes the magnetic field[12].

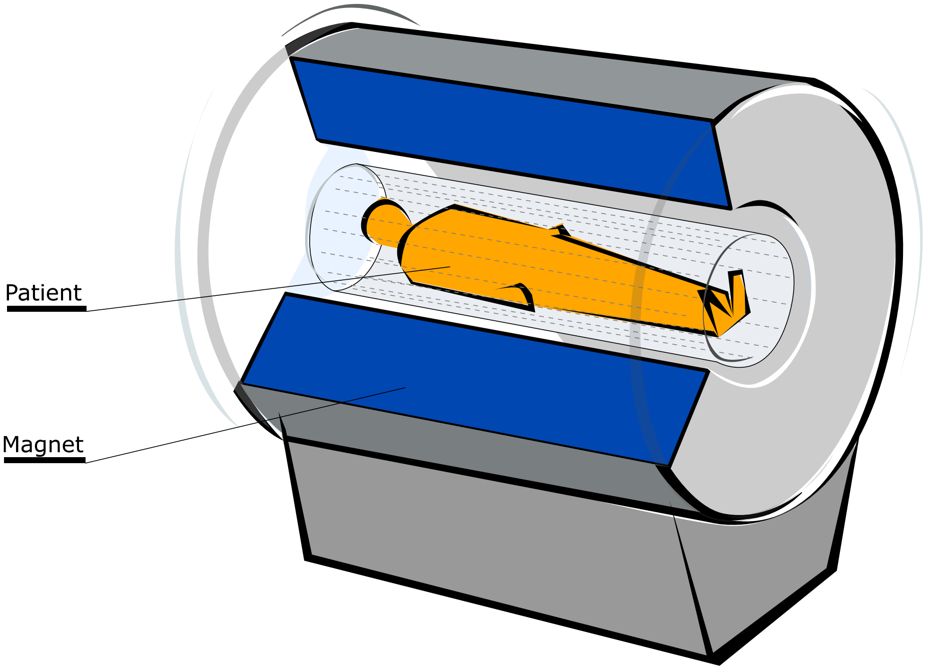

Figure 2.2: A sketch of a superconducting cylindrical magnet with a built in volume transmit coil. The magnet consists of a continuous winding to form a cylindrical bore. The patient is placed in the bore for imaging. Pavel Barta ©. Used with Permission.

Gradients are room-temperature wire windings that generate magnetic fields oriented along the z-axis, that vary linearly in strength from positive to negative across one of the three cardinal axes, x,y, or z. By varying the driving current through the windings, the strength of the linear magnetic field gradient produced can be varied.

The simplest gradient coil design is a pair of loops oriented symmetrically at some +z and -z positions[44]. By driving equal magnitude but opposing currents in each loop, i.e., clockwise in +z, and counter-clockwise in -z, the loop pair generates a magnetic field along the z-axis that points along positive z-axis, diminishes in strength

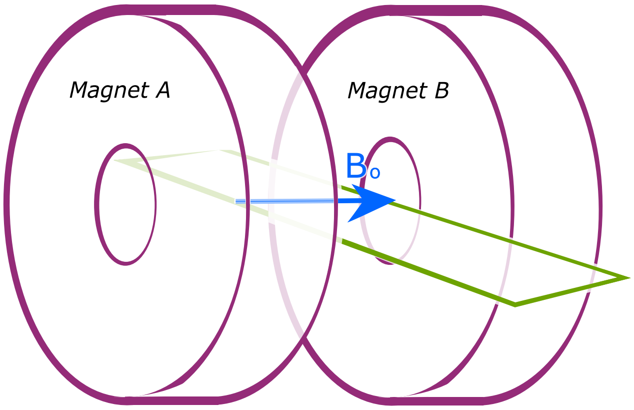

Figure 2.3: A sketch of a double donut magnet formed by two dense windings of conductor that generate a main magnetic field along their common axis. The “bore” is the gap between the two magnets where patients can be positioned. Pavel Barta ©. Used with Permission.

towards the center, reverses directions and increases in strength along negative z-axis towards the bottom loop (Figure 2.4).

Simple designs for gradients along the other axes include a dual pair of saddle coils called Golay coils to generate gradients along x and y (see Figure 2.5). [45]

In modern systems the gradients are typically complex “fingerprint” coils. The desired magnetic field to be produced by the coil windings is first defined and then the inverse Bio-Savart equation is solved to determine the arbitrary current distribution upon a defined surface that would generate that field. Then the arbitrary current distribution is converted to a complex winding pattern that approximates that current distribution. The complex winding patterns follow densely packed curved lines that resemble human fingerprints, hence their name. [46] Modern gradient coils are built on two layers to minimize fields external to the outer layer (i.e., self-shielded). Without shielding, eddy currents in nearby conductors can compromise image quality.

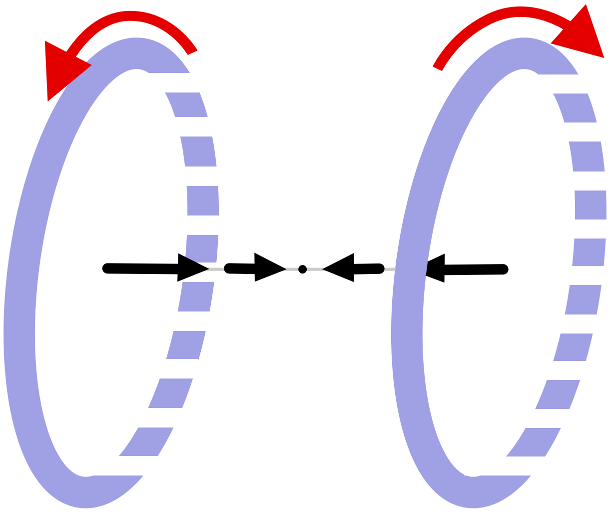

Figure 2.4: A pair of coils with counter rotating currents forming a Maxwell pair. They generate a gradient in the axial magnetic field that has maxima at the coil position and a minimum at a point, equidistant from both coils along their shared axis. Adding a Maxwell pair to a cylindrical MRI system is one way to achieve a z-gradient. Pavel Barta ©. Used with Permission.

In addition to precise and strong gradient fields, gradient systems are expected to ramp the current up and down quickly and precisely. How quickly gradients can be ramped and how precisely sequence defined gradients are played out restricts the complexity of sequences that is possible, and how quickly images can be acquired without artefacts.

In addition to the RF-coils needed to detect the magnetization, the system needs to have a series of RF amplifiers that magnify the millivolt voltages generated in the RF-coil into signals that can be digitized. Amplification is typically at least two stage, with an initial pre-amp located as close to the coil as possible to amplify the signal before travelling down cables that will introduce additional noise. A second stage of amplification occurs before signal processing. An analog-to-digital converter (ADC) digitizes the signal and sends it to the computer system for digital processing. [43]

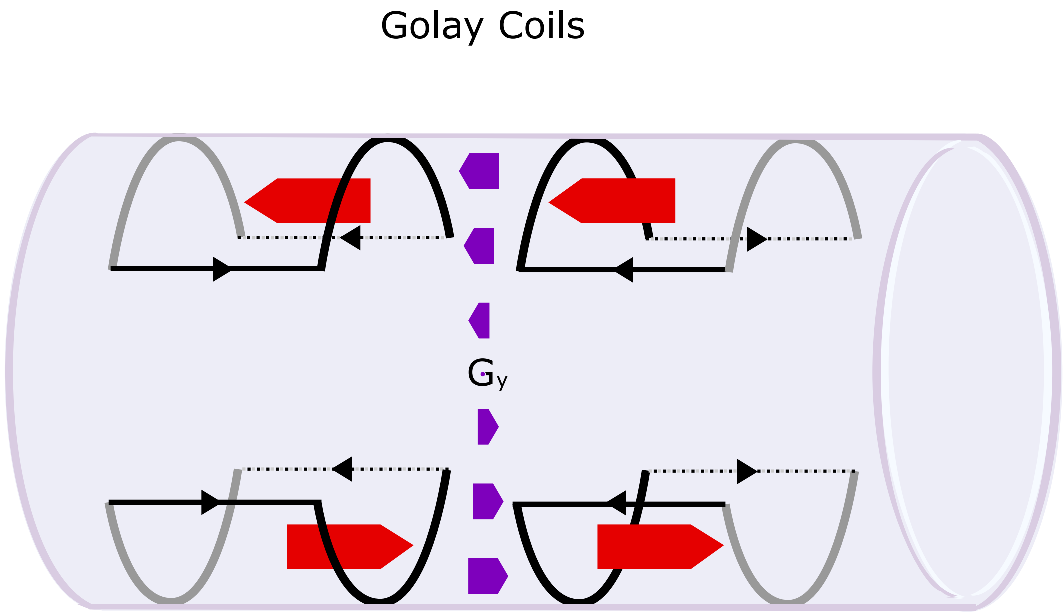

Figure 2.5: A Golay coil consisting of a pair of saddle coils, designed to generate a gradient from top to bottom of the image, labeled the y-gradient. A Golay coil is a coil that can be placed on the surface of a cylinder and will generate a B_z gradient along an axis orthogonal to the axis of the bore. Pavel Barta ©. Used with Permission.

The computer system sends instructions to the spectrometer which converts the sequence timing controls to accurately timed pulses and receives signal from the receive chain. The sequence timing controls are what ensure the gradients and the RF transmit and receive chains operate in a synchronized manner. This synchronization allows the spectrometer to manipulate the magnetization and receive the signal correctly so it can be reconstructed into a faithful image.

2.1.5 RF-Coils

The RF-coils play two key roles in imaging, as the end point of the transmit (Tx) chain, which generates the RF pulses that excite and manipulate the magnetization, and as the starting point of the receive (Rx) pathway that detects the signal generated by precession of magnetization[40, 43]. All RF-coils consist in the most basic sense of a conductive loop (or multiple loops) typically made of copper due to its ready availability and high conductivity. Alternative conductors include silver, aluminum, graphene, and other conductive materials. The loop of conductor acts like an inductor. The loop is typically tuned to a narrow band resonance at the Larmor frequency using one or more capacitors. A matching network consisting of capacitors, inductors, and other electronic components, connects the loop to the receive or transmit chain. The network matches the impedence of the coil to that of the coaxial cable which is used to interconnect the different elements of the analog portions of the RF system.

The transmit pathway begins with a signal generated by the spectrometer that is converted to analog by a digital to analog converter (DAC)[43]. This signal is modulated with the Larmor frequency and amplified through high-power RF-amplifiers. The amplified current flows through transmit RF-coils that generate the B_1 field described earlier. Only the component of the B_1 field that rotates with the precession drives the excitation. Any B_1 field (linear or quadrature) can be decomposed into a component rotating with ($B_1{}^{+}$) and a component rotating against the precession ($B_1{}^{-}$).

$$\begin{aligned} B_1^+ &= \frac{B_{1x} + jB_{1y}}{2} \\ B_1^- &= \frac{B_{1x}^* + jB_{1y}^*}{2} \end{aligned} \tag{2.29}$$

where the B_{1x} and B_{1y} are the complex magnetic fields along the x and y axis in the laboratory frame and * denotes the complex conjugate[41]. The transmit properties of RF-coils depend on the B_1^+. By applying reciprocity, because the direction of propagation reverses in reception, the detection properties of receive coils actually depend on B_1^- (note that in reception that field is not actually being produced)[47].

Transmit coils need to generate a homogeneous field to ensure uniform excitation across the subject or sample. They also must be able to handle a large voltage and current. Power transfer between the cabling and the coil must be very efficient at the Larmor frequency so the least amount of power is wasted in driving the Tx-coils.

This transmit efficiency is typically described by the ratio of field to driving power.

$$\Psi = \frac{B_1^+}{\sqrt{P}} \tag{2.30}$$

Tx-coils are typically volume coils. These are homogeneous coils that can be used for Tx, Rx or both, are rigid, and are sometimes built into the bore of the MRI system.

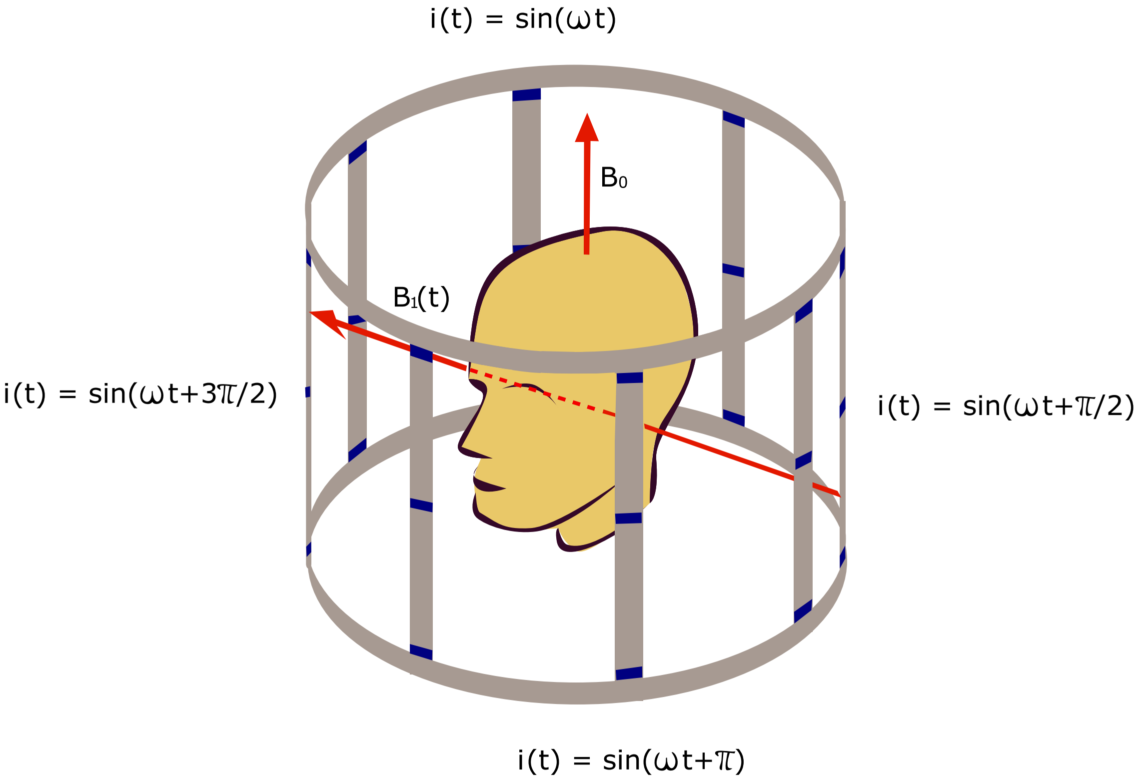

Figure 2.6: A birdcage coil surrounding a human head, the current in the coil at some time, t, is shown in four representative rungs of the birdcage. The current in each rung is phase shifted relative to the others, such that there is a total 2π phase shift around the circumference. The RF-field generated by the birdcage is perpendicular to the birdcage rotational symmetry axis. As the current in the rungs changes the RF-field generated will rotate at the frequency of the current oscillations in the rungs. Pavel Barta ©. Used with Permission.

A birdcage coil (Figure 2.6) consists of two end rings connected by a number of evenly spaced legs. It is intended to be used with the end rings co-axial with the main magnetic field, which is along the bore in cylindrical systems. The birdcage is designed to be driven in quadrature and generate a circularly polarized field in the transverse plane.

The birdcage is ideal for the cylindrical magnet since its own cylindrical shape fits inside the main magnetic field and gradient windings, co-axial with each, and generates a rotating B_1 field perpendicular to the main magnetic field[40].

Quadrature coils like the birdcage require driving at two points with 90° out of phase signal. This is achieved with a quadrature coupler which splits the driving analog signal into two equal signals and sends one along a slightly longer path to delay it by 90°. If a quadrature coil is used to receive signal, the process can be reversed to recombine the 90° out of phase signals into a single signal[40].

Despite the additional complexity of quadrature coils they have a power efficiency advantage over linear coils, which generate a non-rotating, but alternating B_1 field along only one axis orthogonal to the main magnetic field. Consider a field ${B_1}^+ = B_{1x}$ generated with a linear coil using some power P, the linear efficiency is then just given by Equation (2.30)

If the same power, P, is applied to each port of a quadrature coil 90° out of phase (total power 2P), then $B_{1x} = jB_{1y}$. Hence the field generated by the quadrature coil is $2{B_1}^+$. This means the efficiency of the quadrature coil is given by:

$$\Psi_Q = \frac{2{B_1}^+}{\sqrt{2P}} = \sqrt{2}\Psi \tag{2.31}$$

Linear coils are also commonly used in MRI, especially in reception. A simple design is a loop coil which generates a B_1 field is generated along the loops central axis. This kind of linear coil however is primarily only used for reception due to the high inhomogeneity which is unacceptable in excitation.

A solenoid coil combines multiple turns to increase sensitivity and homogeneity generating a field along its central axis. This design does not work in a cylindrical MRI scanner, but could be used other systems where the main magnetic field is not along the patient axis[40].

Another common linear coil is a Helmholtz pair. Two equal sized circular loops are positioned one radius apart[40]. The Helmholtz coil generates a field within 10% of maximum B_1 over a central area with a radius 50% of the Helmholtz radius[48]. A Helmholtz-like arrangement of two coils with a widened gap results in poorer homogeneity at the center, though the variation from the center to the coil planes can actually improve. In practice for RF-coils a homogeneity of about 10% can be called homogeneous. The requirements on the B_1 field are a lot less strict than on the B_0 field[40].

Receiving signal can be done with a coil that is used to transmit. In this case this coil is known as a Tx/Rx coil, while if a separate coil is used to detect signal, then it is a Rx-only coil. If a Tx/Rx coil is used, the system needs a transmit/receive switch. A transmit/receive switch ensures the driving signal flows into the coil, but that the receive line is protected from reflections or direct flow from the transmit chain. It also ensures that when the coil is receiving all of the received signal that goes down the receive chain path isn't lost to the transmit chain, and noise from the Tx chain doesn't get added to the signal. On Rx-only coils, the receive chain also needs to be protected from the excitation generated by the Tx coil, and the coil needs to not get excited, as this could alter the excitation B_1 experienced by the sample. This is achieved through the use of detuning traps that shift the operating frequency of the Rx-coil during excitation, either actively or passively through crossed-diode detuning[43].

2.1.6 Spatial Encoding and Imaging

The previous sections introduced the basics of MR signal generation and the components necessary for imaging. Before diving into the practical construction of RF-coils it is important to briefly look at a few pulse sequences and understand how spatially-encoded MR images are possible.

Consider the signal detected by an RF-coil, based on Equation (2.22). It can be described in terms of magnitude and phase[49].

$$\begin{aligned} s_{rf}(t) = -\epsilon_{loop} &= \int d^3\vec{r}\frac{d\vec{M}}{dt} \cdot \vec{S}_p(\vec{r}) \\ s_{rf}(t) &= \int d^3\vec{r}\omega_0\vec{S}_p(\vec{r}) \cdot \vec{M}_0(\vec{r})e^{j(\omega_0 t - \phi(\vec{r},t))} \\ s_{rf}(t) &= \int d^3\vec{r}\rho_{eff}(\vec{r})e^{j(\omega_0 t - \phi(\vec{r},t))}df \end{aligned} \tag{2.32}$$

The ρ_{eff} is defined as the effective spin density, grouping together the spatial distributions of the temporally stable elements of the detection coil and the magnetization. ρ_{eff} includes the spatial distribution of the receive coil (Equation (2.24)), the spatial sensitivity of the excitation pattern of the transmit coil, and the spatial distribution of the actual spins themselves. The first exponential term describes the time evolution of the magnetization as it undergoes precession as described in Equation (2.11). The second exponential describes the spatial and time dependent accumulation of phase that occurs when regions of the sample experience different effective local B_z that cause spins to gain or lose phase relative to ω_0. Equation (2.32) formulation ignores relaxation and protons with slightly different Larmor frequencies for simplicity and clarity[49]. Consider now the application of a gradient magnetic field along the z-axis that varies with the position along the x-axis[49].

$$B_z(t) = B_0 + \vec{G}(\vec{r},t) \cdot \vec{r} = B_0 + xG_x(t) \tag{2.33}$$

In terms of frequency, the precession of spins is spatially dependent:

$$\omega(x,t) = \omega_0 + \gamma x G_x(t) \tag{2.34}$$

This use of the gradient to link spatial position to frequency is called frequency encoding. The change in phase relative to ω_0 is spatially dependent and given by:

$$\phi(x,t) = \int_0^t \gamma x G_x(t')dt' \tag{2.35}$$

The gradient term can be described as a spatial frequency k_x:

$$k_x(t) = \int_0^t \frac{\gamma}{2\pi} G_x(t')dt' \tag{2.36}$$

The signal as a function of time then can be written as

$$s_{rf}(t) = \int d^3\vec{r}\rho_{eff}(\vec{r})e^{j(\omega_0 t - 2\pi k_x(t)x)} \tag{2.37}$$

Ignoring the ω_0 dependence (i.e., demodulating) and laying out the acquired signal according to the spatial frequency $k_x(t)$ the signal becomes explicitly the Fourier transform of the effective spin density.

$$\begin{aligned}
s_{rf}(t) =& \int d^3\vec{r}\rho_{eff}(\vec{r})e^{-j2\pi k_x(t)x} \\
s_{rf}(k_x) =& \int dx\rho_{eff,x}(x)e^{-j2\pi k_x x} \\
s_{rf}(k_x) =& FT(\rho_{eff,x}(x)) \\
& \text{hence:} \\
\rho_{eff,x}(x) =& FT^{-1}(s(k_x)) \\
& \text{or generally:} \\
\rho_{eff}(\vec{r}) =& FT^{-1}(s(\vec{k}))
\end{aligned} \tag{2.38}$$

Frequency encoding in imaging is achieved by applying a “read” gradient (i.e., G_x) while signal is being received. In this case, linearly separated, subsequently acquired time points will be linearly spaced measurements of the signal in k-space (the space defined by $s(k)$). Frequency encoding occurs along the direction that the gradient varies, for example the x-axis as described above. A Fourier transform of this data gives a one dimensional image of ρ_{eff}, i.e., a projection along the gradient. It is possible to build up a 2D k-space matrix by applying a perpendicular “phase-encode” gradient (i.e., G_y) before each frequency encoding gradient. In this case the points acquired during reception will be spaced linearly along the read gradient axis but offset along the phase-encode gradient direction to k_y based on the amplitude

$(G_y(t'))$ and amount of time (t_{pe}) the phase-encode gradient was applied for:

$$k_y = \int_0^{t_{pe}} \frac{\gamma}{2\pi} G_y(t)dt \tag{2.39}$$

By repeating the data acquisition and varying the phase-encode gradient, a two dimensional k-space set of data can be collected and 2D Fourier transformed to give a two-dimensional MRI image. This process of repeating acquisition can be again repeated once for each line of the third dimension (i.e., k_z) to build a three dimensional image.

More common is the use of a slice select gradient during excitation so that the signal received is only coming from a particular slab of the sample or subject. The resulting two dimensional MRI image (p(x,y)) is then a cross-sectional slice image of the sample. Slice selection is based on applying a gradient along an axis (i.e., z-axis) and applying a frequency selective excitation pulse. The goal of the slice selective pulse thus is to excite a rectangular function of spatial frequencies that match the slab of interest $(rect_{\Delta z}(z))$. In the time domain (i.e., the pulse shape), the Fourier transform of the rectangular function is a *sinc* function $(B_1(t) \propto \sin(\pi k_z \Delta z)/(\pi k_z))$[49].

In general through the combination of gradient fields along x, y, and z-axis, gradients along any axis through the sample can be generated. Gradients applied during excitation select a slab or slice. Gradients applied after excitation, before, and during reception allow movement through k-space. The signal received at a specific time after excitation is the signal for the position in two-dimensional k-space given by:

$$< k_x, k_y >= \left\langle \int_0^{t_{pe}} \frac{\gamma}{2\pi} G_x(t)dt, \int_0^{t_{pe}} \frac{\gamma}{2\pi} G_y(t)dt \right\rangle \tag{2.40}$$

A gradient(s) applied during reception results in data being collected for a line through k-space along a path governed by the gradient(s) applied. A Fourier transform of the k-space data gives an MRI image. The intensity of acquired signal depends on the underlying effective spin density (p, see Equation (2.32)) and whether the spatially distributed spins are in phase. Typically the signal maximum occurs at the center of k-space where phase accumulation relative to ω_0 is zero for all spins. This all assumes there is no relaxation during the reception time and the same amount of relaxation occurs prior to reception for each phase encode. In general, the trajectory through k-space and the rate of relaxation will affect which spatial frequencies have the largest amplitudes (i.e., k-space filtering)[50].

A feature of k-space data is that the signal's energy is located mostly at the center of k-space. An example of how omitting certain portions of a k-space will impact the resulting image is shown in Figure 2.7. Thus imaging sequences are typically designed to measure the center of k-space when the signal is at a maximum thanks to an echo (see Imaging Sequences in 2.1.4). The edges of k-space are where information about details and edges of the image are found. The further out in k-space that data is collected, the more detailed the image. Not collecting data towards the edges leads to a more blurred image that has the same broad structures, with worse boundary definitions.

2.1.6.1 Imaging Sequences

Over the years, many possible pulse sequences have been developed to generate various kinds of images and exploit various kinds of contrast. Two common categories have emerged and are worth discussing specifically. The first has no rephasing RF pulse during the echo time: these are gradient-echo sequences. The second does have a rephasing RF pulse during the echo time: these are spin-echo sequences[49].

A basic gradient echo sequence (Figure 2.8) consists of a slice-selective pulse and a corresponding slice select gradient to excite a slab of the sample. Along an orthogonal axis a phase encode gradient is applied to shift to a specific line in k-space. After excitation, a brief negative gradient along the third and final orthogonal axis is applied dephasing the transverse magnetization so that acquisition can begin at the edge of k-space rather than from a central axes. Then the gradient along this third axis (called the "readout" direction) is reversed while receiving the signal with an RF-

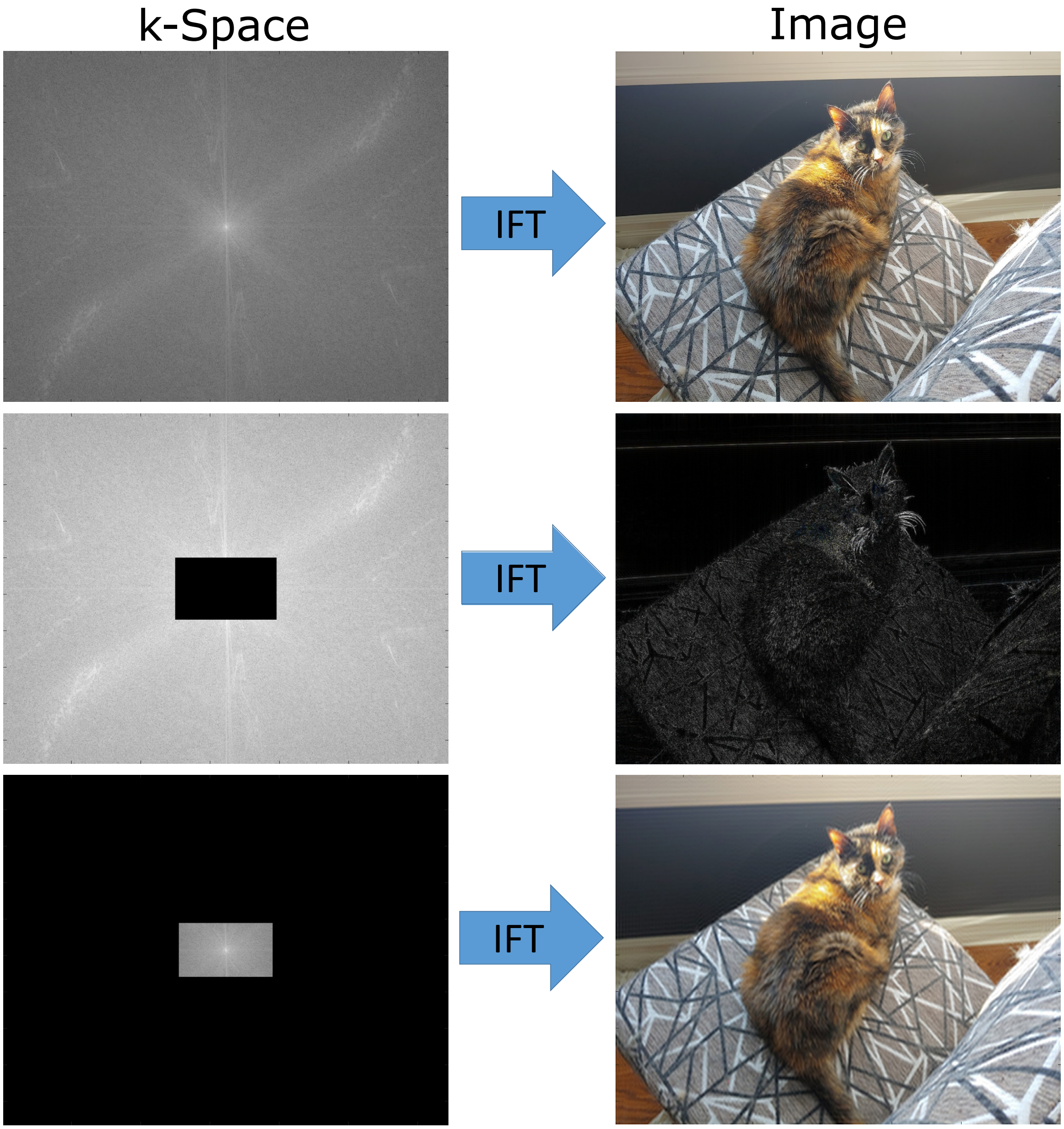

Figure 2.7: An example of images of my cat, Cassandra, generated from a fully sampled k-space (top, only red channel shown for each k-space), a k-space missing the center region (middle), or a k-space only centrally sampled (bottom). The best image of Cassandra is seen when all of the k-space is acquired. If we, however, sample only the edge of k-space, only missing a small portion of the center, the image becomes much darker (displayed image magnitude was doubled) as most of the energy is located at the center in the lower spatial frequencies. The edges of k-space lead to an image that retains only edges of objects in the image, like whiskers and outlines. By focusing on acquiring the center of k-space if we cannot get all of it, then we can ensure that, while blurring and distinct line artifacts are present in the image, Cassandra is easily identifiable.

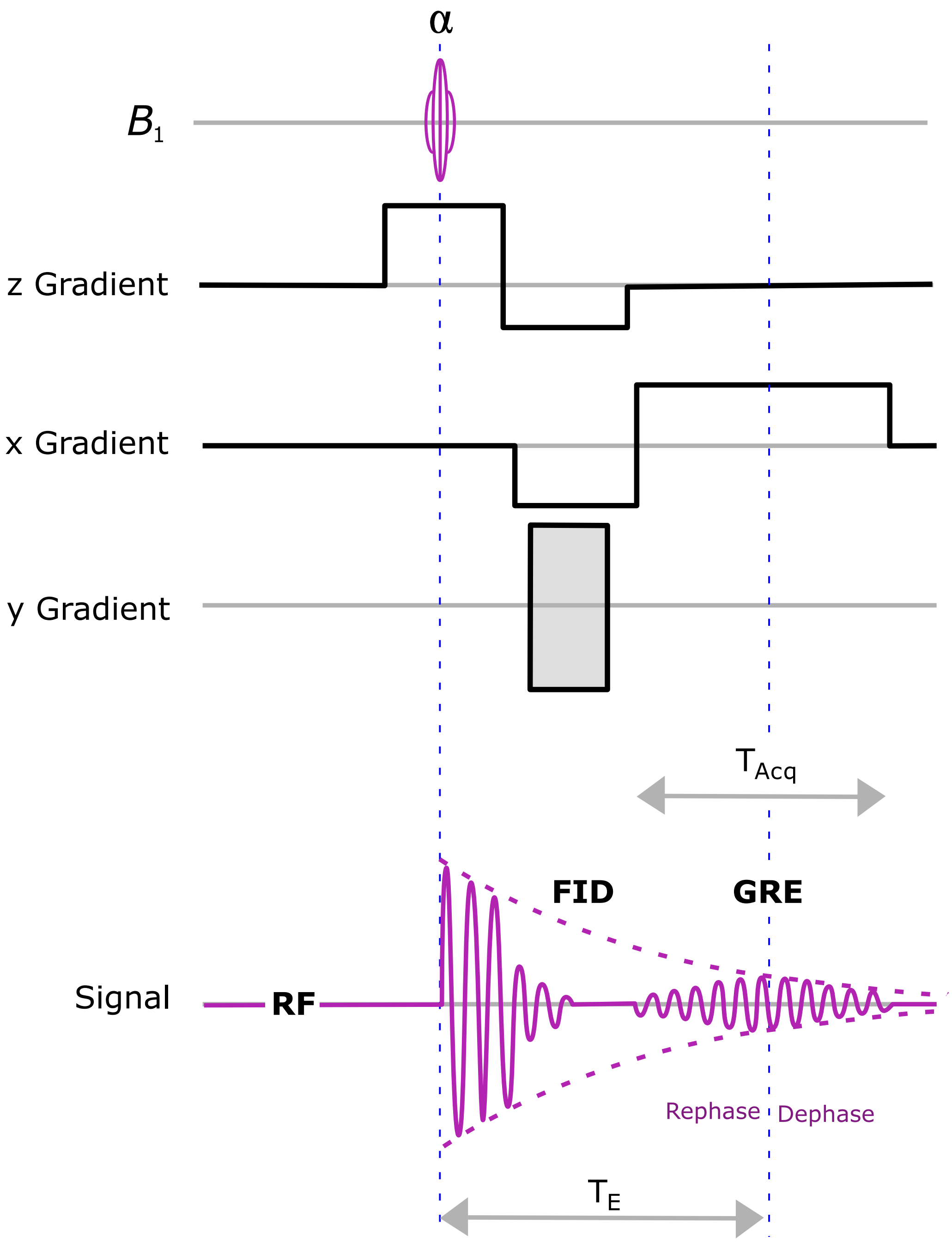

Figure 2.8: An example gradient echo sequence consisting of an excitation pulse (flip angle α) with a slice select gradient, an encoding gradient, and a dephasing and then rephasing read gradient. The amplitude of the echo is determined by T_2^*. Note that the signal shown is a representation of the available signal, but the readout signal only occurs when the x gradient is active. Pavel Barta ©. Used with Permission.

coil, this positive gradient will rephase the magnetization and then dephase it the same amount. This acquires data along a line in k-space at the position set by the phase encode gradient. A line is collected because signal is received for all phase variations as the read gradient varies the phase accumulation along the third axis from the negative phase accumulated before receiving all the way to the same magnitude of phase accumulation, but positive. The time at which the phase accumulation is 0, is termed the echo time (TE). Since static B_0 inhomogeneity contributes to the dephasing in a gradient echo, the magnitude of the echo depends on T_2^*[49].

A basic spin echo sequence (Figure 2.9) is where at TE/2 after excitation, an 180° rephasing pulse is applied to the magnetization. At TE after excitation, all dephasing due to static B_0 inhomogeneity is eliminated, creating a spin echo. Consider a magnetic moment that experiences a local B_0 field of $B_z + \delta$. For the first TE/2 this magnetic moment will accumulate $\gamma\delta\frac{TE}{2}$ radians of phase compared to an on-resonance moment. A 180° refocusing pulse inverts the phase accumulated of all the magnetic moments. The magnetic moment in $B_z+\delta$, now has accumulated effectively $-\gamma\delta\frac{TE}{2}$ radians compared to an on resonance moment. After a further TE/2 then the moment will accumulate an additional $\gamma\delta\frac{TE}{2}$ as compared to an on-resonance moment. The sum of the inverted initial phase accumulated and the phase accumulated in the subsequent TE/2, is zero compared to the on resonance moment. At TE for a spin-echo sequence there is an echo where all magnetization has re-phased thanks to the refocusing. For imaging, the excitation, phase, and read gradients are applied as for the gradient echo sequence. It is desirable that the read gradient is applied such that when the read gradient has rephased the magnetization, during reception, this occurs at TE so that all of the magnetization is refocused, not only due to the gradients, but also due to the static B_0 inhomogeneity. This avoids phase shifts in the k-space data. Due to the refocusing of static B_0 inhomogeneity the echo magnitude will depend on T_2 rather than T_2^*[49].

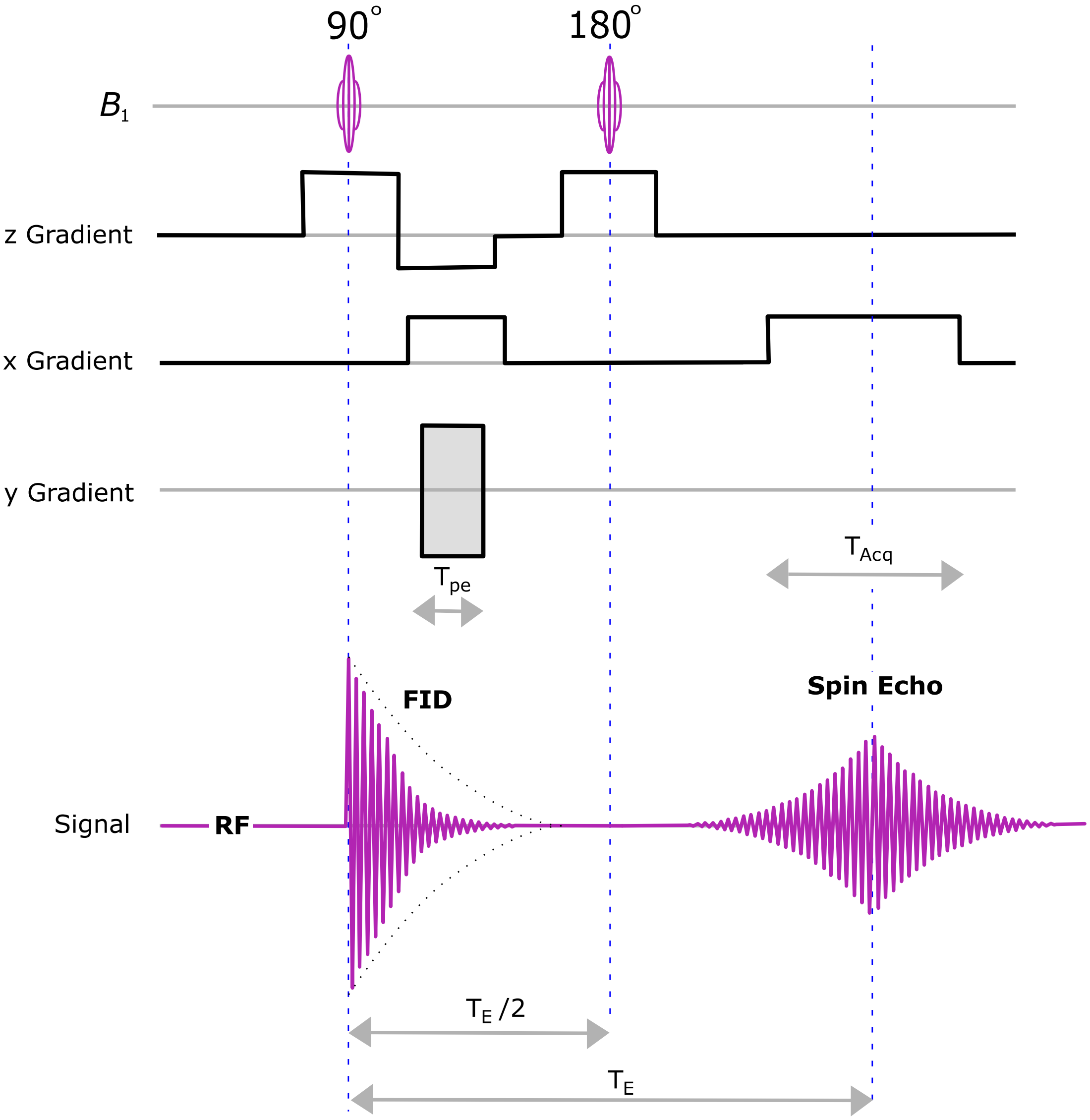

Figure 2.9: An example spin echo sequence consisting of a 90° excitation pulse with a slice select gradient, an encoding gradient, a 180° re-focusing pulse, and dephasing and rephasing read gradients. The amplitude of the echo is determined by T_2. Pavel Barta ©. Used with Permission.

2.1.6.2 Image Contrast

The contrast in an MRI image is dominated by differences in relaxation times between different tissues. Contrast due to differences in material properties (T_1, T_2, magnetization density) can be manipulated by adjusting the imaging parameters of repetition time (TR) and echo time (TE)[51].

Repetition time (TR) is the total time between subsequent excitations such as the time between excitations with two different phase gradients or phase encodes. The amount of magnetization available to excite may be less than the total magnetization depending on the flip angle, which determines how much of the available magnetization is rotated into the transverse plane, and the TR, which determines how much time the longitudinal magnetization has to recover. The recovery is governed by the T_1 of the material. For large flip angles, TR must be much longer than the T_1 for the magnetization to fully recover, while if a small flip angle is used, the magnetization is only recovering a small amount and imaging can be done much more quickly. If two materials in the body have different T_1 parameters, we can choose a flip angle and TR such that the longer T_1 material doesn't fully recover, in the same time the shorter T_1 material will recover more or even perhaps completely (see Equation (2.9). This will result in the material with the shorter T_1 having more magnetization to excite after each TR and hence will appear brighter in the image. This is known as T_1-weighted imaging[51].

Echo time (TE) is the time between excitation and the measurement of the signal. The longer the echo time the more time there is for the transverse magnetization to decay at a rate given by the material T_2^* (or T_2 for spin echo sequences), reducing the overall signal in the image. This can also be exploited for contrast. If two materials have different T_2^*'s an intermediate TE will led to the shorter T_2^* material decaying more and appearing darker in the image. This is known as T_2^*-weighted imaging. In the case of spin echo sequences, magnetization is refocused to eliminate the effect of B_0 inhomogeneity, thus the image is T_2 weighted[51].

If TR is very long and TE is very short, such that all the magnetization recovers before each subsequent excitation and there is little magnetization decay before acquisition, then the image contrast is dependent on the density of protons, resulting in a proton-density image. In most situations proton density weighting gives poorer contrast than weighting that includes the effects of relaxation. Across various soft tissues the proton density doesn't vary significantly, but the local environment that influences relaxation can vary significantly due to tissue structure, including chemical composition (impacts spin-lattice interactions) and how it limits the movement of water (impacts spin-lattice and spin-spin interactions)[51].

2.1.6.3 Role of Noise in Image Quality

The signal in MRI is voltage in an RF-coil and hence acquisition of this signal suffers from inevitable noise and interference added by conductors and electronic devices. The primary source of noise in electronics is thermal fluctuation of the charge carriers in the conductor; this noise is called Johnson noise[52]. The noise power (V^2) is proportional to the effective resistance (or loss) in the circuit formed by the RF-coil, the body and the environment. Hence the noise voltage, V_N, in MRI signal is given by:[52]

$$V_N = \sqrt{4k_B T r} \tag{2.41}$$

where k_B is the Boltzmann constant. T is the temperature of the system, and r is the effective resistance.

Sources of loss in MRI include the sample (magnetic and electrical losses) and the RF-coil (conductive and radiative losses) [40]. Other elements of the receive chain such as cabling and amplifiers can contribute to losses, but typically the RF-coil and sample dominate if pre-amplifiers are placed close to the RF-coil. By amplifying near the coil, any further thermal noise sources can be made negligible. Sample magnetic losses (r_M) depend on a coil geometry dependent term (R_M), the sample electrical conductivity (σ_{con}), number of turns (N), and size (d), and, critically, the frequency (ω). Magnetic losses in the sample are typically the largest contributor in most MRI imaging scenarios. [40]

$$r_M = R_M \sigma_{con} N^2 \omega^2 \frac{d^5}{2} \tag{2.42}$$

The second most dominant are the conductive losses in the RF-coil and receive chain before the initial amplification. These losses depend on the resistivity of the wires used and the quality of the lumped components. These losses are frequency dependent due to the skin effect in conductors[40].

$$r_\Omega = R_\Omega \omega^{\frac{1}{2}} \tag{2.43}$$

Where R_Ω depends on coil geometry and material.

The electrical losses are due to stray electric fields from the RF-coil inducing currents in the lossy dielectric of the sample. The fringe electric fields are caused by charges and depend on the coil's geometry, self inductance (L), and capacitance (C). These should be minimized in the RF-coil design to minimize this noise source. [40]

$$r_E = R_E \omega^3 L^2 C \tag{2.44}$$

Where R_E is a coil geometry dependent term.

Finally there are also radiative losses due to the RF-coil acting as an antenna and potentially radiating energy into free space where it isn't coupling to the sample and contributing useful signal (while receiving noise from the surroundings). This depends primarily on the size of the coil and goes as ω^4. With good RF-coil design radiative losses are not significant next to r_M and r_Ω. For example, for a 60 mm diameter loop coil that is tuned to 200 MHz, the radiative losses are estimated at 0.05 Ω, while the resistance of the conductor is about 0.4 Ω[40].

Based on the assumption of good coil design where r_M and r_Ω dominate, the noise in MRI depends on frequency according to

$$V_n = \sqrt{4k_BT\left(a\omega^{\frac{1}{2}} + b\omega^2\right)} \tag{2.45}$$

where a and b are the collected terms (not including frequency) of magnetic and conductive losses respectively.

2.1.6.4 Image Quality: SNR

The total signal available depends on the total magnetization (type of nuclei and B_0) and relaxation (T_1 and T_2). One aspect of image quality is the ratio of signal received compared to the noise in the received signal, i.e., the signal-to-noise ratio (SNR). The signal is proportional to ω times the magnetization, hence signal is proportional to γ^3 and B^2 (Equation (2.2)). Considering only protons, the signal is proportional to ω^2 [53]. Hence by combining Equation (2.23) and Equation (2.45) we obtain the expression given by Edelstein for SNR's proportionality to frequency in MRI:[53]

$$SNR \propto \frac{\omega^2}{\sqrt{a\omega^{\frac{1}{2}} + b\omega^2}} \tag{2.46}$$

The relationship between SNR and ω is such that SNR is roughly proportional to B_0. This is one motivation for using stronger magnetic fields.

The other important consideration for image quality in MRI is scan time. While for a given B_0 the maximum available magnetization, M_0 is fixed, it is common to improve SNR through signal averaging, reducing noise by ${N_{rep}}^{-\frac{1}{2}}$ where N_{rep} is the number of sequence repetitions. Each repetition, however, requires the same amount of time as the first, meaning that image quality and imaging speed compete.

$$SNR \propto \sqrt{T} \propto \sqrt{N_{rep}} \tag{2.47}$$

2.1.6.5 Image Quality: CNR

A defining purpose of imaging is to distinguish different tissues and materials in the body. This is quantified by the contrast to noise ratio (CNR). There are several available contrast mechanisms including the variation of proton density, T_1, and T_2 between different tissues.

Proton density can be useful for distinguishing between low water content structures like cartilage and soft tissues like fat and muscle. The density of protons does not change with field strength. Proton density weighted image contrast depends on the SNR and hence B_0.

Relaxation offers several methods for contrast. Pulse sequences exploit differences in relaxation properties to generate different kinds of contrast, with achievable CNR dictated by the differences in T_1 and T_2 (both of which change with field strength). A study investigating CNR in real-time imaging applications across a range of field strengths showed CNR differences between 0.5T and 1.5T were significantly smaller than SNR differences, and for certain tissues 0.5T is predicted to have higher CNR[54].

The importance of different image quality metrics depends on the application. Images may be interpreted by radiologists who rely on good image SNR and CNR to identify and interpret features or images may be used for tracking structures where structures simply need to be distinct enough[55]. Studies have shown that while higher field strengths lead to improved image quality, the extent of the improvement is lower than that predicted by naive linear models and in many cases leads to no diagnostic advantage[56, 57]. When considering new applications, like Linac-MR, where strong B_0 fields can lead to undesired effects such as deflection of electrons (see Section 2.2.2.2), the optimal field strength may not be the strongest field achievable[54].

2.1.6.6 Image SNR

The amplified analog voltage signal from RF-coils is sampled, and used to populate a k-space data matrix based on the trajectory defined by the imaging sequence. The k-space matrix is the spatial frequency information of the sample or patient being imaged (Figure 2.10, left).

K-space data is complex because the coil signal is demodulated using phase-sensitive quadrature detection resulting in real and imaginary components. A two or three dimensional Fourier transform of the k-space matrix generates the corresponding complex MRI image (Figure 2.10, right), of which the magnitude is typically considered the MRI image of the sample or subject. Thermal noise in MRI images can be considered additive white Gaussian noise and will be uniformly distributed throughout both the image and k-space[58].

SNR in MRI images can be measured in a few different ways, based on how much

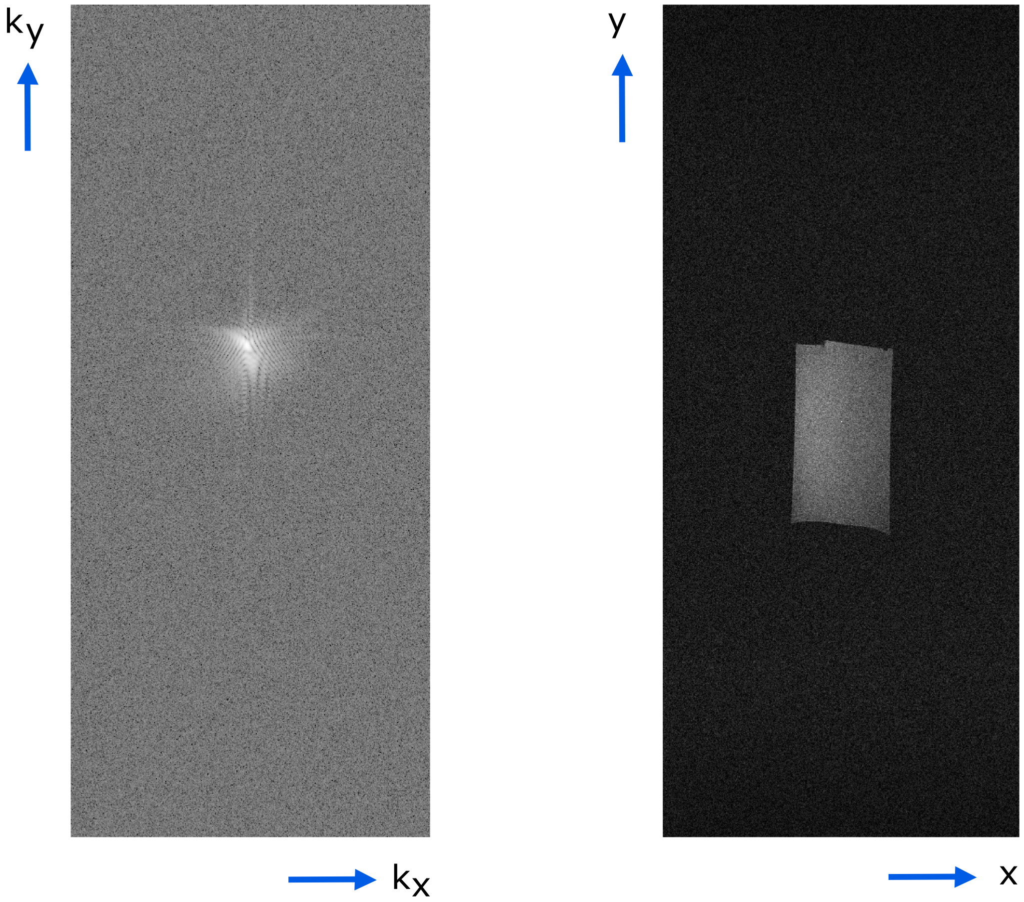

Figure 2.10: Left: A visualization of k-space data (log of the magnitude). Right: The corresponding magnitude image generated by 2D Fourier transform of the k-space data shown on the left.

time and imaging sequence flexibility is available. Three methods are single-image region of interest (ROI) SNR, difference image SNR, and separate signal and noise image SNR. Consider an image with N voxels. Let s_k be the matrix value of voxel $k \in I = [1, N]$.

1. The first method (Figure 2.11) is the least expensive in terms of time on the scanner, and easiest to implement as it can be done on any reconstructed MRI image. The signal (s_{avg}) is evaluated as the average voxel value in the magnitude image (I) over some chosen ROI containing voxels, $Y \subset I$.

$$s_{avg} = \frac{\sum_{k \in Y} |s_k|}{\sum_{k \in Y} 1} \tag{2.48}$$

The noise (n) is evaluated as the standard deviation of voxel values over an ROI that is known to contain only air, typically a region exterior to the sample or subject being imaged[59]. Let all the voxels in this ROI be $Y_N \subset I$.

$$\begin{aligned} n &= \sqrt{\frac{\sum_{k \in Y_N} (|s_k| - s_{N,avg})^2}{\sum_{k \in Y_N} 1}} \\ s_{N,avg} &= \frac{\sum_{k \in Y_N} |s_k|}{\sum_{k \in Y_N} 1} \end{aligned} \tag{2.49}$$

The SNR then is:

$$SNR = 0.65 \frac{s_{avg}}{n} \tag{2.50}$$

The factor of 0.65 approximately corrects for the fact that because the noise variance is being calculated from a magnitude image, the original Gaussian distributed noise is now Rayleigh distributed. If instead complex image data is used then:

$$\begin{aligned} n &= \sqrt{\frac{\sum_{k \in Y_N} (s_k - s_{N,avg})(s_k - s_{N,avg})*}{\sum_{k \in Y_N} 1}} \\ s_{N,avg} &= \frac{\sum_{k \in Y_N} s_k}{\sum_{k \in Y_N} 1} \end{aligned} \tag{2.51}$$

and SNR is simply:

$$SNR = \frac{s_{avg}}{n} \tag{2.52}$$

2. As above, the second method also requires no modifications to the imaging sequence, but allows a better estimation of the noise. By repeating the same acquisition twice, a difference image (I_d) can be generated by subtracting the second magnitude image from the first ($I_d = |I_1| - |I_2|$) in a voxel by voxel manner. In this case the signal to noise is calculated by once again selecting

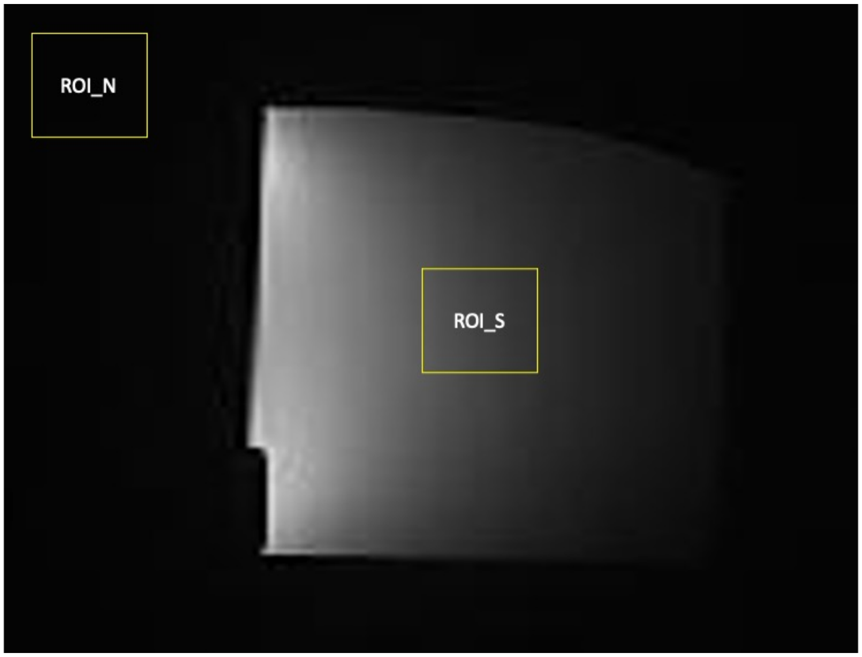

Figure 2.11: Examples of signal ($\mathrm{ROI_S}$) and noise ($\mathrm{ROI_N}$) regions in a single magnitude image. The same corresponding regions can be used for a complex image, but the complex values rather than the displayed magnitude values would be used in the calculation.

a signal ROI, Y and calculating an average voxel value for either of the two magnitude images ($Y \subset I_1$ or $Y \subset I_2$). The noise is calculated as the standard deviation of the voxel values in the same ROI, but in the difference image ($Y_N \subset I_d$)[59]. Hence

$$s_{avg} = \frac{\sum_{k\in Y} |s_k|}{\sum_{k\in Y} 1} \tag{2.53}$$

$$\begin{aligned} n &= \sqrt{\frac{\sum_{k\in Y_N}(s_k - s_{n,avg})^2}{\sum_{k\in Y_N} 1}} \\ s_{n,avg} &= \frac{\sum_{k\in Y_N} s_k}{\sum_{k\in Y} 1} \end{aligned} \tag{2.54}$$

SNR then is given by: and SNR is:

$$SNR = \frac{1}{\sqrt{2}} \frac{s_{avg}}{n} \tag{2.55}$$

The $\sqrt{2}$ factor accounts for the fact that the noise is evaluated from the difference of two images, hence it is underestimated.

3. The third method gives the purest noise measurement, but it requires an extra image to be acquired and a modification of the pulse sequence. An image with signal (I_S) is acquired as before, and a second noise image (I_N) is acquired by repeating the same sequence again, but without any transmit RF-pulses during the entire acquisition. This means the sample is not excited, and the only signal picked up is thermal noise. The signal then is the average voxel value of some ROI in the signal image ($Y \subset I_S$). The noise is the standard deviation of all the voxel values in the noise image ($N = I_N$). Image signal and noise are the same as those given in Equation (2.48), Equation (2.51), and Equation (2.52).

2.1.7 Radiation Induced Current

There is an important component of image quality for linac-MR systems that is not found in MRI-only systems. When high energy photons strike the conductor of an RF-coil, electrons can be ejected. If there is no equivalent influx of electrons, this leads to a region of positive charge in the RF-coil conductor. Since an RF-coil is a grounded electric circuit, current will flow to restore neutrality, thus radiation induces a current. The higher the dose rate, hence rate at which electrons are ejected, the higher the current. The amplitude of the induced current was found to be linearly dependent on the dose rate[60].

Radiation induced current (RIC) in the conductor degrades the image quality. Unlike thermal noise, the effect of RIC appears as stripes in the k-space data of acquired images, rather than constant across frequency. The effect of this spurious signal has been studied experimentally in linac-MR systems at 0.2 T, where it was found to degrade SNR by up to 18% when the linac delivered a dose rate of 250 MU/min to a 3 cm diameter solenoid RF-coil[34]. Simulations of RIC in different magnetic field strengths and orientations showed that RIC was independent of the magnetic field. [35] In investigations of a dedicated MR-linac RF-coil, RIC was also seen in a 1.5T MR-linac. The SNR loss due to RIC was significantly lower at 1.5T with a beam delivering 680 MU/min causing a maximum SNR loss of 5% [31]. The degradation is lower at larger field strengths because the voltage from precession of magnetization increases with a square of the field strength (Equation (2.23)), while the RIC is proportional to dose rate and independent of field strength[35]. The effect of RIC cannot be predicted from field strength and dose rate alone, as it also depends on elements such as scan parameters and the noise floor[31, 35].

Several methods to reduce the impact of RIC have been proposed. The simplest mitigation method is to keep the conductor out of the radiation field. This eliminates RIC as a source of image quality degradation. Another option is to add build-up to the conductor. There will be electrons ejected from the build-up that enter the conductor, offsetting the electrons ejected. This method was used to restore over half the SNR loss associated with RIC (11% SNR loss without build-up, 5% SNR loss with 18.5 mm of Teflon build-up)[34]. A third method is post-processing of the k-space data to edit out spikes in the noise regions that exceeded 3 standard-devations of the background. This was used to recover up to 81% of the SNR loss due to RIC in certain conditions[35]. Based on simulations of different field strengths, the mitigation methods investigate at 0.2T should also perform similarly at different field strengths[34, 35].

2.1.7.1 RF-Coil Quality and Link to SNR

RF-coil design and construction aim to provide the best image quality given constraints on material, positioning, and any other requirements. A common quantity used to measure how well a coil performs is its quality factor (Q), defined as ω times the electromagnetic energy stored in the RF-coil relative to how quickly energy is dissipated when a current flows in the coil.

Recall that an RF-coil is just a conducting loop, which can be described in terms of lumped components as a series inductance (L, the coils self-inductance as determined by the loop geometry) and a series resistance (r, the total resistance of the loop as determined by the resistivity of the conductor, cross-sectional current density and length). The loop then has an impedance given by:

$$Z_{coil} = r + j\omega L \tag{2.56}$$

For a given sinusoidal current (I) generated by an applied voltage or induced emf it is possible to write the power dissipated:

$$\frac{dE_{lost}}{dt} = I^2 r \tag{2.57}$$

and the rate of energy storage in the circuit:

$$\frac{dE_{stored}}{dt} = IL\frac{dI}{dt} = I^2 \omega L \tag{2.58}$$

The quality Q then is given by the ratio:

$$Q = \frac{\omega L}{r} \tag{2.59}$$

The relationship between RF-coil quality and SNR is described by efficiency (η)[53]:

$$\begin{aligned} \eta =& 1 - \frac{1}{Q_{ratio}} \\ SNR =& \sqrt{\eta}\ iSNR \end{aligned} \tag{2.60}$$

This relationship states that for given proximity and arrangement of a coil and the sample there is some theoretically achievable maximum SNR (iSNR). The signal-to-noise ratio (SNR) that will be achieved by a particular coil is describe by the efficiency of that coil (η). Efficiency describes what fraction of the losses cannot be assigned to the coil. That is if the coil itself is lossless, the efficiency should be unitary. To determine efficiency we measure the quality Q of the coil in isolation, termed Q unloaded (Q_U). In this case Q is given as above based on the inductance of the conductor loop and the conductors resistivity. Note that this assumes that the capacitor needed to resonate the loop is lossless. To determine the contribution of the non-coil losses as discussed in Section 2.1.6.3, the Q is measured with the coil set up as it will be used for imaging. In this case the total energy lost is determined by the total losses (r_{tot}):

$$r_{tot} = r_{coil} + r_{sample} \tag{2.61}$$

This is termed the loaded Q (Q_L):

$$Q_L = \frac{\omega L}{r_{coil} + r_{Sample}} \tag{2.62}$$

The efficiency is then simply given by:[53]

$$\eta = 1 - \frac{Q_L}{Q_U} = 1 - \frac{r_{coil}}{r_{coil} + r_{sample}} = \frac{r_{sample}}{r_{tot}} \tag{2.63}$$

Based on the measured efficiency, the losses are described as sample dominated ($\eta > 0.5$) or coil dominated ($\eta < 0.5$). The goal should always be to have losses be sample dominated. This can be achieved by having high quality coils with very low coil resistance, r_{coil}. Depending on the proximity of the coil to the sample and operational frequency however, the requirements on the coil resistance can be strict or more relaxed. A shorter distance between the coil and the sample leads to more magnetic losses in the sample. The amount that the sample impacts the coil losses is termed loading. Loading depends on the relative geometry, relative proximity, and the sample size. There is also a power of two relationship between operating frequency (Larmor frequency is determined by B_0) and sample losses (see Equation (2.42)).

Conversely the requirements on the coil may limit how low a resistance can be achieved. Use of different conductors changes the resistivity, potentially increasing or decreasing coil losses. Longer lengths of conductor will yield more total resistance. And as frequency increases the current density becomes less uniform and more crowded near conductor surfaces, increasing resistance per unit length.

The goal in coil design is to select a geometry that will have a high intrinsic SNR (i.e., increase $\vec{S}_p$, Equation (2.24)) and construct the coil in a way that maximizes efficiency (i.e., minimize r_{coil}/r_{tot}). The design, construction, and field strength will all influence both intrinsic SNR and efficiency. For example, mechanical design constraints can limit the coupling (distance) between the coil and sample, and if the coupling is low even small r_{coil} can lead to poor efficiency.

2.1.7.2 RF-Coil Tuning

While Faraday's description of induction does not require the transmitting or receiving device to be a resonator, to maximize sensitivity RF-coils are almost always RF resonators tuned to the Larmor frequency. This is achieved by the use passive devices, specifically conductors and inductors, to match the receiving/transmitting device to amplifiers.

Loop impedance is described by Equation (2.56) and must be matched using low-loss components to the characteristic impedance of coaxial cable (typically 50 Ω). Because signal bandwidths are small ($\sim 1\%$), it is sufficient to use narrowband matching with reactive components (capacitors and inductors). [38] In the transmit case, the coil is acting as the load, and must be matched to avoid power wasting reflections that lower Tx coil efficiency (eq. (2.30)). In the receive case, the coil must be matched to the optimal source impedance (Z_{opt}) of low noise amplifiers to amplify the small signal voltages without introducing much noise [61].

Consider a desired impedance (Z_0, typically real) written in the form:

$$Z_0 = r_0 + jX_0 \tag{2.64}$$

The coil impedence (Z_{coil}) can be matched to Z_0 by a minimal lossless matching network consisting of two reactive elements, with one in parallel and one in series. First, the coil is tuned, through the introduction of a reactive component (X_t) in parallel to Z_{coil}. X_t is such that the real part of the combined impedance (Z_{comb}) equals Z_0.

$$Z_0 = Re(Z_{comb}) = Re\left(\left({Z_{coil}}^{-1} + (jX_t)^{-1}\right)^{-1}\right) \tag{2.65}$$

When the resistive component of the coil is small relative to $\mathrm{Z_0}$ and $\mathrm{X_t}$, then the requirement on X_t to first order becomes:

$$X_t = -X_{coil} = -\omega L \tag{2.66}$$

which describes adding a capacitor (C_t) in parallel with a value that satisfies the LC circuit relationship

$$LC_t = \omega^{-2} \tag{2.67}$$

By changing the capacitor value, the frequency (ω_s) at which a match is achieved is changed or tuned.

$$\omega_s = \frac{1}{\sqrt{LC_t}} \tag{2.68}$$

As the highest priority signals are those at the Larmor frequency, the system is typically tuned such that $\omega_s = \omega_0$.

The remaining reactive component of the combined impedance $Im(Z_{comb})$ can be set equal to the imaginary component of Z_0 (i.e., zero in the case of a lossless transmission line), by an appropriate series reactive component (X_m).

$$Im(Z_0) = Im(Z_{comb}) + X_m \tag{2.69}$$

Typically a remaining positive imaginary component is cancelled by an equal but opposite reactive impedance produced by a series capacitor termed the matching capacitor (C_m).

$$C_m = \omega_s^{-1} Im(Z_{comb})^{-1} \tag{2.70}$$

Matching, similarly to tuning, is frequency dependent and the frequency at which the imaginary component is negated should also be ω_s.

The usage of only reactive components is to avoid introducing additional losses to the system. However, the use of reactive components means the matching condition is only satisfied well in a narrow band of frequencies around ω_s. To best couple to the sample this should be the made the same as the Larmor frequency (ω_0) of the nuclei of interest[40].

Practically, the right tuning and matching capacitor values can be found through the use of a vector network analyzer (VNA). A VNA is used to measure the coils response to signal, from a 50 Ω source, that scans across a desired band of frequencies. A vector network analyzer measures the voltage at some number of ports, typically for a single coil, a two-port network analyzer is sufficient. In a two-port system, one port is designated as the source, network analyzer sends test RF-waves spanning a band of frequencies from this port, and then measures the reflected power at the same port (an S_{11} measurement) and the power transmitted to the other port (an S_{21} measurement).

The co-axial cable of the coil is connected to one port and a small (e.g., 10 times smaller diameter than the coil) sniffer probe is connected to the other (Figure 2.12). The transmitted power in this arrangement gives the frequency dependence of the magnetic coupling between the coil and the probe. There will be a peak at the frequency for which the real part of the coil impedance matches the characteristic impedance ($Z_0 = 50\ \Omega$). This is because the peak is dominated by the LC properties of the coil as described by Equation (2.67). Adjusting the tuning capacitor will shift this peak, and typically a variable capacitor is used to bring the peak right to the desired frequency ω_0.

The right value for the matching capacitor can then be found by looking at the return loss (S_{11}) at the coil port (Figure 2.13)[38]. By adjusting the matching capacitor the remaining imaginary component can be cancelled at ω_s leading to a minimum return loss or 50 Ω match. Both the tuning and matching capacitor impact the value of ω_s so often some additional iterations of adjustments to the capacitor values are needed to achieve $\omega_s = \omega_0$.

It is important to note that the tuning and matching capacitors depend on the effective resistance of the coil (see Equation (2.65) and Equation (2.56)). This means as the loading changes, the tuning and matching capacitors need to be fine tuned, a further reason why variable capacitors are commonly used.

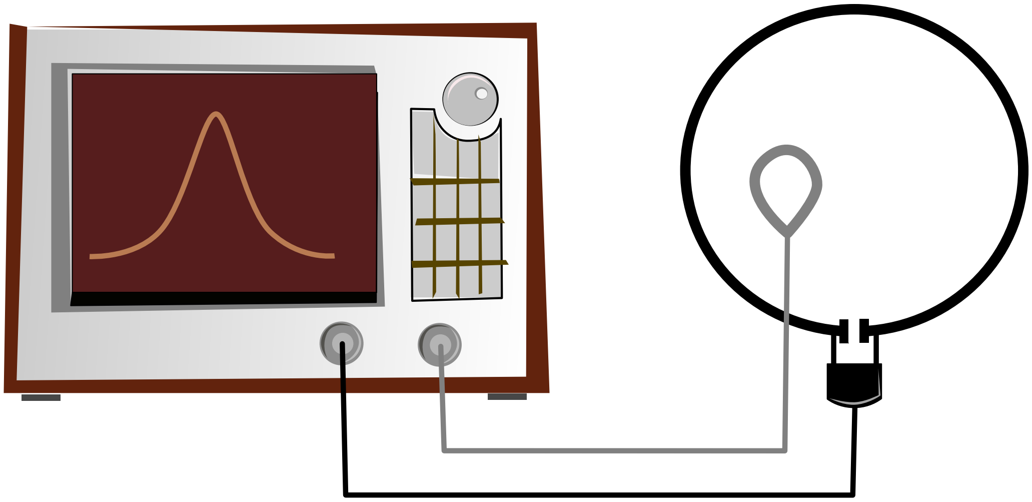

Figure 2.12: The first port of the Vector Network Analyzer is connected to the matched coil. A sniffer probe is connected to the second port. The vector network analyzer displays the characteristic Lorentzian line shape that occurs near the resonant frequency of the coil. Signal at this frequency is best able to couple from the coil to the probe, which suggests the coil will best couple to precession in the sample at this frequency. This frequency should match the Larmor frequency of interest. Pavel Barta ©. Used with Permission.

The S21 measurement in addition to playing a role in tuning is also relevant for measuring Q. The lower the losses in the coil, the narrower the band of frequencies for which the transmitted power is at least half the maximum transmitted power (3dB below the maximum). The measurement of the 3 dB bandwidth on a vector network analyzer of the S21 frequency response is a proxy for the losses in the coil and the ratio of the central frequency to the bandwidth is equal to the quality factor of the coil[40].

$$Q = \frac{f_c}{\delta f} = \frac{\omega L}{R} = \frac{1}{\omega C R} \tag{2.71}$$

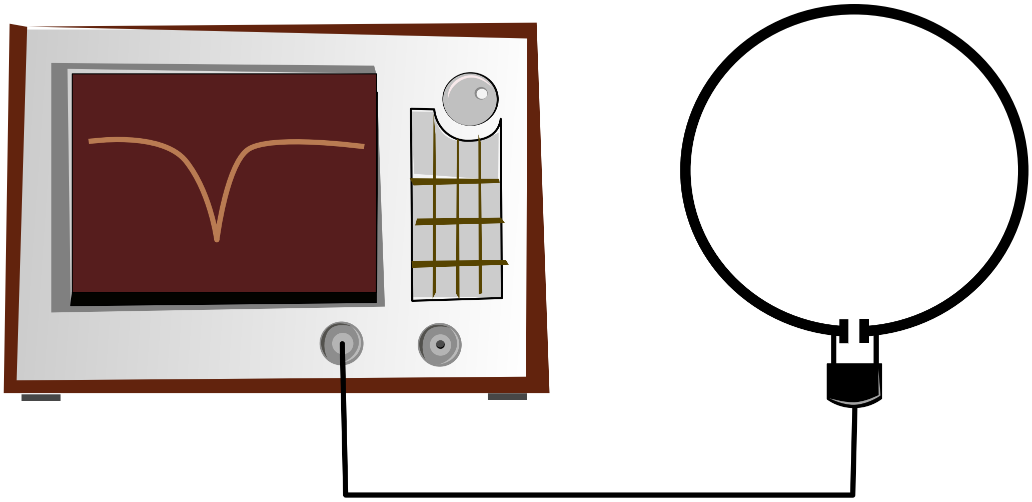

Figure 2.13: The first port of a vector network analyzer is connected to a the coil through a matching network (box between coil and cable). The dip shown is the low reflection loss that is achieved when the matching network has been adjusted to achieve the best power loss match between the cable (50 Ω) and the coil. This is the right match if the pre-amplifier that is used with this coil expects a 50 Ω impedance for optimal noise characteristics. Pavel Barta ©. Used with Permission.

2.1.7.3 Detuning Traps

Receive only coils use detuning traps to stop the flow of currents in the coil during excitation. During excitation the transmit coil, typically the body coil, generates strong RF-fields, which would induce an emf in the RF-coil. The resulting current would generate a magnetic field opposing the excitation, hence ruining the desired excitation. To avoid this, a series combination of crossed diodes and an inductor is placed in parallel to each tuning capacitor. The crossed diodes will act as an open circuit during receiving when induced emf is low. However when the coil is experiencing the high emf due to active transmit fields, the diodes will conduct creating an alternate path past the capacitor. The inductor is selected such that the parallel pair of capacitor and inductor act as a very high impedance at the Larmor frequency for any currents that would flow in the coil loop. The impedance of the pair:

$$Z_{LC} = \left((j\omega L)^{-1} + j\omega C\right)^{-1} \tag{2.72}$$

becomes undefined for $\omega = (LC)^{-\frac{1}{2}}$. So the right selection of inductor ensures no current flow (at frequency $\omega = \omega_0$) during excitation. An active bias can be applied in a synchronized manner with the transmit and receive instructions sent by the control computer. The passive system is commonly used as a backup in case the active detuning fails.

2.1.8 B$_1$ Field Maps

An important measurement in MRI is acquiring a B_1 map. Measuring B_1^+, the component of the B$_1$ co-rotating with the precession (Equation (2.29)), gives confirmation that the transmit coil uniformly excites the phantom and can be used to calibrate transmit power to achieve a desired flip angle. Uniform excitation is also verification that any receive-only coils used are detuned during transmission and do not impact the spatial distribution of excitation.

There are many B_1 mapping techniques, but an effective and long used method is the double-angle method [62, 63]. The double-angle method consists of acquiring two images using a gradient echo sequence with two different flip angles (α_1 and α_2) where the second is double the first. The signal acquired in each case then is proportional to $\sin(\alpha_1)$ and $\sin(\alpha_2)$, respectively. The flip angle is proportional to $\gamma B_1^+ t_{pulse}$, where t_{pulse} is the pulse duration. By taking the ratio of the two images, all common factors can be eliminated

$$\frac{I_1}{I_2} = \frac{sin(\alpha_1)}{sin(\alpha_2)} \tag{2.73}$$

since $\alpha_2 = 2\alpha_1$:

$$\begin{gathered} \frac{I_1}{I_2} = \frac{sin(\alpha_1)}{sin(2\alpha_1)} = \frac{sin(\alpha_1)}{2sin(\alpha_1)\cos(\alpha_1)} \\ \cos^{-1}(\frac{I_2}{2I_1}) = \alpha_1 \propto B_1^+ \end{gathered} \tag{2.74}$$

So by acquiring two images, the flip angle α_1, which is proportional to B_1^+ can be mapped. [62]

2.1.9 Arrays, Coupling, and Image Combination

It is common in MRI to use multiple receive RF-coils simultaneously (RF-coil array). The purpose is to combine coil signals to cover larger target volumes and to increase sensitivity. In general signals from the various coils are correlated, meaning the information collected from one is not strictly independent of the others. The methods used to combine the images from multiple coils are characterized by whether they correct for sensitivity and noise correlation. Which method can be used depends on whether this information has been collected or not.

The simplest method is merely to combine the images in a root sum of squares (RSS) fashion and can be used in any circumstance. In this case no additional information other than the individual coil signals is needed. One downside of this method is that the variation in spatial sensitivity of the various coils will bias the combined image[64, 65].

If the sensitivity profile at all positions for each coil in the array is known, then a sensitivity-based method can be used. The voxel values are scaled by the sensitivity of each coil at that point, and summed, then normalized by dividing by the root sum of squares of the sensitivities. This accounts for sensitivity variation but not the variation in SNR[64, 65].

The SNR optimal or Roemer method can be used when the sensitivity and noise information about the array is known. This method weighs the contribution of each coil by the sensitivity and the noise in that channel. This favours contributions from highest sensitivity and lowest noise coils, and generates the best voxel by voxel SNR combined image, but requires the most a priori information. [64, 65]

When coil sensitivity is not known, the noise information can still be used with the weighted root sum of squares (wRSS) method. The channels are combined according to the Roemer method with the assumption that the sensitivity is proportional to the signal in the channel. This leads to a sum of squares but with low noise channels being weighed more heavily. This method is attractive because noise information is desirable to acquire to evaluate SNR, and this method does not require additional scans to measure the individual channel sensitivities. [64, 65] Explicitly the wRSS method voxel by voxel is given by:

$$p = \sqrt{< s_1, s_2 ... > \psi^{-1} < s_1, s_2, s_3 ... >'} \tag{2.75}$$

Where ψ is the noise covariance matrix

$$\psi = \mathrm{cor}(< n_1, n_2, n_3 ... >, < n_1, n_2, n_3 ... >) \tag{2.76}$$

s_i and n_i are the signal and noise at that particular voxel from the ith coil in the array.

This particular expression for the combination image also is already scaled so that the noise is uniform across the image. Uniform noise scaling also means that the voxel values are equal to the combined SNR values. This makes it very practical for evaluating and using coil arrays[64].

One of the key aspects of building and using RF-coil arrays is to try and have each channel contribute independent signal to the combined image. This is achieved by having low coupling between the various channels. The effect on image SNR can be seen in Equation (2.75). Low coupling between channels means the cross-terms in the covariance matrix (Equation (2.76)) will be smaller, hence the voxel values will be higher because its inverse is seen in the equation for p.

Coupling arises due to the mutual inductance of two inductors that are near each other. Coupling between resonant loops alters the effective inductance of each resonator, and typically generates various resonance modes depending on the various options for relative currents. Good decoupling can be achieved through geometry. The simplest example of decoupling is the use of orthogonal coils, where one loop is

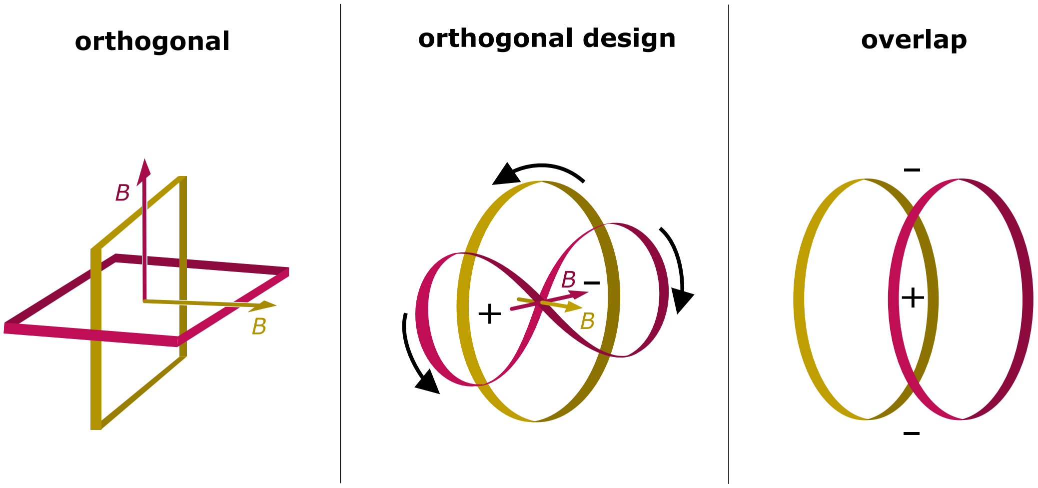

Figure 2.14: Three methods of decoupling two different coils for construction of coil arrays. Left shows decoupling through orthogonal orientation of two similar coils. Middle shows decoupling through choice of two coils (single turn, yellow, and figure-eight or butterfly, red) which are primarily sensitive to orthogonal RF fields. Right shows decoupling though optimal overlap where the positive coupling in the overlapped region precisely compensates for the negative coupling of the not overlapped coil regions. In each case the positive and negative mutual coupling have to cancel to achieve two uncoupled coils that will then detect uncorrelated signal and have uncorrelated noise. Pavel Barta ©. Used with Permission.

rotated 90° with respect to another as in Figure 2.14. Another option is two concentric coils each designed to couple to separate orthogonal axes, such as by combining a single turn coil with a figure-eight (butterfly) coil (Figure 2.14). Partial overlap is a method often used when parallel coils are used to cover a larger field of view[65]. The mutual inductance between two adjacent loops is offset by the opposite sign mutual inductance from the overlapped region (Figure 2.14). Alternatively the adjacent coupling can be offset through the introduction of coupling networks between adjacent coils[40].

2.2 External Beam Radiation

2.2.1 Linear Accelerator

The other primary component of the linac-MR is the linear accelerator. The linear accelerator generates the photon and electron radiation that is used to treat cancer with radiotherapy. The linear accelerator (Figure 2.15) consists of a pulsed power supply, klystron or magnetron, electron gun, accelerating structure, in some systems a bending magnet, a target or scattering foil, and collimation structures[66].

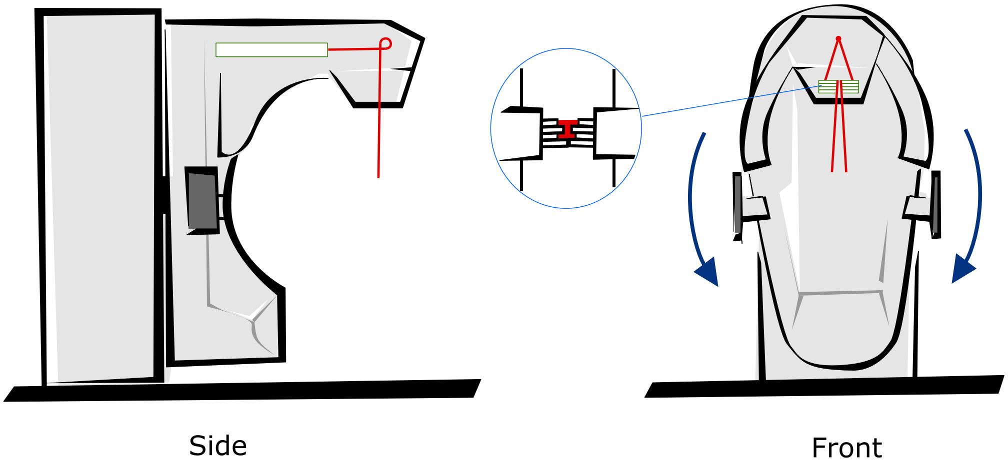

Figure 2.15: A depiction of a clinical linear accelerator from the side and front. The head of the linac is where the bending magnet, target, and collimation are located. The straight part connected to the head holds the electron gun and the accelerating structure. The stand holds the pulsed power supply and the klystron which feeds the accelerating structure. Pavel Barta ©. Used with Permission.

The pulsed power supply generates RF-pulses to trigger the klystron and electron gun in a synchronized manner. The klystron generates the high power RF pulses that accelerate the electrons produced by the electron gun. The electrons are accelerated through multiple resonant cavities of the accelerating structure and then enter the head of the linac. In non-bending magnet linacs, the accelerating structure is in line with the target or scattering foil. In systems with longer accelerating structures, a bending magnet curves the electrons in a 270° loop to align the electrons with the target axis. To generate a photon beam a metal target is used to slow and stop the electrons. As the electrons decelerate the lost energy is given off, in part, as Bremsstrahlung radiation. The broad-beam Bremsstrahlung radiation is collimated with movable jaws and a multi-leaf collimator (MLC) to define a specific beam shape. To generate an electron beam suitable for treatment, the electrons instead strike a scattering foil which scatters the pencil beam of electrons into an electron cone beam. An electron beam is collimated using a field size specific collimator attachment and lead inserts to define specific shapes.

2.2.1.1 Klystron

A klystron consists of a cathode and an anode connected by a drift tube[66]. At the cathode, electrons are produced continuously by thermionic emission, focused by electric fields, and accelerated by a high voltage. The electrons pass through the buncher cavity where the input microwave power enters. The low power microwave input signal excites the cavity.

As the electrons pass through the cavity, they will be either accelerated or decelerated in the short gap between the two apertures. The electrons then drift through the tube (hence drift tube) and accelerated electrons will catch up to decelerated electrons. The length of the drift tube is designed to maximize the bunching of the the electrons as they arrive at the collector cavity[66].

The bunched electrons generate a strong electric field proportional to the number of electrons as they approach and then an equal and opposite field as they exit. This alternating electric field induces an alternating magnetic field, resulting in RF-wave that is many times more powerful than the original RF wave used to bunch the electrons. The energy in the DC flow of many electrons has been converted to RF-power[66]. The high power RF-wave is guided from the klystron to the accelerating structure by a waveguide.

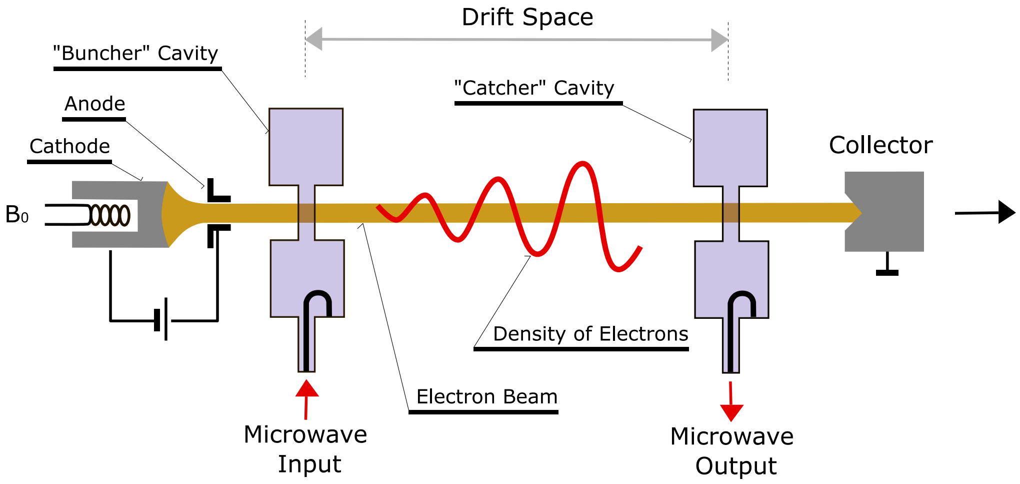

Figure 2.16: A klystron with its the microwave input and output shown separated by a drift space. Electrons generated at the cathode by thermionic emission clump together due to the timing based acceleration or deceleration of individual electrons in the buncher cavity. Accelerated electrons catch up to decelerated ones. With the right drift space length, the electrons arrive in large bunches depositing a many times multiplied amount of energy into the catcher cavity, resulting in an amplified microwave output. Direct current energy of the electrons is converted into RF energy thanks to the periodic arrival of the electron bunches. Original figure by Charly Whisky, remixed in accordance with the BY-SA 3.0 license. This figure courtesy of Pavel Barta, CC BY-SA 4.0, https://creativecommons.org/licenses/by-sa/4.0/legalcode..

2.2.1.2 Magnetron

Some linear accelerators use a magnetron instead of a klystron to generate the accelerating RF waves. A magnetron consists of a series of identical cavities arranged in a circle around a central cathode. The cavities are positively charged so that electrons emitted (thermionic process) by the cathode are accelerated towards the anode (the cavities) by a static electric field. A large magnet is added to generate a magnetic field along the cathode axis, causing the electrons to travel along a curved path from cathode to anode. As electrons pass by the opening of each cavity, they will lose energy and excite the resonance modes of the cavities. The resonant electromagnetic field in the cavities helps to focus the accelerating electrons into rotating spokes that will continue to feed energy into the RF-field.

2.2.1.3 Electron Gun

The electrons that will be accelerated are produced through thermionic emission in the electron gun. Heating of a current carrying wire causes electrons to be ejected from the wire into the space near the wire[66]. A reversible electric field or gate, pulls groups of electrons into the accelerating structure in time with the microwave pulses coming from the klystron or magnetron.

2.2.1.4 Accelerating Structure

The accelerating structure consists of multiple resonance cavities with similar designs as the cavities described in the klystron. In a typical linear accelerator the electrons are accelerated by a standing wave[66]. In a standing wave accelerator, the accelerating structure has an input and the electromagnetic field travels up and down the structure setting up a standing wave[66]. In each cavity travelling electrons are accelerated by the electric field across the aperture, which is alternating due to the standing electromagnetic wave. The period of the standing wave by design is such that electrons accelerated in the first cavity will arrive at the center of each subsequent cavity when the electric field in the cavity reaches a maximum. These electrons form a traveling group.

Electrons slightly ahead of the group will enter the next cavity early, and experience some initial deceleration, bunching it with the slightly slower, more closely phase matched, electrons[66]. The electron beam is bunched into dense packets of high energy electrons. In general the total kinetic energy gained is given by the product of the charge on an electron and the sum of the potentials experienced in each cavity. Many clinical systems also have the ability to shift between energies by partially degrading the coupling between cavities. While the RF-input parameters in the first cavity remain the same, the reduced coupling weakens the electric fields generated in subsequent cavities, reducing the acceleration achieved for each electron. The total accelerating potential (ie. 6 MV, 10 MV, or 15 MV) is a typical way of identifying the linear accelerator and the photon beam it generates.

2.2.1.5 Bending Magnet and Target

When the electron beam exits the linac accelerating structure it enters the linac head. In lower energy linear accelerators the accelerating structure can be short enough to be in-line with the target, in high energy ($\geq$ 10 MV) linear accelerator, however, the the accelerating structure is orthogonal to the desired photon beam. In this case a magnet bends the electron beam 270° and focus the beam to hit the target[66]. On striking the target the electrons generate photons through bremsstrahlung radiation (see Section 2.2.2). Low energy accelerators typically use tungsten while for high energy accelerators copper is preferred[66]. The bremsstrahlung generated photon beam is forward peaked and has a broad energy spectrum, with a maximum energy equal to that of the electrons incident on the target.

2.2.1.6 Photon Beam

Even though a broad range of photons is generated in the target, low energy photons are attenuated out of the beam by the target itself. The photon beam will not have very low energy photons and not many at the peak energy. Additionally, the spatial distribution of the photons will be focused around the center of the beam; in-line with where the electrons struck the target. The higher the electron energy the more forward peaked the photon spectrum. The primary collimator, a piece of metal with a conical hole, and the shielding around the linac head limit the photon radiation to a directional beam.

A flat dose profile across the extent of the radiation beam is achieved by introducing a flattening filter, a conical shape, typically made of copper or other medium-Z materials, which attenuates the center of beam more than the edges to compensate for the higher photon fluence at the center of the beam. Beam flatness comes at a cost as attenuation decreases dose rate. In some treatments the photon beam is used without any flattening filter. So called flattening filter free delivery provides treatment beams with a higher dose rate and spatial variation of the fluence across the beam is accounted for during treatment planning.

The flattened or un-flattened photon beam is collimated by tungsten jaws and a tungsten multi-leaf collimator (MLC). Jaws are a pair of thick tungsten blocks that move across the beam to block all but a strip of the photon beam. Photons striking the thick tungsten blocks are attenuated out of the beam. Two sets of jaws, rotated 90° relative to one another, can be used to generate any desired rectangular beam shape. The MLC is a set of thin metal leaves that can be moved independently to generate a desired pattern, shaping the beam. Alternately, some linacs use a single set of jaws, and use thicker MLC leaves at 90° to the jaw axis to act as either a second jaw or an MLC.

The collimated photon beam travels from the linac head to strike the the patient. The energy in the beam is transferred to the patient, and is quantified by the energy deposited per unit of mass (J/kg) or gray (Gy). The radiation dose delivered to the patient is the result of specific interactions of photons and electrons with the patient's tissues.

2.2.2 Radiation and Matter Interactions

2.2.2.1 Electrons

Electrons are charged particles and interact strongly with both positively charged atomic nuclei and negatively charged atomic electrons in matter. These strong interactions limit electron motion through matter. Electrons deposit energy locally to the medium through many individual energy transfers. The higher their energy, the further electrons travel before losing all their energy. The range of an electron is the expected total distance it will travel before losing all its energy. According to the continuous slowing down approximation (CSDA), in water, an electron's range in centimeters is half of its initial energy in mega electron volts (MeV)[67]. This is the distance traveled along the electrons trajectory, since it experiences multiple interactions that change its direction of travel. The distance from where the electron is created (or enters a material) to where it loses all its energy will always be less than the range.

Electron interactions can be categorized into collisional and radiative events. Collisional events are the most common and occur when an electron transfers some of its energy to an atom in the medium. In a collisional event most of the energy is deposited locally. Radiative events are where the energy lost by the electron generates one or more photons which carry the energy far from where the interaction occurred.

Collisional events are usually ionizing events where the traveling electron interacts with a bound electron ejecting it. The result is two energetic electrons and an ionized atom (Since electrons are indistinguishable, the higher energy electron is labeled as incident). In the ionized atom, electrons in higher energy orbitals than the ejected electron fall down to the vacated lower energy states. As electrons cascade down energy levels, with each transition energy is emitted as characteristic x-rays. A competing mechanism is when the transition energy is absorbed by a bound electron (in a higher energy state), ejecting it. Such ejected electrons are termed Auger electron. The dominant energy transfer in a collisional event is to the ionized electron, and characteristic x-rays are very low energy, therefore the transferred energy is deposited locally[68]. The rate at which electrons lose energy through collisional events to the medium is described my the mass collisional stopping power $\left(\frac{L}{\rho}\right)_{col}$, the density-scaled energy loss per unit distance ($MeVg^{-1}cm^{2}$)[68, 69].

The mass collisional stopping power is proportional to the electron density of the medium, and below about 1 MeV it varies appreciably with electron energy[68, 69]. Above 1 MeV:

$$\left(\frac{L}{\rho}\right)_{col} \propto \frac{N_A Z_A}{A_M} \tag{2.77}$$

In radiative events, the electron interacts with a positive nucleus. The attractive force causes the electron to decelerate and bend as it passes an atom. The energy lost by the electron as it slows is given off as photons. These photons are called bremsstrahlung or breaking radiation. The maximum bremsstrahlung is generated with an electron strikes an atomic nucleus head on and all of its incident kinetic energy is emitted as a photon. An electron may slow down numerous times in arbitrary increments and consequently bremsstrahlung photons have a continuous energy spectrum. Photons do not interact as readily as electrons (Section 2.2.2.3) and the transferred energy is not deposited locally[68]. The rate of energy loss through the radiative process is described by the mass radiative stopping power ($\frac{L_{rad}}{\rho}$).

The mass radiative stopping power is approximately proportional the atomic number squared and the electron energy [68, 69].

$$\left(\frac{L}{\rho}\right)_{rad} \propto \frac{N_A E_e Z_A^2}{A_M} \tag{2.78}$$

Above 1 MeV where collisional mass stopping power is independent of electron energy, it is instructive, from a photon beam generation perspective, to look at the ratio of mass stopping powers. This describes the bremsstrahlung yield in the linac target due to the incident electron beam[68].

$$\frac{\left(\frac{L}{\rho}\right)_{rad}}{\left(\frac{L}{\rho}\right)_{col}} \approx \frac{E_e Z_A}{700 MeV} \tag{2.79}$$

This means that using a tungsten target ($\mathrm{Z_A} = 74$) and a 6 MeV electron beam gives a yield of about 63%, that is 37% of the incident energy will be lost in the target due to collisional interactions. Additionally, not all bremsstrahlung photons escape the target, some, especially low energy ones, will be absorbed by the target[68].

2.2.2.2 Electrons in a Magnetic Field

In MR guided radiotherapy, electrons experience Lorentz forces due to an external magnetic field (B_0) (Figure 2.17). The force on an electron (charge q_e) in an external magnetic field is described by:

$$\vec{F} = q\vec{v} \times \vec{B} = -q_e\vec{v} \times \hat{z}B_0 \tag{2.80}$$

$$\frac{d\vec{v}}{dt} = \frac{q_e B_0}{m_e} \langle v_y, v_x, 0 \rangle \tag{2.81}$$

In constant external magnetic field, the parallel velocity (v_z) is constant as it does not experience a force. The perpendicular velocity, however, experiences an acceleration perpendicular to its direction this describes in the absence of a parallel velocity a circular orbit (Figure 2.17). The radius, r, of this path is given by ratio of the parallel momentum to the product of the charge on the electron and the external magnetic field.

$$r = \frac{m_e v_\perp}{q_e B_0} \tag{2.82}$$

The higher the momentum (and thus energy) of the electron the larger the radius. The stronger the magnetic field, the tighter the curvature in the perpendicular plane. Combining the parallel and perpendicular components, the electron will follow a helical path co-axial with the external field.

In the case where the B_0 is parallel to the beam axis (dominant momentum axis), the helix of the electrons generated in the air and in the patient will be along the beam axis. Electrons in the air will be somewhat focused if the field strengthens as they travel, as the radius of the helix decreases as field strength increases and in the patient, the spread of the scatter electrons will be slightly reduced.

In the case of a B_0 that is primarily perpendicular to the beam axis, the electrons will travel in a helix along the magnetic field and hence away from the patient. An electron produced in the air will not strike the patient if its energy is low enough that the radius of its helix is less than the distance to the patient surface. In the patient, electron paths will curve perpendicular to the beam direction, resulting in a shifting of the energy deposition to one side of the patient. And on the exit side of the patient, the electrons will be curved back towards the patient due to the perpendicular field.

The Lorentz force on electrons distinguishes radiation interactions in matter between MR guided treatment and traditional treatment.

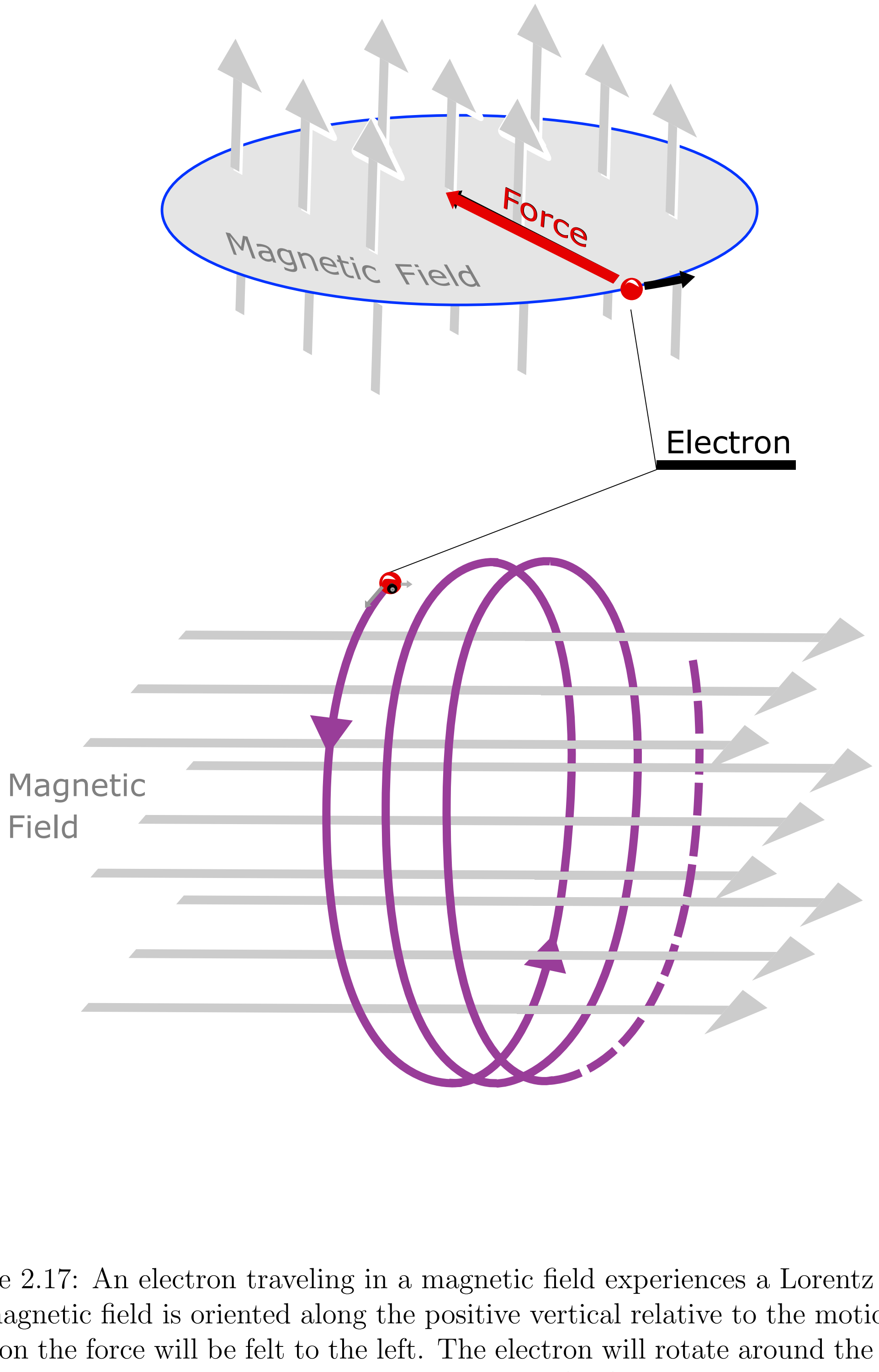

Figure 2.17: An electron traveling in a magnetic field experiences a Lorentz force. If the magnetic field is oriented along the positive vertical relative to the motion of the electron the force will be felt to the left. The electron will rotate around the external magnetic field axis in a counter-clockwise manner (top). The velocity parallel to the magnetic field in a constant field is unaffected resulting in a helical patch (bottom). Pavel Barta ©. Used with permission.

2.2.2.3 Photons

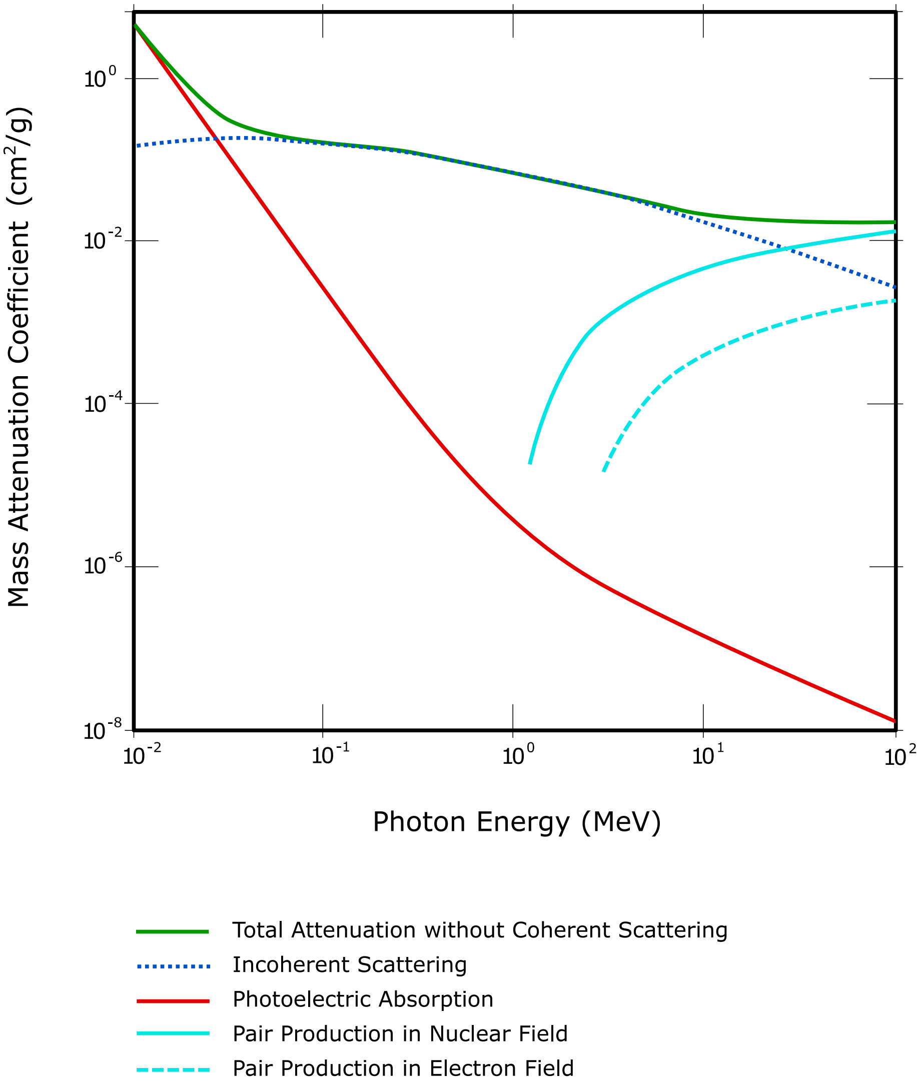

Figure 2.18: The mass attenuation of photons (cm^2/g) in water as a function of energy (MeV). Shown are total attenuation (ignoring coherent scattering) and the individual contributions from the photoelectric effect (σ_{pe}), incoherent (Compton) scattering (σ_{inc}, pair production in a nuclear field (σ_{pp}), and triplet production (pair production in an electron field σ_{tp}). Adapted from NIST [70]. Pavel Barta ©. Used with permission.

Photons are uncharged and interact more rarely than electrons. Some photons may not even interact in the patient and the photons that do may only experience a few interactions in patient. Photons nevertheless interact with matter in numerous ways. Photons are scattered in Compton interactions with electrons, absorbed by atoms through the photoelectric effect, and can generate an electron-positron pair near an atom through pair production. Rarer events like triplet production are possible but do not play a significant role in dose deposition. Photons can also be scattered in energy conserving interactions like Rayleigh scattering that attenuate the beam, but do not contribute to dose deposition.

Compton scattering is the dominant interaction relevant to radiation therapy. Compton scattering describes the scattering of a photon by a free electron. At the energies seen in radiation therapy, atomic electrons behave almost like free electrons for the purposes of Compton interactions. The probability of interacting with matter through Compton scattering thus is very dependent on the electron density and thus the atomic Compton scattering cross-section is proportional to the atomic number.

$$\sigma_{inc} \propto Z_A \tag{2.83}$$

The differential Compton scattering cross-section for scattering into a particular solid angle ($\frac{d\sigma}{d\Omega}$) is described by the Klein-Nishina equation [71]

$$\frac{d\sigma}{d\Omega} = \frac{1}{2} r_e^2 \left(\frac{E_f}{E_i}\right)^2 \left[\frac{E_f}{E_i} + \frac{E_i}{E_f} - \sin^2(\theta)\right] \tag{2.84}$$

where r_e^2 is the classical electron radius, E_i is the incident photon energy, and E_f is the energy of the scattered photon. The larger the angle of photon scatter, the more energy is transferred to the electron. By conservation of momentum and energy the transferred energy is given by:

$$E_{tr} = E_i - E_f = \frac{\frac{E_i^2}{E_e^0}\left(1 - \cos\theta\right)}{1 + \frac{E_i}{E_e^0}\left(1 - \cos\theta\right)} \tag{2.85}$$

Where E_e^0 is the electron rest energy.

At low photon energies the probability to scatter forward or backward is approximately equal. At high energy, the scattering becomes forward peaked, as forward scatter is more likely than scattering backwards. The Compton interaction probability increases approximately proportionally to the photon energy at low energies, and falls off with the inverse of the energy at high energies, transitioning between the two dependencies by a gradual curve between ≈10 keV and ≈1 MeV[68].

Less relevant in clinical radiotherapy, the photoelectric effect dominates at low energies. The photoelectric effect is the interaction between a photon and an atom where the photon is absorbed and an electron is excited, either raising it to an available higher energy level or ejecting it from the atom. Like in the case discussed for electrons, the lower energy state vacancy, in an atom, leads to a cascade of electrons filling the lowest available energy states. The excess energy is emitted as characteristic x-rays or Auger electrons. The photoelectric effect is very dependent on photon energy and atomic number. The higher the atomic number, the larger the cross-section, and for a specific atomic species, the cross-section generally decreases with increased energy[68].

$$\sigma_{pe} \propto \frac{Z_A^4}{E^3} \tag{2.86}$$

At energies greater than 1 MeV the pair production interaction is possible though the Compton effect still dominates even up to 10 MeV[72]. Pair production is when a photons energy is totally converted into an electron-positron pair. A photon can only undergo this when passing near an atomic nucleus as in order for energy and momentum to be conserved, the nucleus will experience some recoil. For particles their total energy is a sum of their rest energy and kinetic energy which means the incident photon must have at least enough energy to generate the electron-positron pair, where each of the pair has a rest mass of 511 keV giving a minimum photon energy threshold of 1.02 MeV. The cross-section for this interaction is proportional to the atomic number squared[68].

$$\sigma_{pp} \propto Z_A^2 \tag{2.87}$$

It is also possible for a photon to interact in the near vicinity of an atomic electron and generate an electron and positron. This process is termed triplet production, as the photon vanishes and its energy is transferred to the atomic electron and the electron-positron pair. The minimum photon energy for this process is higher at 2.04 MeV. The cross-section with a neutral atom for triplet production is proportional to the atomic number[68].

$$\sigma_{tp} \propto Z_A \tag{2.88}$$

Generally pair production dominates interactions compared to triplet production, thus at high energies the cross-section is approximately proportional to the square of the atomic number. The cross-section rises rapidly with energy after the threshold is exceeded. And then continues increasing at a slower rate beyond 10 MeV[68].

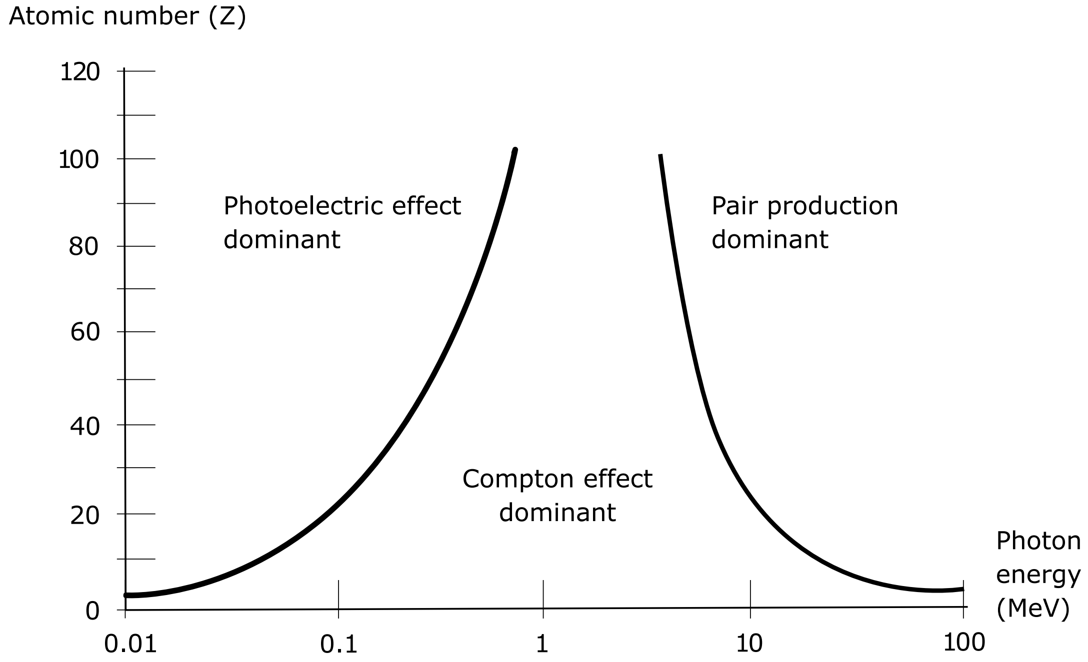

Figure 2.19: Shown is the photon energy and material atomic number (Z_A) dependence of the dominant interaction mode in photon-matter interactions. Low energy and high atomic number (Z_A) is dominated by the photo-electric effect. High energy and high atomic number are dominated by pair-production. And Compton scattering dominates for intermediary energies and low atomic number. Reproduced from Figure 1.8 in reference [73] with permission from IAEA and Dr. Podgorsak.

The relative contributions of each interaction type can be visualized by looking at the individual and total cross-sections for water (Figure 2.18)[70]. The curves highlight how Compton scattering dominates the relevant energy range and photoelectric and pair production dominate at very low and very high energies respectively. The energy at which Compton exceeds the photoelectric and the energy where pair production exceeds the Compton likelihood, can be plotted for various atomic numbers, to visualize regions of dominance across energy and atomic species (Figure 2.19)[68].

The total attenuation of a photon beam is described as a sum of all possible interactions[68].

$$\mu_{tot} = \rho\frac{N_A}{A}\left(\sigma_{pe} + \sigma_{inc} + \sigma_{pp} + \sigma_{tp} + O(\text{Rayleigh term})\right) \tag{2.89}$$

2.2.3 Dose Deposition

Critical to radiation physics as applied to treatment of cancer is the deposition of dose into a patient by the photon beam generated by the linac. A high energy photon beam will be attenuated through the patient as described by

$$\Phi(d) = \Phi(0)e^{-\mu_{tot}(d)d} \tag{2.90}$$

where $\Phi(d)$ is the photon beam energy fluence (J/cm^2) at depth d in the patient and μ_{tot} the total attenuation coefficient. As discussed, cross-sections and hence the total attenuation can depend on energy and will vary spatially within the patient. This means that Equation (2.90) is implicitly integrated across energy and μ is the path specific mean attenuation which will be dependent on position in the beam and depth in patient.

The energy fluence lost to the primary beam is scattered away or transferred to the medium. To determine the energy transferred we consider a $\mu_{tr} < \mu_{tot}$ that includes only the interactions that lead to an energy transfer to the medium, such as the energy transferred to an electron in Compton scattering. Combining the energy fluence, the energy transfer attenuation coefficient, and the density gives the kinetic energy released per unit mass or KERMA (K)[73].

$$K = \Phi(\frac{\mu_{tr}}{\rho}) \tag{2.91}$$

The unit for KERMA is the gray (Gy) which is joules of energy deposited per kg of material (J/kg).

Some of the energy transferred to the medium will not be deposited in the medium. For example as described in (Section 2.2.2.1 excited electrons will radiate some of their energy as bremsstrahlung. The amount radiated away is small as the efficiency in the water like tissue of a patient and for the energies of electrons set in motion by the photon beam is much smaller that that seen in a metal target. The attenuation term taking into account this small loss is $\mu_{en} = (1 - g)\mu_{tr}$ for some small value of g. The product of this energy absorbed coefficient, the energy fluence, and the density is the collisional KERMA (K_{col}).

$$K_{col} = \Phi(\frac{\mu_{en}}{\rho}) \tag{2.92}$$

The energy absorbed by the material is not deposited locally at the point of transfer. Depending on the energy transferred to atomic electrons, these electrons will travel and the energy will be deposited along their paths. Thus energy absorbed at some depth will through conservation of momentum be deposited some distance down stream. The energy deposited in the material locally per unit mass is the dose (D) in gray. Dose depends on collisional KERMA and the downstream travel of the absorbed energy.

At the entrance surface of a medium, collisional KERMA will be the highest as the photon beam will be unattenuated. The dose however is very small as most of the absorbed energy is in electrons moving downstream and slowly depositing the energy. At further depths, the dose approaches collisional KERMA as the amount of electron energy travelling from upstream to a point in the material reaches the amount of electron energy generated by the absorbed energy. Electronic equilibrium is defined as the condition when these two energies are equal. If there were no beam attenuation or divergence, the energy fluence and hence KERMA would be constant, so true electronic equilibrium would be maintained. However, since KERMA falls off, the dose exceeds KERMA beyond the point of equality as the local energy deposited depends on the higher collisional KERMA at a shallower depth.

$$D(d) = \beta K_{col}(d) : \beta < 1 \text{ for } d < d_{max},\ \beta > 1 \approx \text{constant for } d < d_{max} \tag{2.93}$$

The region before d_{max} is called the build-up region as dose is building up towards collisional KERMA. The value of β with depth in this region is not well described, but the dose rises sharply with depth and then its rise slows as D_{max} is approached. This can be seen in the percentage depth dose curve or PDD in Figure 2.20. It is convention to scale the maximum dose to 100% as absolute dose can be changed by the intensity of the initial energy fluence, but the relative shape will persist as long as the energy distribution of the energy fluence remains constant[73, 74].

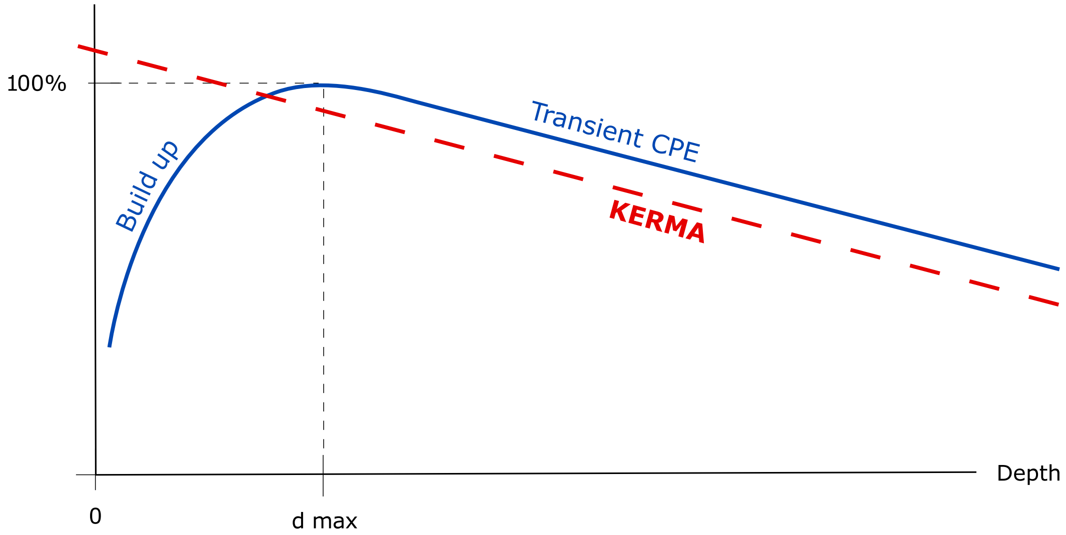

Figure 2.20: The percentage depth dose in water for a photon beam and its relationship to KERMA. KERMA falls off with depth right from the surface, as the water in the path of the beam is always attenuating the primary beam, thus reducing the amount of primary beam that can interact at deeper depths, thus reducing the amount of kinetic energy that can be released to the media. In contrast, prior to establishment of TCPE, in the build-up region the dose to water rises quickly from from a small amount at the surface (about 20% of maximum dose for 6 MV) to 100% at about d_{max} (i.e., for a 6MV beam d_{max} is 1.5 cm). Beyond d_{max}, the dose is proportional to KERMA and always larger as described by Equation (2.93). Pavel Barta ©. Used with permission.

Note also that the build-up region exists due to the non-zero but finite range of electrons excited by the incident photon beam. As the energy of the photon beam increases the electron range will increase, this means electrons will travel deeper (on average) before depositing all their energy locally. This leads to the depth of maximum dose increasing with higher mean photon energy.

The fall-off of the PDD with depth is a combination of attenuation, beam divergence, and scatter. The attenuation depends on the attenuation coefficient (Equation (2.90)) which is energy dependent. As the photon energy increases the attenuation coefficient becomes smaller, hence higher energy beams have a shallower fall off beyond d_{max} in addition to a deeper d_{max}. Beam divergence is a consquence of the beam originating from a very focused electron beam. The beam spreads out over a larger area as the square of the distance from the source. Divergence reduces the energy fluence as the same energy is spread over a larger cross-sectional area, so dose falls as the inverse square of the distance from the source. As the distance from the source to the surface of the medium (source-surface distance, SSD) increases, the difference between the inverse square factor at the surface and at a depth, d, becomes smaller

$$\frac{IS(d)}{IS(surface)} = \frac{(SSD)^2}{(SSD+d)^2}. \tag{2.94}$$

The divergence of the beam and the increasing beam size does increase the amount of scatter contributing to dose along the central axis. For very narrow beams, there is no fluence away from the central axis and so scatter only leads to decreased dose along the central axis (accounted for by the attenuation coefficient). However as the beam cross-section increases some of the energy absorbed away from the central axis will travel laterally and be deposited along the central axis contributing dose. Hence, in beams with a larger field size the dose fall off less rapidly with depth.

2.2.4 Dose Measurement

Calculating dose is quite challenging, requiring evaluation of cross-sections, calculating the mean transferred energy for each interaction, precise knowledge of the photon fluence, and integration over all energies. While simulation and dose calculation is important in clinical radiation therapy, there is no replacement for measurement.

Measurement of radiation dose is done with ion chambers. Typically, a gas filled cavity with a central anode and cathode walls forms the detection volume. Some voltage is applied across the chamber between the anode and cathode. Photons and electrons passing through the chamber will ionize the gas forming positively and negatively charged pairs. The positively and negatively charged ion pairs will be pulled towards the cathode and anode respectively. The flow of charges (mainly from the electrons due to their much lighter mass) forms a current from anode to cathode, which can be measured with a current meter. By calibrating to a known radiation source, the ion chamber can be used to measure dose in a wide range of circumstances[75].

2.2.5 Surface Dose and Skin Dose

A special consideration for the surface dose and the first 100 μm in medium is that a significant portion of the dose is from electrons generated outside the medium. Electrons generated in the linac head and in the air column, where the electron range is much longer, will strike the patient, contributing dose. Over 50% of the surface dose is from electrons generated in the air[76]. In the absence of these electrons, the dose to the surface would be much lower as only the backwards scattered electrons deposit energy in the most superficial layers[74].

The low surface dose and the build-up effect are important features in radiation therapy. When the clinical target is at depth, the low surface dose and build-up act to spare (reduce the dose to) the surface of the patient. The skin is a sensitive organ that is always irradiated during external beam radiation therapy, and radiation induced skin reactions are common. The skin consists of epidermal and dermal layers. The epidermis, the outermost skin layer, is at 70 μm depth and the dermis, the connective tissue and sensory nerve containing layer, is at 100 μm. The dose at a depth of 70 μm

is typically considered the skin dose. Higher energy beams yield more skin sparing (through lower dose to skin), thanks to the more penetrative photon beam, and the longer electron ranges. Reducing radiation dose is essential to reducing acute and long term skin reactions[77].

Acute skin reactions are those that appear within 3 months of exposure. There are well understood links between the dose to skin and the kinds of effects expected. As little as 2 Gy (total dose from all treatment fractions) leads to short term reddening of the skin (erythema), similar to a sunburn[77]. At 8 Gy, the skin experiences further erythema and potential loss of hair (epilation). At 16 Gy the erythema is pronounced and the skin can become darkened, termed hyper pigmentation. At 23 Gy, the skin begins to peel as the skin cells are heavily damaged and die off. At 35 Gy the skin is heavily compromised and begins to leak, the skin no longer acts as the protective barrier it should, termed moist desquamation. At more than 40 Gy, the skin will break and significant damage and cell death occurs throughout the affected area[77].

In addition to acute skin reactions, which tend to recover over time as the skin cells regenerate, radiation damage to skin can also appear later and be chronic. While not linked directly to specific dose thresholds, the higher the dose to the skin during treatment the more likely and the worse the late effects[77]. These late effects are progressive and irreversible, and result in irreparable damage to the skin as the area loses the ability to regenerate.

In some cases the target of a treatment will be near the surface at a depth less than d_{max} of the chosen beam. In this case, to avoid under dosing the target, it may be necessary to place additional material on the surface of the patient to provide additional build-up, shifting the effective depth of the target according to the amount of material added. The additional material is clinically called bolus. This leads to additional skin dose, but is warranted when it is needed to ensure coverage of the target.

Chapter 3

Impact of a Parallel Magnetic Field on Radiation Dose Beneath Thin Copper and Aluminum Foils[1]

3.1 Introduction

Magnetic resonance image guided radiotherapy (MRIgRT) has the potential to deliver state-of-the-art radiation therapy concurrently with soft-tissue imaging[12–16]. Because radio frequency (RF) coils provide maximal signal to noise ratio (SNR) in MRI when placed closest to the imaged region, these coils may need to be placed in the path of radiation beam(s) treating the same region. While it is possible to use RF coils placed far enough away to avoid intersecting the beam path or to treat only from angles that do not irradiate the coil[36, 37], image SNR or treatment plan quality, respectively, may suffer. For the RF coil designs that do intersect the radiation beam, it is important to understand the dosimetric consequences of materials intersecting the beam in a magnetic field.

While previous studies have shown minimal impact of RF coils in the beam on the target volume dose[32, 33], only one study has investigated the impact on the surface dose[33]. A stack of materials simulating an RF coil placed in the beam, in

---

[1] This chapter has been previously published as: Barta, R., Ghila, A., Rathee, S., Fallone, B. G., & De Zanche, N. (2020). Impact of a Parallel Magnetic Field on Radiation Dose Beneath Thin Copper and Aluminum Foils. Biomedical Physics & Engineering Express, 6, 037002. http://iopscience.iop.org/10.1088/2057-1976/ab7cf2

contact with a phantom surface, increases the surface dose to $>$75% of maximum dose ($\mathrm{D_{max}}$)[33]. This example coil consisted of a polycarbonate base (1.5 mm), copper tape conductor (0.08 mm), and PTFE (Teflon®, 0.9 mm) cover. The surface dose increase was measured with the magnetic field both parallel and perpendicular to the beam, as well as without field. The authors also found a surface dose increase to 45% $\mathrm{D_{max}}$ (48% $\mathrm{D_{max}}$ in a parallel magnetic field from a 0.22 T magnet) for a 0.1 mm copper plate alone[33].

The surface dose increases due to the low energy secondary electrons, produced by photons interacting with coil materials, depositing their energy in the superficial layers of a phantom or patient below (bolusing effect, Section 2.2.5). In this reference[33], and a follow up study comparing measurements to Monte Carlo simulations[78], Ghila et al. also found that the surface dose increased in the presence of a parallel magnetic field even when nothing was obstructing the beam path. The surface dose was 20% $\mathrm{D_{max}}$ without field, and 30% $\mathrm{D_{max}}$ in the presence of the field[33, 78]. This effect is caused by contaminant electrons (produced in the linac head and irradiated air column) being trapped and guided by Lorentz forces due to the magnetic field[33, 78]. Similar effects have been simulated and measured in other studies of MRIgRT systems[79, 80]. Note that, for such parallel systems, the strength of the field at the surface is not as important as the strength and shape of the fringe field near the linac head and in the air column. The exact shape of the field determines where on the surface the contaminant electrons contribute dose.

The interest in surface dose is motivated by skin reactions that occur in radiation therapy. Even in traditional fractionated treatments, low levels of acute skin reactions are common with the skin receiving a fractionated dose of 2-8 Gy[77]. For every doubling of absorbed skin dose, the degree of acute skin damage increases by one step: from discoloration, to erythema, to desquamation, up to necrosis at 40 Gy fractionated. Additionally, increased dose to skin raises the risk of long-term effects of radiation dose and their severity[77].

Large increases in surface dose due to in-beam RF coils can, however, be reduced. The predominantly Compton interactions in the therapeutic photon energy range depend on electron density (e^-/cm^3)[81]. Since electron mass density (e^-/g) varies slowly with atomic number, the number of Compton interactions depends on the amount of material (thickness) and its density. Thin ($\ll$0.1 mm) and/or lower density conductors in RF coils thus may allow in-beam coils to be placed directly on the patient surface without a large increase in skin dose[33]. Lightweight RF coils that use conductive inks[82, 83], thinner conductors[84], and minimal enclosures are already being designed for a variety of purposes. Conductors made of aluminum instead of copper have also been considered because of the lower density[84, 85].

This work fills a gap in the literature by presenting surface dose measurements, with and without a parallel magnetic field, below various thicknesses (9–127 μmm) of copper and aluminum, and insulating materials that could be used as enclosures for in-beam RF coils.

3.2 Materials and Methods

The surface dose below square (10 × 10 cm^2) copper and aluminum foils of thicknesses ranging from 9 to 127 μm was measured using a PTW Markus parallel plate ion chamber (PTW, Freiburg, Germany). The surface dose was also measured below a polyimide film (17 μm thick, Kapton®, DuPont, Wilmington, DE, USA) and a polyester film (127 μm thick, HP LaserJet transparency, Hewlett-Packard Company, Palo Alto, CA, USA). Polyimide is a common substrate for flexible printed circuit boards (PCBs). The polyester film is a potential lightweight enclosure material for flexible RF coils. For comparison, the surface dose below a hospital gown was also measured.

Each sheet was positioned in contact with the top surface of a solid polystyrene phantom which simulated tissue and provided backscatter. The parallel-plate ion chamber was set into the phantom top surface [33] with its effective point of measurement being just below the entrance window (0.03 mm polyethylene). The sheets were irradiated with a square 8.5 × 8.5 cm^2 (source to phantom surface distance or SSD = 170 cm) 6 MV beam from a Varian Silhouette linac (Varian Medical Systems, Palo Alto, CA) with and without the presence of a parallel magnetic field. Dual solenoid electromagnets (model 3472-70, GMW Associates, San Carlos, CA), placed on a wooden stage on the floor (Figure 3.2), generated a 0.22 tesla (T) field at the center of their bore decreasing to 0.6 mT at the linac's exit window (Figure 3.3)[33, 78]. The polystyrene phantom was positioned inside the bore of the electromagnets such that the top surface of the phantom coincided with the top of the solenoids (Figure 3.1).

Surface dose was determined as the ratio of ionization in the ion chamber at the surface to the maximum ionization (D_{max}) in the phantom. Readings were taken at 1.4 cm, 1.5 cm and 1.6 cm depths, below stacks of polystyrene sheets, to sample the depths where maximum ionization (D_{max}) is expected. D_{max} was measured with and without a magnetic field. The ratio of ionizations is reported as a percent of D_{max} (% D_{max}). This chamber and set-up has been validated in previous studies[33, 78].

Measurements were performed over several days and repeated measurements were averaged. For thin foils (thickness $\leq 25\ \mu$m) linear regression was used to fit the surface dose increase for copper and aluminum with and without a field. The p-value was used to evaluate the goodness of the fit[86]. P-value is based on the χ-square test and gives the probability that a data set with a worse misfit (higher χ-square) would be obtained assuming the fit is correct. The 95% confidence interval was used as the error in the slope.

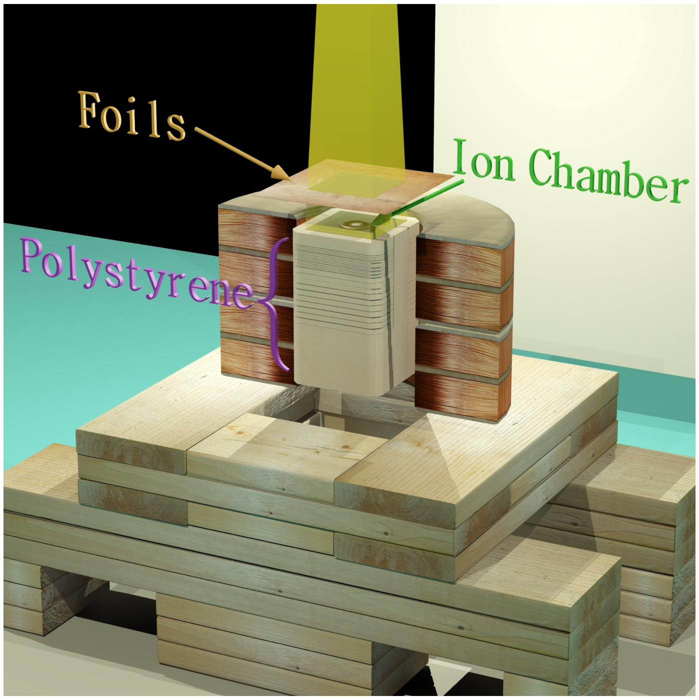

Figure 3.1: Surface dose was measured below copper and aluminum foils of various thicknesses. The foils were placed in the beam on top of the polystyrene phantom surface with an inset parallel plate ion chamber. Foils were in direct contact with the phantom surface (gap in image is introduced to show the ion chamber). The phantom was inside the bore of dual solenoid electromagnets positioned on top of a wooden support structure.

Figure 3.2: A photograph of the dual solenoid magnet positioned at the center of the light field at an SSD of 170 cm to the top of the magnets.

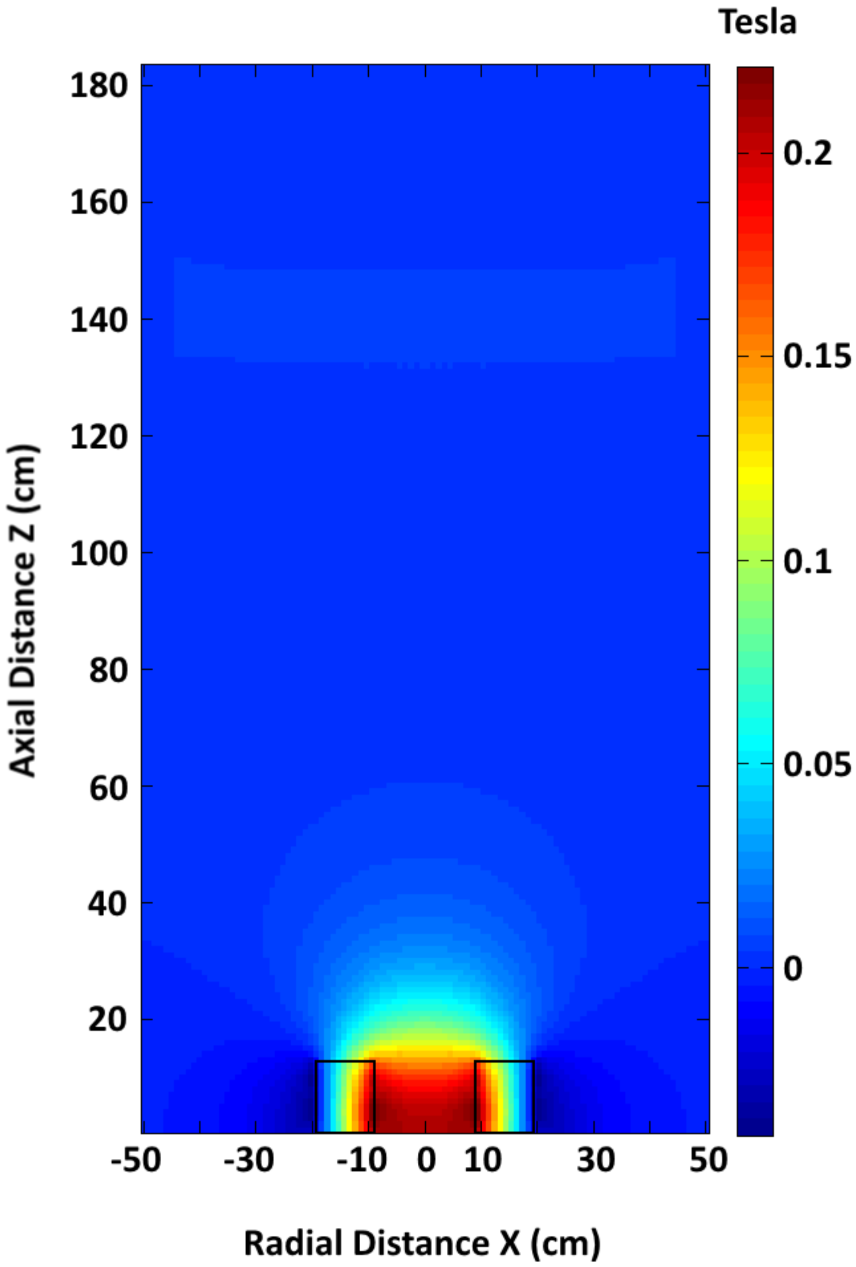

Figure 3.3: Magnitude of the magnetic field generated by the dual solenoid magnet (black rectangles mark its cross-section). The strength of the field decreases rapidly with distance from the magnet. Near the linac head (its position is marked by a faint rectangle) is 0.64 mT, many times weaker than the 0.2 T at the magnet center. Courtesy of Andrei Ghila. Used with permission.

3.3 Results

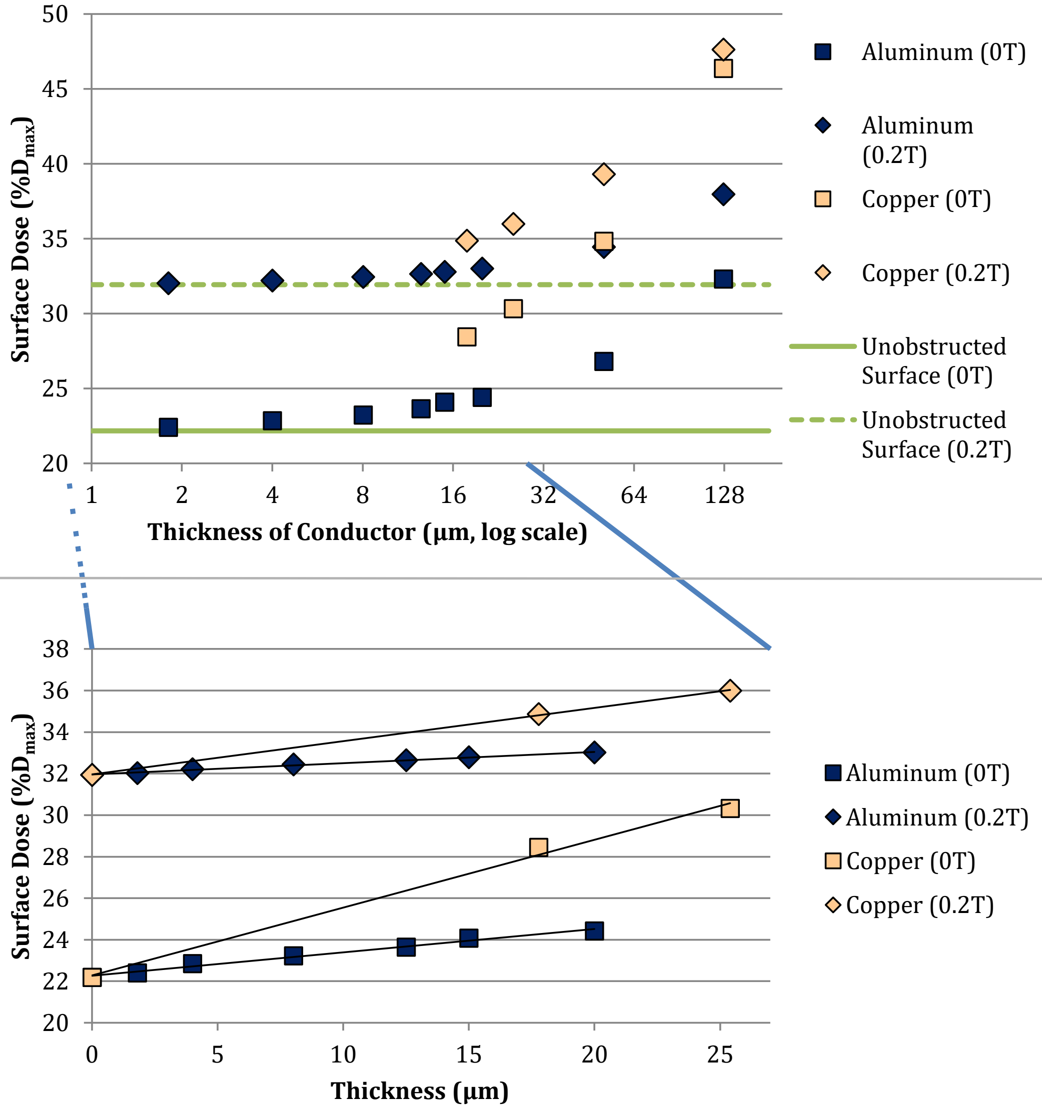

Figure 3.4: (Top) Surface dose measured below copper and aluminum sheets of various thicknesses (logarithmic scale). The unobstructed surface doses were 22%$D_{\max}$(solid horizontal line) and 32%$D_{\max}$(dashed line) without and with a parallel magnetic field (0.22 T magnet) respectively. Uncertainty in each data point is less than 1% (.2%$D_{\max}$). (Bottom) The linear region (0 to 25 μm) is expanded and shown on a linear scale and with linear fits. The slopes are 0.116 $\%D_{\max}\mu m^{-1}$ (no field, marked 0T) and 0.06 $\%D_{\max}\mu m^{-1}$ (with field, marked 0.2T) for aluminum, and 0.339 $\%D_{\max}\mu m^{-1}$ (no field) and 0.16 $\%D_{\max}\mu m^{-1}$ (with field) for copper.

The average surface doses for an unobstructed beam were 22.2 ± 0.1 % and 31.9 ± 0.2 % of Dmax with no field and with the magnetic field respectively.

The measured surface dose increases due to copper and aluminum are shown in Figure 3.4, showing an approximately linear relationship for thicknesses $\leq 25\mu m$. Surface dose increases by 0.339 ± 0.008 $\%D_{\text{max}}\mu m^{-1}$ for copper ($\chi^2 = 15.6, p = 0.0004$) and 0.116 ± 0.006 $\%D_{\text{max}}\mu m^{-1}$ for aluminum ($\chi^2 = 8.99, p = 0.174$) with no field; and by 0.16 ± 0.01 $\%D_{\text{max}}\mu m^{-1}$ for copper ($\chi^2 = 0.132, p = 0.936$) and 0.06 ± 0.01 $\%D_{\text{max}}\mu m^{-1}$ for aluminum ($\chi^2 = 0.165, p = 0.999$) with field. Slopes are obtained by linear regression with the open-field dose being a fixed zero-intercept. With the exception of the no field copper data, the p-values suggest that the datasets match a linear trend reasonably well[86]. For copper (no field) the extremely small p-value (4×10^{-4}) indicates a poor model fit given the small (1%) uncertainty of the measurements. This may be due to the limited number of points for thin copper foils, or that the linearity approximation breaks down in this case.

Table 3.1: Surface dose for support and enclosure materials positioned in the beam.

Material	**Surface Dose with No Field ($\%D_{\text{max}}$)**	**Surface Dose with Field ($\%D_{\text{max}}$)**
Open Field	22.2	31.9
Hospital Gown	28.3	36.0
Polyimide (17 μm)	23.7	32.7
Polyester (127 μm)	28.5	35.9

Measurements of surface dose below a hospital gown, polyimide (17 μm), polyester (127 μm) are listed in Table 3.1. The surface dose increase due to the polyester film is comparable to the increase caused by a hospital gown. The 17 μm polyimide had a very small impact on the surface dose similar to that of 15 μm aluminum; with either one of these, the surface dose (with field) is within 1 $\%D_{\text{max}}$of the surface dose (with field) of an unobstructed beam.

3.4 Discussion

The magnitude of the increase in the surface dose, for an unobstructed beam, due to the magnetic field (from $22.18\%D_{\max}$ to $31.9\%D_{\max}$) is dependent on the specific magnetic field pattern[17] between the linac head and the phantom surface. As other studies have found[17, 33, 79, 80] the parallel magnetic field in general leads to surface dose increases due to trapping of contaminant electrons.

Adding coil conductors ($\leq 25\ \mu$m) in the beam causes the surface dose to increase proportionally to the thickness of copper and aluminum as confirmed by the goodness of fit. For thicker conductors the proportionality breaks down because they partially self-shield, with downstream segments of the foil absorbing some of the electrons produced upstream in the same foil.

Interestingly, the slopes of the fits in a magnetic field are lower than those without a magnetic field. This is most likely due to the metal sheets shielding the surface from contaminant electrons captured by the magnetic field. A thicker sheet, while increasing the dose due to a greater build-up (bolusing effect), will also better shield the surface from upstream contaminant electrons captured by the parallel magnetic field. This means the effect of material in the beam is reduced in the presence of the magnetic field compared to the open field dose. The ratio of slopes between copper and aluminum (2.9 ± 0.2 with no field, 2.9 ± 0.7 with field) is consistent with the ratio predicted by the relative electron density of the two metals (3.1)[87].

Measuring the surface dose below a hospital gown allows us to compare the effect of the metal foils to a material that is used clinically and typically considered negligible. Copper $\leq 25\ \mu$m, and aluminum $\leq 50\ \mu$m thick increase the surface dose less than a hospital gown does. The conductors of RF coils can thus be made to have a negligible effect on the surface dose.

Additionally, the enclosures for RF coils need not increase the surface dose to 83 %

of Dmax as traditional MRI coil enclosures do[33]. Thin (17 μm) polyimide increases surface dose by little over 1% (compared to an unobstructed beam). If enclosing polyimide layers are considered insufficient, a layer of polyester (127 μm), while increasing the dose more than a hospital gown, is still dramatically less impactful on the surface dose than traditional housings (4 - 6.3%$D_{\max}$increase vs. 60%$D_{\max}$increase)[33].

Surface dose increases due to material in the beam are consistent with previous results[33]. These measurements are specific to the field shape and strength used. The surface dose increases will differ for other magnetic fields and must be measured to verify the trends described. Specifically, depending on the magnetic field strength and shape, the contaminant electron spectrum at the surface of the patient will change[17]. As an extreme example, in perpendicular field almost all the contaminant electrons as are swept away rather than trapped by the magnetic field. However, regardless of the electron spectrum, the increased surface dose due to the bolusing effect will still be present for surface RF coils regardless of magnetic field configuration or strength.

The measurements in this study were performed on foils that were slightly larger than the radiation field size to allow for reliable comparisons between thicknesses and materials. In reality, surface RF coils are constructed of narrow strips of foil and thus these surface dose measurements represent upper bounds. The introduction of air gaps that would be present in rigid volume coils will further reduce the surface dose increase in perpendicular magnetic fields, where a large enough gap can eliminate the bolusing effect completely[31, 33]. In parallel magnetic fields, gap leads to no surface dose increase for foils, but larger gaps still reduce the peak surface dose increase due to strip or rod of material in the beam[33]. This data also suggests that evaluating the surface dose impact should be an integral part of the design procedure for RF coils used in the radiation beam of MRIgRT systems.

Surface dose in the presence of a magnetic field is highly dependent on the strength and orientation of the magnetic field lines and their proximity to the linac head. Compared to the 0.5 T parallel field lines in the 120 cm SAD Alberta linac-MR, our experiments used a 0.22 T magnet at 170 cm SSD, whose field lines are not parallel outside of the magnet. As such, compared to our experiments, the Alberta linac-MR radiation field contains many more low-energy contaminant electrons and a larger surface dose: 46%$D_{\mathrm{max}}$to 75%D_{max}without and with a magnetic field respectively[88]. Due to this larger electron contamination, we anticipate that in the Alberta linac-MR thin metal sheets will increase the surface dose beyond those values reported in this work. The measurements and simulations needed to determine the extent of enhanced surface dose in the Alberta linac-MR are beyond the scope of this work.

3.5 Conclusions

As advancements are made in MRIgRT, RF coils will continue to be critical components in effective treatments and imaging. It is impractical to expect that every MRIgRT treatment plan will avoid beam(s) passing through the RF-coil. The introduction of materials in the path of the radiation beam leads to measurable increases in patient surface dose that can have serious consequences. Surface coils will increase entrance surface dose regardless of magnetic field strength or configuration (transverse or parallel) due to the bolusing effect. This study is an investigation of different thicknesses of copper and aluminum which could serve as alternative conductors in RF-coils. RF-coils built with thinner and aluminum conductors may yield lower surface dose if trends shown here extend to MRIgRT systems. Similarly, the enclosure materials tested (polymide and polyester) interact with the beam on the same order or less than a hospital gown. If these are used in RF-coils for MRIgRT systems, the surface dose impact could be reduced.

For thin materials the surface dose increase is found to be proportional to thickness and electron density of the material. Therefore, using thin (≤ 25 μm) and/or lower density materials (aluminum rather than copper), may have applications in RF-coils that are placed on the surface and in the path of the radiation beam.

Chapter 4

How Thin Can You Go? Performance of Thin and Non-copper RF Coil Conductors[1]

4.1 Introduction

Several emerging technologies are expanding the range of conductors available for RF coils beyond traditional materials. In conventional RF coil construction, thick copper conductors (including solid or hollow bars or tubes, as well as standard printed circuit boards (PCB)) ensure the coil has the lowest possible losses for a given design due to copper's excellent electrical conductivity ($5.9 \times 10^8 Sm^{-1}$) [89]. Resistive losses in the conductor lead to lower SNR [90] and therefore traditional coil design has naturally placed an emphasis on minimizing losses. Use of conductors several times thicker than the skin depth is necessary to avoid SNR losses due to sub-optimal current cross-section [91].

Recent RF coil design paradigms, however, relax this convention to take advantage of the benefits of thin or alternate conductor coils. For example, lightweight (minimal enclosure), flexible coils are more comfortable [82] and can provide better SNR than rigid setups due to closer proximity to the imaging region. Examples include screen-printing to create RF coils that are incorporated into infant blankets [82], as well

---

[1] This chapter has been previously published as: Barta, R., Volotovskyy, V., Wachowicz, K., Fallone, B. G., & De Zanche, N. (2020). How thin can you go? Performance of thin copper and aluminum RF coil conductors. Magnetic Resonance in Medicine. https://doi.org/10.1002/mrm.28540

as flexible, meandering wires that allow the coil conductor's path to change [92, 93]. Conductive textiles can be stretched up to a 100 times their size [94], and a flexible coil made from a conductive elastomer based on silver microparticles achieves an SNR just 14% lower than a reference copper coil [95]. Liquid metal [96, 97] and braided conductors [98] also allow for stretchable coils that closely fit moving and flexing body parts [96, 98]. Further alternate conductors include aluminum (conductivity $3.54 \times 10^8 Sm^{-1}$), which has applications in multi-modality systems such as x-ray MRI [85], PET-MRI [99], and linac-MR systems [12, 100], where interactions with ionizing radiation must be minimized. In x-ray MRI [85], aluminum coils significantly reduce artifacts in the x-ray image compared to the copper coils. In PET-MRI [99], attenuation of the photons through aluminum is reduced compared to copper, but the difference is inconsequential because the required correction is equally effective for copper or aluminum conductors. In linac-MR systems [12, 100], the use of aluminum conductor of the same thickness as copper leads to interactions with the beam that are up to three times smaller.

Thinner conductors can also allow for reduced interactions with radiation [100], as well as allowing form-fitting coils made of flexible PCB (which use thinner copper than the up to 70 μm typically used in rigid PCBs). Quantifying the increased resistance expected due to using a thinner conductor is, however, not simple analytically. For thin rectangular traces both the classical and lateral skin effects determine the effective resistance of the coil; their contributions can only be approximated or simulated and in practice must be measured [101, 102].

Consequently, in this study we compare the image SNR of coils that span a range of conductor losses measured on the bench. This work demonstrates that despite having higher resistance compared to standard thick copper, coils made of thinner or alternate conductors achieve SNRs that may exceed intuitive expectations. We believe this to be the first such exploration of a wide range of thicknesses (using two materials) with other variables carefully controlled.

4.2 Methods

4.2.1 Coil Construction and Bench Measurements

Surface coils for a 0.48 T (20.56 MHz) system were constructed with different thicknesses of thin aluminum foil (9 μm, 13 μm, 20 μm, and 127 μm). The 9 and 13 μm thick aluminum foils had a polyester laminate backing ($\sim 12 \mu m$ thick). Preliminary tests with small pieces of thinner aluminum (4 and 8 μm) without the backing material were challenging to work with, inconsistent and unreliable because they often had microscopic tears that impeded RF current flow. Thus, the resistance was higher than expected with these thin materials and they were not considered further. For comparison, coils were also constructed from thin copper (17 μm and 35 μm) with polyimide (Kapton®) backing ($\sim$ 17 μm), self-adhesive copper tape (32 μm), and copper foil (127 μm). A much thicker copper coil was made of 600 μm copper bars to demonstrate bulky conductors. At this frequency the skin depths for copper and aluminum are 14.4 μm and 18.1 μm, respectively.

All coils consisted of a square 15×15 cm^2 loop of 6-mm-wide traces with 12.5 cm long leads that were connected to a matching network (Figure 4.1). The long leads were used to create a coil that could be struck by a radiation treatment beam [100], while matching network components remained away from direct radiation. Total length of the trace was approximately $\lambda/18$ at 20.56 MHz which satisfies the maximum length criterion [103] without requiring additional capacitive breaks.

All coils (including 9 and 13 μm thick aluminum foils with polyester backing) used thin acetate projector film for backing and structural support. The traces (6 mm wide) were cut manually from the copper and aluminum foils (including any backing) using a sharp blade, and fastened to the projector film using double-sided tape (3M 667-ESF, Saint Paul, MN, USA). For the 32 μm copper coil, 6-mm-wide copper tape (Venture Tape Corp. No. 1725, Rockland, MA, USA) was pressed onto the projector film in the same shape. Joints in the corners were soldered to create a continuous

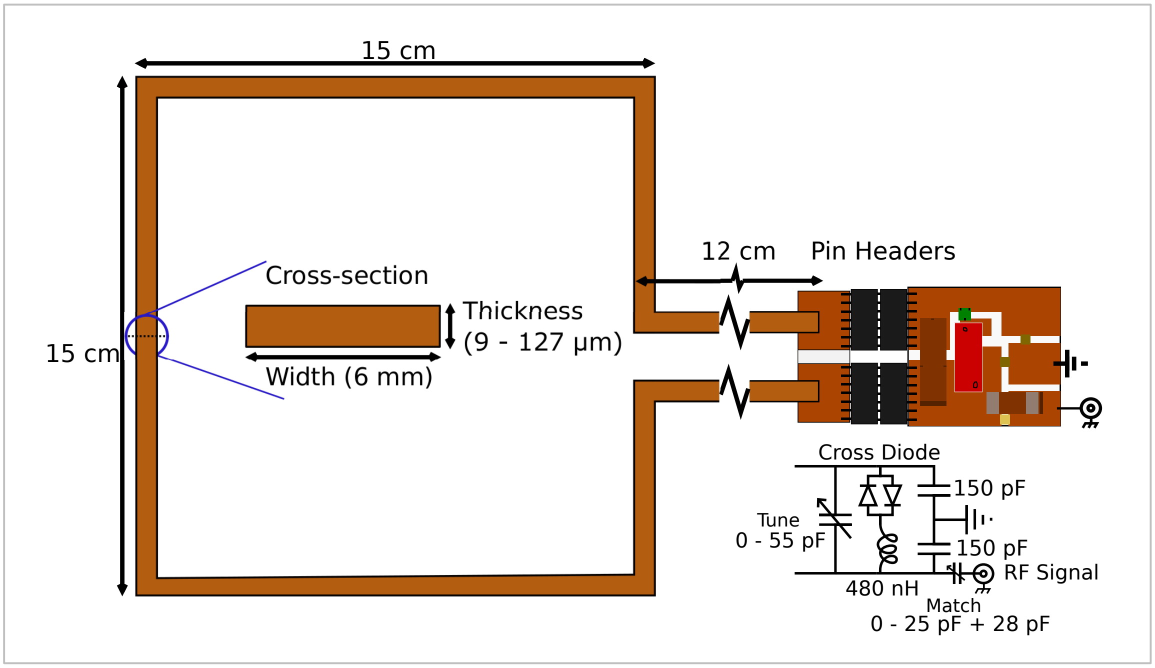

Figure 4.1: Coil schematic showing the dimensions (15 × 15 cm^2) of the conducting loop, as well as the layout of the tuning and matching circuits on the PCB and corresponding circuit diagram.

trace. The 600 μm bars were sheared from copper plate into 6 mm wide strips and then soldered into the required shape.

To ensure a stable electrical connection (especially for the aluminum coils that cannot be soldered) the ends of the leads were clamped between two pieces of FR4 PCB using non-magnetic rivets. Two sets of seven-pin headers were soldered to the PCB enabling the coils to be connected to tuning and matching capacitors mounted on a separate PCB. The 600 μm copper coil was soldered to the PCB rather than riveted.

Each coil was made resonant near 20.56 MHz (Larmor frequency at 0.48 T) to measure quality factor (Q) and total inductance (L) by mating its pin headers to a temporary PCB with female headers connected to two capacitors in parallel (68 pF ±5% and 47 pF ±5%). The Q was determined as the ratio of the resonance frequency and the 3 dB bandwidth from the transmission spectrum obtained between two small (∼ 1 cm ⌀) pick-up loops positioned at the corners of the square coils. Inductance

(L) of each coil was determined from the measured resonant frequency (ν_0) and the known fixed capacitance (C = 115 pF, two Voltronics 11 series capacitors in parallel, 68 pF ±5% and 47 pF ±5%).

Measurements were conducted with a ZVL3 Vector Network Analyzer (VNA) (Rohde & Schwarz, Munich, Germany). The quality factor was measured both unloaded, Qu (coils supported by foam), and loaded, Ql, by a head-sized, cylindrical aqueous phantom (19 cm $\oslash$, 15 cm high, 55 mM NaCl and 5 mM $NiCl_2$; ASG Superconductors, Genova, Italy). The unloaded Q was used to determine the resistive loss in each coil (r_C). Achievable SNR of a coil, relative to its intrinsic SNR (iSNR), is related to its efficiency ($\eta \in [0, 1]$) by [53]

$$SNR = \sqrt{\eta} * iSNR. \tag{4.1}$$

Efficiency depends on loss contributions from the sample (r_S) and coil (r_C). There are additional losses introduced due to the capacitors, soldering, and radiative losses, but these losses cannot be readily separated from the overall losses without modelling [101] hence

$$\eta = 1 - \frac{r_C}{r_C + r_S}. \tag{4.2}$$

If $\eta < \frac{1}{2}$ then coil losses are dominant, while if $\eta > \frac{1}{2}$ the sample losses are dominant. Since all coils have the same geometry, except for conductor material and thickness, the intrinsic SNR is expected to be equal (i.e., r_S is the same for all coils).

A symmetric matching network (Figure 4.1, right) was built on a small PCB and connected to each coil through the headers. Tuning the coils to 20.56 MHz was achieved using a variable capacitor (Voltronics AJ55HV, 0–55 pF) and symmetrically-connected fixed capacitors (Voltronics 11 series, 150 pF ±5%). The coils were matched by adjusting a variable capacitor (Voltronics AJ25HV, 0–25 pF) connected in parallel with fixed capacitance (two Voltronics 11 series 56 pF ±5% connected in series) by minimizing the return loss ($|S_{11}|$) at the resonance frequency measured with the VNA. To detune the coils during the transmission pulse of the imaging sequence, a passive crossed-diode (BAV 99) trap with a hand-wound inductor ($\sim 480nH$) was connected in parallel with the tuning capacitors. The coils were tuned and matched in the loaded condition.

4.2.2 Image SNR Measurement

The constructed coils were tested in the Alberta 0.5 T linac-MR system [12, 23]. This system is a combination of a modified clinical 0.48 T scanner with an integrated transmit volume coil (20.56 MHz ASG Superconductors) and a clinical linear accelerator. The parallel arrangement allows for real-time imaging while minimizing the effect of the Lorentz force on radiation dose distributions [12]. For each coil, a single, central 10 mm thick slice of the cylindrical phantom was imaged (Figure 4.2) with a gradient-echo imaging sequence (field of view = $40 \times 40cm^2$, TE = 12 ms, TR = 330 ms) to measure SNR variation with depth. A noise-only image corresponding to each signal image was acquired by repeating the same sequence without the excitation pulse. Each signal and noise image pair was acquired three times without re-positioning. Identical positioning of the phantom and all receive coils was assisted by markings on the table and phantom. Furthermore, transmit and receive RF amplifier gain settings were kept consistent across all measurements. This was achieved by controlling these parameters within the TNMR spectrometer software (TECMAG, Houston, TX, USA) of the system. Raw k-space data from the TNMR software was fast Fourier transformed in MATLAB (MathWorks, Natick, MA, USA).

The SNR profile as a function of depth from the surface of the phantom was determined to compare image quality across a large portion of the phantom. Stepping pixel by pixel along the depth axis of the phantom, at each depth the pixel values for the central 16 mm of the phantom were averaged to determine a mean signal value for that depth. The noise magnitude for each profile was determined by taking the

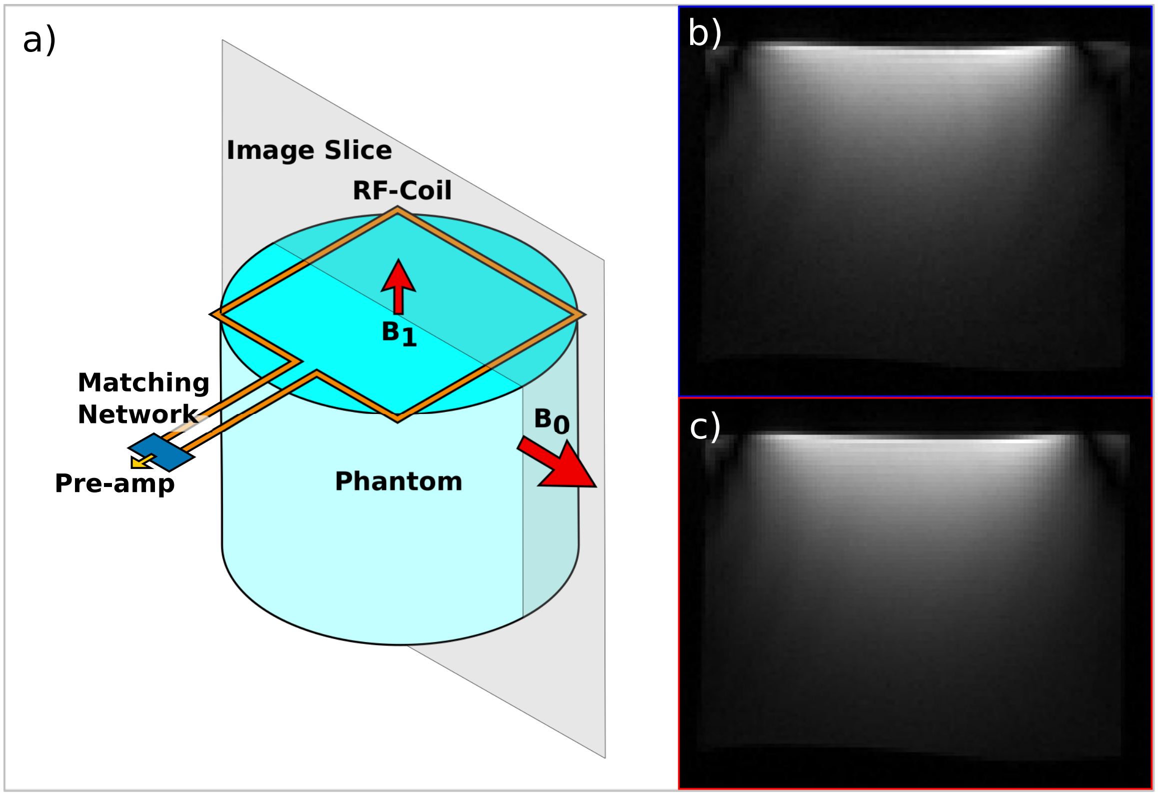

Figure 4.2: Experimental setup used for acquisition of phantom images in the linac-MR (2a, left) as well as sample images for the 9 μm aluminum (2b, top right) and 127 μm copper coils (2c, bottom right).

standard deviation of the corresponding noise-only image. The ratio of the signal values at each depth and the noise for that image gave an SNR profile for each signal and noise image pair. The SNR profiles for the three image pairs for each coil were averaged to give a single profile for comparison to those of the other coils.

As the standard for comparison of SNR between coils, locally weighted smoothing was applied to the SNR profile of the 127 μm copper coil using the smooth function in MATLAB (local regression, 2nd degree polynomial, based on nearest 10 points). Each coil profile was fitted to this standard curve by multiplication with a scaling constant obtained using least squares (LSQCURVEFIT, MATLAB). The scaling constant corresponds to the relative SNR which gives the minimum least squared error between the scaled standard and the data. The goodness of the fit was analyzed using χ^2 and p-values (χ-square test) [86]. Here the P-value is the chance that, assuming the fit is correct, a data set could be obtained and give a higher χ-square. Extremely low p-values ($\ll 0.01$) signify poor fits. A p-value very close to 1 (>0.99) suggests overfitting, or overestimated data errors. The solution covariance was used to determine the 95% confidence range which was used as the error in the relative SNR [86].

The relationship between the relative coil SNR as determined above, and the coil efficiency, as determined previously through bench measurements, was used to obtain an intrinsic SNR for this coil setup by fitting the SNR and root of efficiency data to Equation (4.2)

4.3 Results

4.3.1 Coil Efficiency

The coil efficiency as a function of conductor thickness is tabulated for aluminum and copper in Table 4.1. As can be expected [91], the quality of the coils (Table 4.1) improves with increased conductor thickness, and aluminum coils have a lower efficiency than copper coils for a similar thickness. These bench measurements predict that even the thinnest (9 μm) aluminum conductor coil will achieve an SNR that is almost 75% of that of the 127 μm copper foil coil despite a three times higher coil resistance.

4.3.2 Image SNR

Figure 4.2 b and c show example images acquired with the 9 μm thick aluminum coil and the 127 μm thick copper coil. Images acquired using each coil look qualitatively similar despite the wide variation in coil materials, thereby showing that other variables such as geometry were tightly controlled. In Figure 4.3, the SNR profiles for each coil (averaged from three measurements) are shown to highlight the SNR differences between different thicknesses and materials. Figure 4.4 shows the SNR of each coil (squares and diamonds) relative to that of the 127 μm copper coil as a function

Aluminum	Resistance(Ω)	Unloaded Q	Loaded Q	Ratio	Efficiency
$127\mu m$	$.286 \pm .009$	239 ± 8	97 ± 2	2.5 ± 0.1	0.59 ± 0.02
$20\mu m$	$.462 \pm .007$	149 ± 1	80.0 ± 0.5	1.85 ± 0.02	0.461 ± 0.006
$13\mu m$	$.570 \pm .009$	114 ± 1	64 ± 2	1.77 ± 0.05	0.44 ± 0.02
$9\mu m$	$.74 \pm .01$	89 ± 1	59 ± 2	1.5 ± 0.2	0.34 ± 0.07
Copper	Resistance(Ω)	Unloaded	Loaded	Ratio	Efficiency
$600\mu m$	$.172 \pm .003$	390 ± 5	104 ± 2	3.76 ± 0.08	0.734 ± 0.006
$127\mu m$	$.24 \pm .01$	290 ± 5	104 ± 2	2.8 ± 0.1	0.64 ± 0.02
$35\mu m$	$.30 \pm .02$	230 ± 10	100 ± 10	2.3 ± 0.3	0.56 ± 0.05
$32\mu m$	$.29 \pm .02$	230 ± 10	99 ± 9	2.4 ± 0.3	0.58 ± 0.05
$17\mu m$	$.33 \pm .01$	205 ± 8	90.6 ± 0.5	2.3 ± 0.1	0.56 ± 0.02

Table 4.1: Bench Measured Coil Specifications. Values are either directly measured (Qs) or calculated from measured data (other columns). Uncertainty is based on variance across multiple measurements and accurate propagation of error for calculated values.

of conductor thickness. The 95% confidence interval for the fit values is around 2% making the error bars too small to visualize. P-values are between 0.4 and 0.5 which confirms fits and statistical assumptions are reasonable [86].

The general trend in SNR as a function of thickness and material is similar to the trend predicted by differences in coil resistance and efficiency. Indeed, plotting the image SNR and bench measured efficiency (Figure 4.5) shows qualitative agreement.

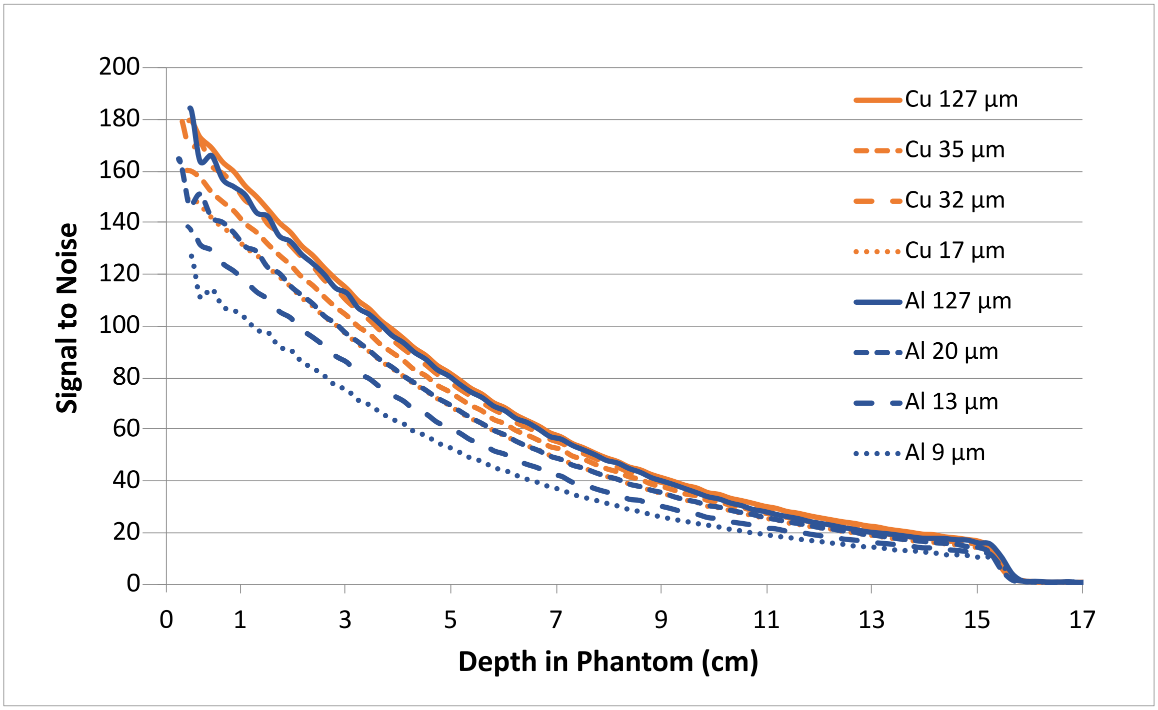

Figure 4.3: The averaged SNR image profiles for each RF coil. Data for the 600 μm thick copper coil is omitted as it was acquired with a different scaling.

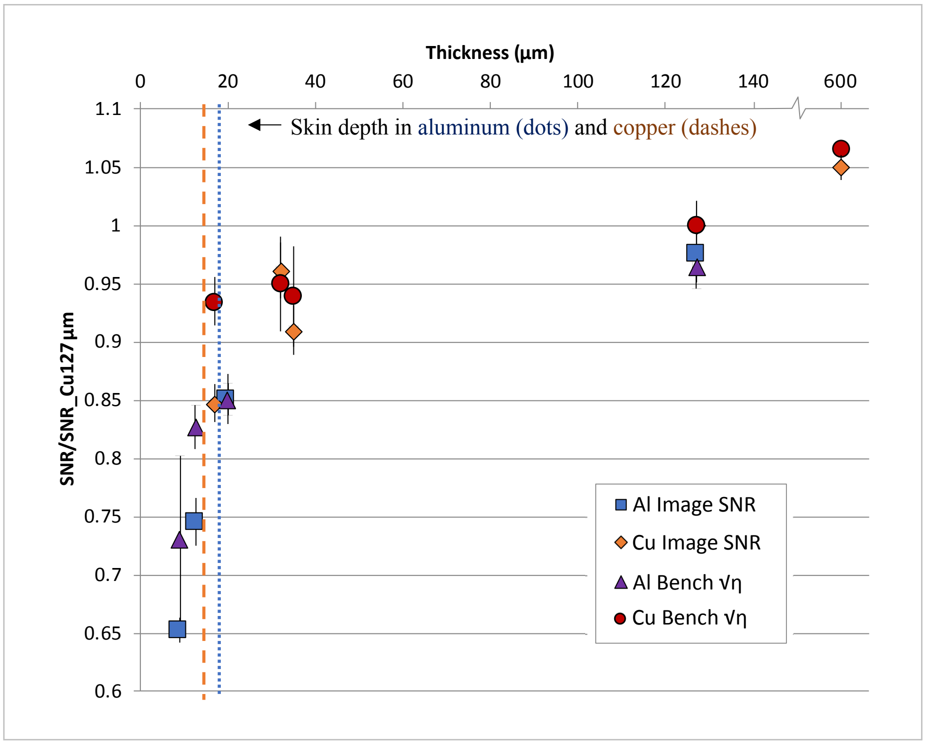

Figure 4.4: SNR relative to that of the 127 μm copper coil obtained from both the images and bench measurements. Mean load impedance of the phantom was 0.41+j0.19 Ω. The range of resonant frequencies was 20.1 to 21.3 MHz.

4.4 Discussion

As predicted, both bench measurements and acquired images confirm that the type and the thickness of conductor affect the achievable SNR. By carefully controlling experimental variables the bench-measured prediction of SNR ratios and the achieved image SNR ratios agree within uncertainty for most coils. The difference exceeded uncertainty in only in two cases (17 μm copper and 13 μm aluminum), for which the uncertainties are likely underestimated.

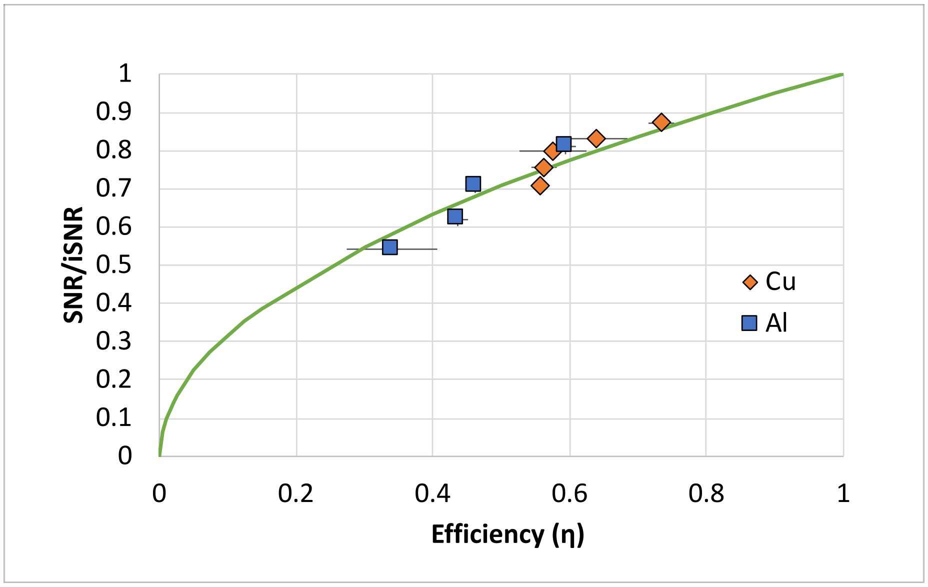

Figure 4.5: The measured image SNR/iSNR plotted against the bench measured efficiency (η). The green curve is the relationship given by Equation (4.1) and iSNR is obtained by fitting.

The calculated efficiency (Table 4.1) demonstrates that at 0.5 T for head-sized phantoms the coils are operating in a transition region between sample-dominated losses (r_S) and coil-dominated losses (r_C). Despite the range in unloaded Q (Table 4.1), all of the tested copper coils have efficiency greater than 0.5. This is reflected in the SNR measurements where the best and worst copper coils differ by about 20% despite the dramatic difference in thickness. The efficiency is also greater than 0.5 for the 127 μm aluminum coil. However, for aluminum the range of thicknesses extends to very thin coils where conductor losses are greater than the sample losses.

This is illustrated by the performance of the 9 μm aluminum coil which is strongly coil-loss dominated ($\eta = 1/3$). Still, this coil is in the range ($\eta > 0.25$) where the slope (Figure 4.5) remains below 1. In terms of SNR performance, this results in a 35% difference between the 127 μm copper coil and the 9 μm aluminum coil despite the over 40 fold difference in areal density.

The 32 μm copper coil is an outlier since it outperforms most other foil coils despite being of intermediate thickness. This coil's traces are machine-cut strips of copper tape and hence have likely overall smoother edges than were achieved by cutting copper and aluminum foil manually with a sharp blade. Edge imperfections (roughness) lead to additional losses because at these frequencies there is current crowding near high-curvature points of the conductor. Current will be especially concentrated at the edges of the cross-section where the imperfections are.

Overall, the measurements indicate that while, certainly, a thickness of multiple skin depths yields the best-performing RF coils, the losses increase only modestly down to thicknesses on the order of one skin depth. The losses nearly double between 127 μm and 20 μm thick aluminum (a factor of 5 smaller thickness), but it only takes a further halving of conductor thickness to 9 μm to increase losses by the same amount again. The data in Figure 4.4 indeed suggest the appearance of an elbow in the SNR performance near 20 μm.

These data are also an experimental exploration of the theoretical relationships in Equation (4.1) and Equation (4.2) [53]. Impacts of material and thickness are lumped together in the total resistance of each coil, or its efficiency. The data are in general agreement with the expected relationship (Figure 4.5). The minimal SNR advantage of the thickest copper (600 μm bars) over the 127 μm standard illustrates that covering a wider range of possible efficiencies will require changes beyond simply the thickness of the conductors (e.g., coil dimensions, capacitor distribution, and/or frequency). The measurements would consequently be more challenging to control and compare.

These measurements were performed at an intermediate field strength of 0.5 T. As field strength (and consequently resonant frequency) increases, the proportion of losses due to the load will increase. At higher field strengths, even thin aluminum coils are expected to operate in the sample-loss-dominated regime, and thus the use of this material in coils for, e.g., PET-MR scanners, is quite feasible.

4.4.1 Radiation Induced Current

This study only investigates the effect of material on image quality in MRI images. To avoid confounding effects, radiation was not delivered during imaging. This means that the imaging performance of these coils during treatment will be degraded further by any external noise sources from the linac, and importantly, by virtue of being in the beam, the image quality will be reduced due to radiation induced current (RIC)[31, 34, 35, 60]. It is difficult to estimate the effect of RIC based on previous studies and in future work that evaluates clinical coils, the effect of RIC must be measured. Based on investigations at 0.2 T and 1.5 T, the predicted SNR loss due to RIC at 0.5 T likely won't exceed the 20% SNR losses seen at 0.2 T even with higher dose rates (600 MU/min) due to the square dependence between signal voltages and field strength, but the SNR loss should be expected to be higher than that seen at 1.5 T for the same reason[31, 35]. Specific investigations are warranted as RIC effects depend on such aspects as the design of the RF-coil and the choice of imaging sequence[34, 35, 60].

4.5 Conclusions

As MRI technology seeks to use RF coils made of thin or alternate conductors for emerging applications, there has been a need to investigate conductors that are lossier than traditional bulky copper conductors. This study presents a verification of the efficiency and SNR relationship for identically-constructed coils under controlled conditions. The coils cover a nearly five-fold range of losses, use the same lumped components, and are evaluated under the same loading conditions. As expected, the losses due to thin conductors are most dramatic when they are thinner than one skin depth at the Larmor frequency. Furthermore, for thick coils the effect of using aluminum rather than copper is found to be minimal when comparing conductors of similar thickness. A 127 μm thick aluminum coil, despite its 20% higher resistance, achieves the same SNR as a 127 μm copper foil conductor. Even the aluminum coil, with several times higher losses (3× higher resistance), achieves SNR better than half that of thick copper and aluminum (65% that of 127 μm copper foil).

These results highlight the fact that a significant change in coil resistance may not lead to a catastrophic loss of SNR, thus justifying the use of thin or alternate conductors in applications where a limited SNR loss is not critical and is outweighed by the advantages gained, such as comfort or radiological transparency (e.g., aluminum).

Chapter 5

B_0 Orientation Invariant Quadrature Detection in a Rotating Linac-MR

5.1 Introduction

RF-coils are an essential piece of the instrumentation needed to achieve real-time image-guided radiation therapy with the combination linear accelerator and magnetic resonance imaging system known as linac-MR or MR-linac. The linac-MR is the next step in improving the radiation therapy treatments that can be provided to patients. It allows for tighter margins, dose escalation and adaptive treatment with fewer side effects [104, 105].

There are several distinct MR-linac combination systems in various stages of development. The Electa Unity and Viewray MRIDIAN are perpendicular systems which means they have a fixed main magnetic field (B_0) that is perpendicular to the beam axis [14, 106]. They have cylindrical windings that generate a magnetic field B_0 along the bore axis, and a linear accelerator is mounted on a gantry to rotate around the bore, with beam being along an axis orthogonal to B_0. The perpendicular arrangement of the treatment beam and B_0 leads to perturbations in the dose deposition because the Lorentz force bends the paths of secondary electrons. The Alberta Linac-MR and the Australian MRI-linac are parallel systems, meaning their treatment beams are parallel to B_0. While in the Australian MRI-linac both B_0 and linac are fixed[15, 16, 28], the Alberta Linac-MR has a magnetic field that co-rotates with the beam gantry. The B_0 is generated by magnets mounted on the same gantry as the linear accelerator [12, 22]. The Alberta Linac-MR has the ability to treat from all gantry angles, including arc treatments, by rotating this gantry, in contrast the fixed gantry Australian MRI-Linac requires rotation of patient instead. Unlike the Unity and MRIDIAN systems, the Alberta Linac-MR also maintains a parallel orientation of the B_0 and treatment beam, which means the dose deposition is not significantly distorted as seen in perpendicular systems. The field in a parallel system causes electrons to follow helical trajectories but does not deflect them in a particular direction [27]. One challenge of parallel systems is that if the B_0 is poorly shielded in the head of the linac and for a section of the air column, it will trap and guide head scatter and air scatter electrons toward the patient, leading to an increase in surface dose [33, 79].

Despite their differences, all linac-MR systems need to achieve precise treatment delivery and excellent rapid imaging of soft-tissue structures. The latter can only be accomplished with high SNR obtained from specially designed RF-coils.

A key aspect of RF-coils for linac-MR systems that has been studied extensively is the interaction between RF-coils and the radiation beam. Traditional surface arrays placed in the beam can increase the surface dose several fold, which could lead to unwanted and harmful skin reactions in patients [33, 100], even if the dose to the target site is unchanged [32]. Several ways to address this issue have been proposed and tested. In perpendicular systems, the Lorentz force on electrons generated in the coils has been exploited by using spacers to generate an airgap between the RF-coil array and the patient [31]. Imaging quality is also affected by the interaction of radiation with in-beam coils. Conductors made from thin copper and aluminum have been evaluated in this thesis (Chapter 4) and the surface dose effect of such conductors has been measured for parallel systems (with relevance to perpendicular systems as well) as described in Chapter 3. Out-of-beam RF-coils, which avoid collisions between the radiation beam and the coil altogether, are another conceptually simple solution to undesired consequences of beam and RF-coil interactions. Out-of-beam coils have been explored for the Australia Linac-MR [37] and for the Alberta linac-MR [36].

The rotating B_0 (around the patient axis) is a unique property of the Alberta Linac-MR. In addition to avoiding interactions with the treatment beam, RF-coils for the Alberta linac-MR also need to be designed with consideration of how image quality varies as a function of gantry rotation. The rotation of the B_0 means the magnetization's plane of precession will be different at different gantry angles. The patient axis is always perpendicular to B_0 and a coil sensitive to this axis will have angle-invariant SNR. The second component of precession, however, rotates in the patient transverse plane along with B_0 though always orthogonal to B_0 (Figure 1.1). In earlier work, quadrature-like detection was achieved with out-of-beam coils, by combining widely spaced single turn and double butterfly channels [36]. The loop and butterfly coils were decoupled thanks to wide spacing, and SNR was detected at three gantry angles.

This chapter describes a three channel coil array that is planar. All channels are positioned in a coil stack, ensuring stable geometric decoupling since all three channels are in one piece. This arrangement can be used along with immobilization devices or additional coils. The theory behind stacking a single turn and two orthogonal butterflies into a three channel array sensitive to all components of magnetization has been explored before using multi-modal arrays, in which the array can operate in one of several resonant modes. For example, a spoked design coil can be used in various modes (single turn, butterfly, or even quadrants), based on the shape of the coupling loop [107]. More generally stacked resonators with sensitivities along different axes are commonly investigated, though typically limited to quadrature coils. Two coils generate mutually orthogonal fields that are also both orthogonal to B_0, with the goals being higher densities of coil elements in arrays or boosting sensitivity of single turn coils with an orthogonal channel [108–110]. Three orthogonal square loops have been investigated in simulation as a way to detect arbitrary fields, but being identical loops the arrangement could not be planar [111].

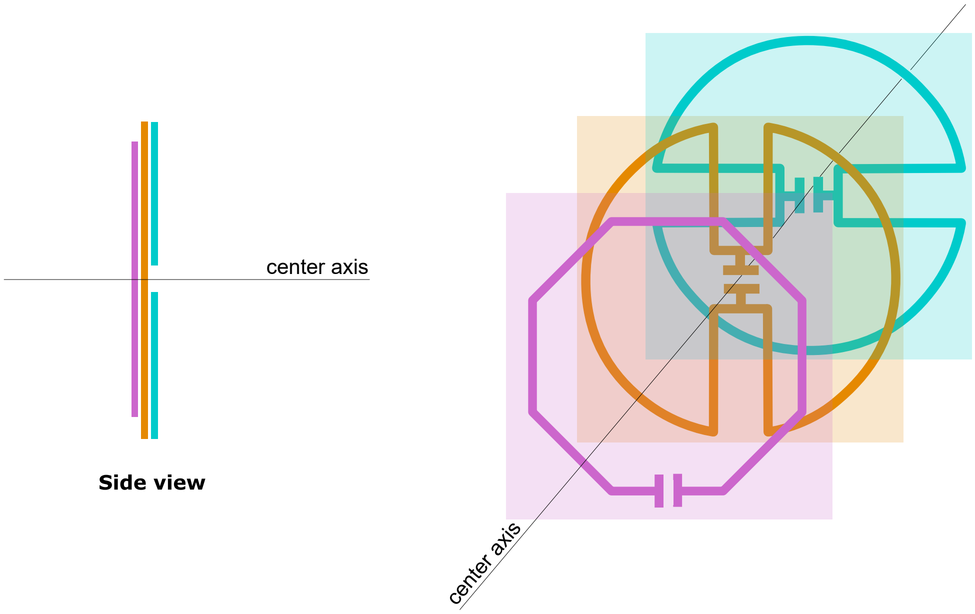

Figure 5.1: A stacked, planar three channel array. A single turn (pink), a vertical butterfly (orange), and a horizontal butterfly (blue), are co-axial arranged and placed close together to minimize set-up complexity. This single piece planar array achieves quadrature detection independent of gantry angle. Pavel Barta ©. Used with Permission.

Two butterflies and a single turn coil are sufficient to capture both components of precession in any plane as the primary sensitivity axes of the three coils are mutually perpendicular. A single turn coil is sensitive along the axis normal to the plane of the coil (transverse plane). A butterfly is sensitive to an axis in the transverse plane. If one of two butterflies is rotated 90°; then one will be sensitive to the axis normal to the sagittal plane and the other to the axis normal to the coronal plane.

The geometry chosen for the three channels should also ensure zero mutual inductance is achievable between each pair of coils. A single turn coil concentrically overlaid on a butterfly will overlap equally with each of the two lobes of the butterfly.

The lobes generate equal and opposite fields, hence there is zero mutual inductance. Similarly, the symmetry of each lobe of a butterfly leads to zero mutual inductance between a rotated butterfly pair.

The goal of this study is to design, build, and characterize the first planar three-channel array, intended for head imaging, that achieves gantry angle independent imaging and completely avoids collisions between the radiation beam and the coil. To date there have been no investigation of such an array and no study has investigated the change in SNR of a triply orthogonal array over a 180° gantry rotation.

5.2 Methods

5.2.1 Theory

The three-channel array for the Alberta 0.5T Linac-MR consists of a single loop coil and two butterfly coils arranged co-axially. The butterflies are rotated 90° with respect to each other. This orthogonal arrangement gives the desired sensitivity to magnetization precessing in any plane and allows all three channels to be decoupled geometrically.

In case of the rotating B_0, the sufficiency of this design can be described visually as in Figure 5.2 and in words as follows: Let s_C be the signal received by an upright single turn coil, and let $\hat{C}$ be the patient inferior to superior axis. Note that the single turn coil is sensitive primarily to magnetization along the $\hat{C}$ axis. Let s_H be the signal received by a butterfly coil with the the plane of symmetry being the patient sagittal plane (horizontal butterfly coil), and let $\hat{H}$ be the patient left to right axis. Note that the horizontal butterfly coil is sensitive primarily to magnetization along the $\hat{H}$ axis. Let s_V be the signal received by a butterfly coil with the the plane of symmetry being the patient coronal plane (vertical butterfly coil), and let $\hat{V}$ be the patient posterior to anterior axis. Note that the vertical butterfly coil is sensitive primarily to magnetization along the $\hat{V}$ axis.

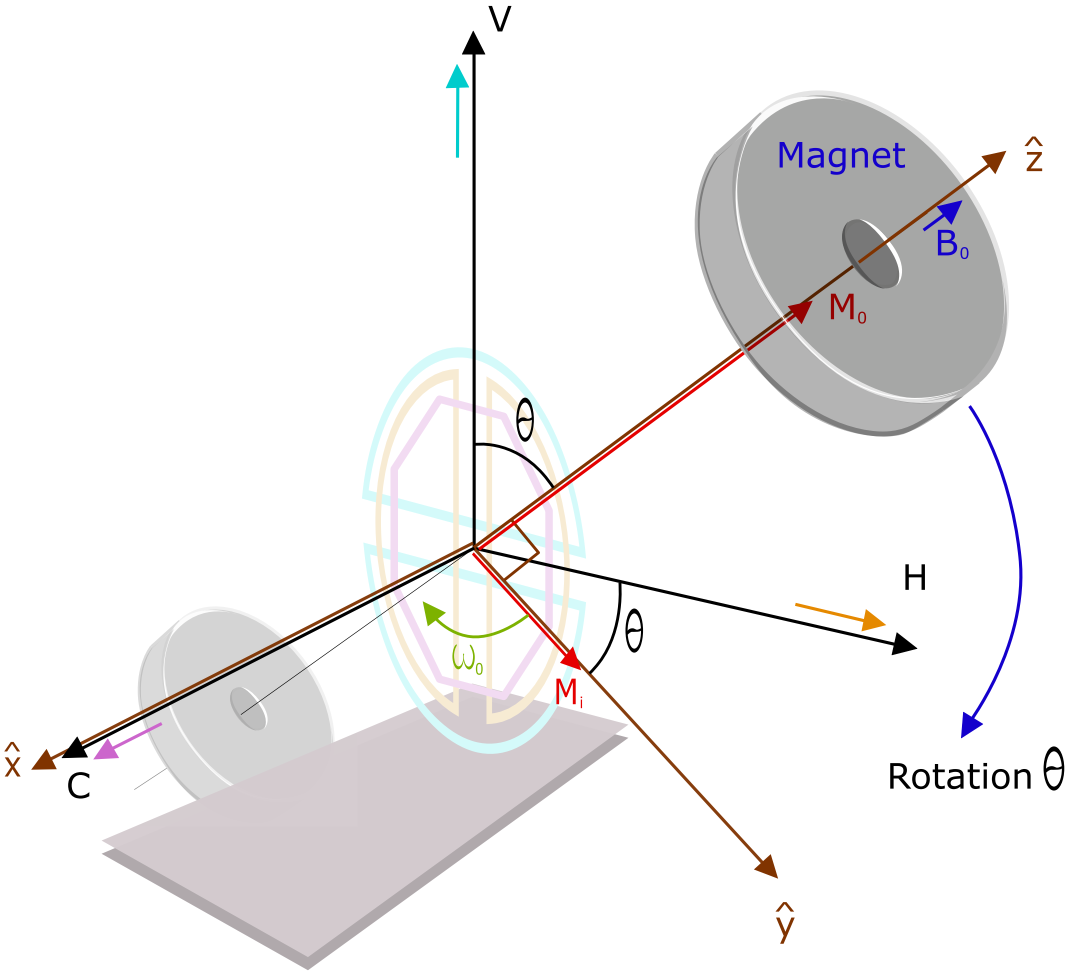

Figure 5.2: The axis (black) defined by the patient and the static RF-coil array is marked by the axis labels C, H, and V. When the gantry holding the magnet and linac is rotated to some gantry angle θ the main magnetic field B_0 defines the axis (brown) marked by $\hat{x}$, $\hat{y}$, and $\hat{z}$. The magnetization (red) which will precess about $\hat{z}$ can be described by components osillating at the Larmor frequency along C, H, and V using simple geometry. Each of the coils in the array is primarily sensitive to one of the components C, H, and V. By combining the Larmor frequency signal in each of these coils the magnetization in the xy-plane, M_i is detected in a quadrature-like manner. It is detected both when along $\hat{x}$ and $\hat{y}$ regardless of the gantry angle θ. Pavel Barta ©. Used with Permission.

Based on the reference frame defined by the orthogonal $\hat{C}$, $\hat{H}$, $\hat{V}$, as the gantry rotates, B_0 will rotate in the $\hat{H} - \hat{V}$ plane. Consider the B_0 at some angle θ with respect to $\hat{V}$. In the typical reference frame then, where the z-axis is along B_0, the magnetization can be described by Equation (2.9):

$$\begin{aligned} M_x(t) =& M_i \cos(\omega_0 t) e^{\frac{-t}{T_2}} \\ M_y(t) =& -M_i \sin(\omega_0 t) e^{\frac{-t}{T_2}} \\ M_z(t) =& M_0 \left(1 - f e^{\frac{-t}{T_1}}\right) \\ f =& 1 - \frac{\sqrt{M_0^2 - M_i^2}}{M_0} \end{aligned} \tag{5.1}$$

The magnetization can be described in terms of the coil array co-ordinate system in terms of θ by:

$$\begin{aligned} M_C(t) =& M_i \cos(\omega_0 t) e^{\frac{-t}{T_2}} \\ M_H(t) =& -M_i \sin(\omega_0 t) e^{\frac{-t}{T_2}} \cos(\theta) + M_0 \left(1 - f e^{\frac{-t}{T_1}}\right) \sin(\theta) \\ M_V(t) =& M_i \sin(\omega_0 t) e^{\frac{-t}{T_2}} \sin(\theta) + M_0 \left(1 - f e^{\frac{-t}{T_1}}\right) \cos(\theta) \end{aligned} \tag{5.2}$$

The signal is proportional to the magnetization (see Equation (2.22)). The signal in each coil also depends on a spatially dependent sensitivity, which is described by the spatial term (Equation (2.24)). The magnetic field produced by each of the coils is dominantly along the described primary axes, $\hat{C}$, $\hat{H}$, and $\hat{V}$. Consider the initial magnetization M_i at point in the sample where all three coils have comparable spatial term magnitude(let $\left|\vec{S}_p\right| = 1$, Equation (2.24))). Ignoring relaxation, the signal due to this magnetization then is given by:

$$\begin{aligned} s_c(t) =& -\omega_0 M_i \sin(\omega_0 t) \\ s_h(t) =& \omega_0 M_i \cos(\omega_0 t) \cos(\theta) \\ s_v(t) =& -\omega_0 M_i \cos(\omega_0 t) \sin(\theta) \end{aligned} \tag{5.3}$$

Note that in a root sum of squares combination the s_H and s_V will result in $\omega_0 M_i \cos(\omega_0 t)$. This is the quadrature component complementary to s_C, giving quadrature-like reception at any gantry angle θ.

The geometric decoupling between the channels is best described graphically (Figure 5.3). Between each pair of coils the equal but opposing components of mutual flux cancel, leading to no net mutual inductance between the coils.

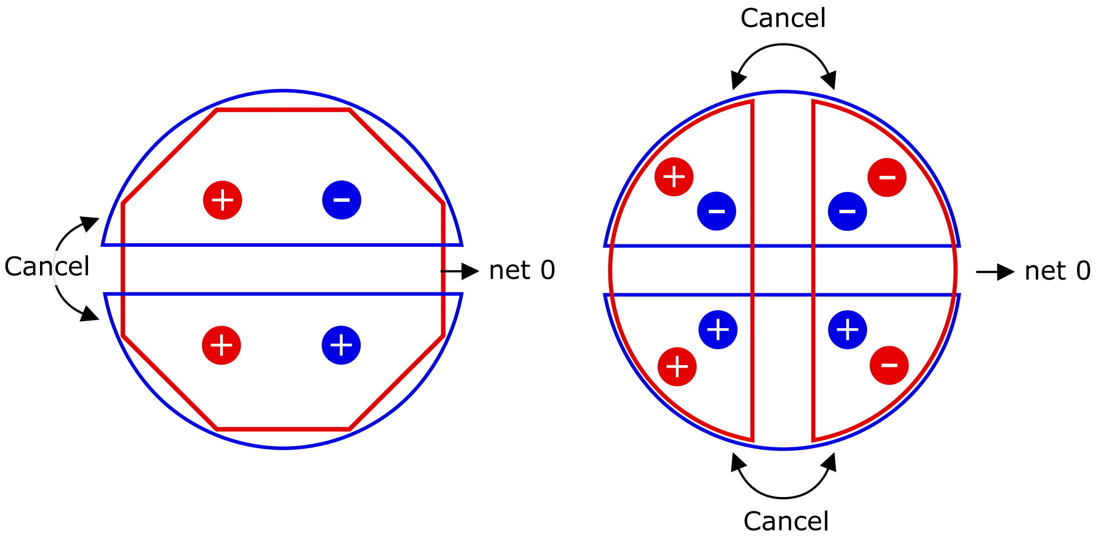

Figure 5.3: A visualization of the geometric decoupling that is achieved by the symmetry of the the coil channels. Plus and minus symbols represent the sign of the coupled signal. In each case, because the geometry is symmetric, each coupling magnitude will be equal. The interaction between coils is dictated by the product of their coupling and the signals in each coil. When there are multiple segments with different products the effects must be added together. On the left, the coupling between the single turn coil and each lobe of the butterfly is equal and opposite leading to a net zero coupling. On the right is shown two overlapped butterfly coils. Due to the 90° rotation the opposing phases in each lobe lead to 4 equal couplings, two of each effective sign. Once again when summed, the net effect on the signal in each coil due to the other is zero. Pavel Barta ©. Used with Permission.

5.2.2 Construction

The array layout was designed in Kicad (https://www.KiCad.org/) and was printed by a PCB manufacturer (JiaLiChuang [HongKong] Co., Limited). Two butterfly coil patterns were printed on opposite sides of a biplanar PCB using 70 μm copper traces for minimum resistance. Each butterfly consists of two mirrored D shapes with the pair forming a broken circle with a 15 cm radius. The third coil element, a single octagonal loop, was made using 1.27 cm wide self-adhesive copper tape (Venture Tape Corp. No. 1725, Rockland, MA, USA) adhered to a cardboard base. The tape was 32

μm thick copper and each segment had an outer length of 8 cm. Four indexing holes at the corners of the PCB and cardboard base allowed for precise co-axial positioning of all three elements. Plastic screws and tape held the octagon firmly to the PCB.

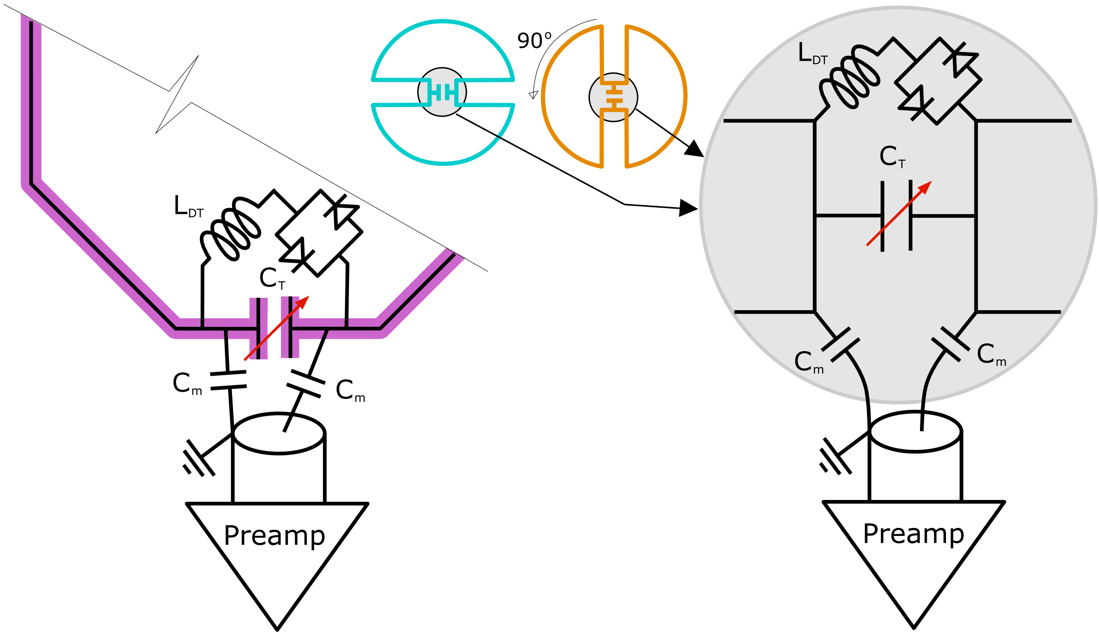

Figure 5.4: The matching and tuning circuits for the single turn coil are shown on the left and for the butterfly coils on the right. Note the parallel de-tuning circuit consisting of L_{DT} and cross-diodes in series. The tuning capacitor (C_T) was a variable capacitor in each case, while the matching capacitors (C_m) were fixed. Pavel Barta ©. Used with Permission.

Tuning elements were mounted at central locations, connecting the two butterfly halves in parallel (Figure 5.4). Vias connecting the two planes of the biplanar PCB allow all matching elements to be mounted on the same face of the biplanar PCB. Additionally, cables could be mounted on the same side (Figure 5.5. For the octagon coil the tuning and matching were mounted at one segment of the loop (Figure 5.4)

5.2.3 Bench Measurements

The coil stack was mounted vertically and placed next to a phantom. Bench measurements of unloaded quality factor (Q), resonance frequency, return loss, and decoupling

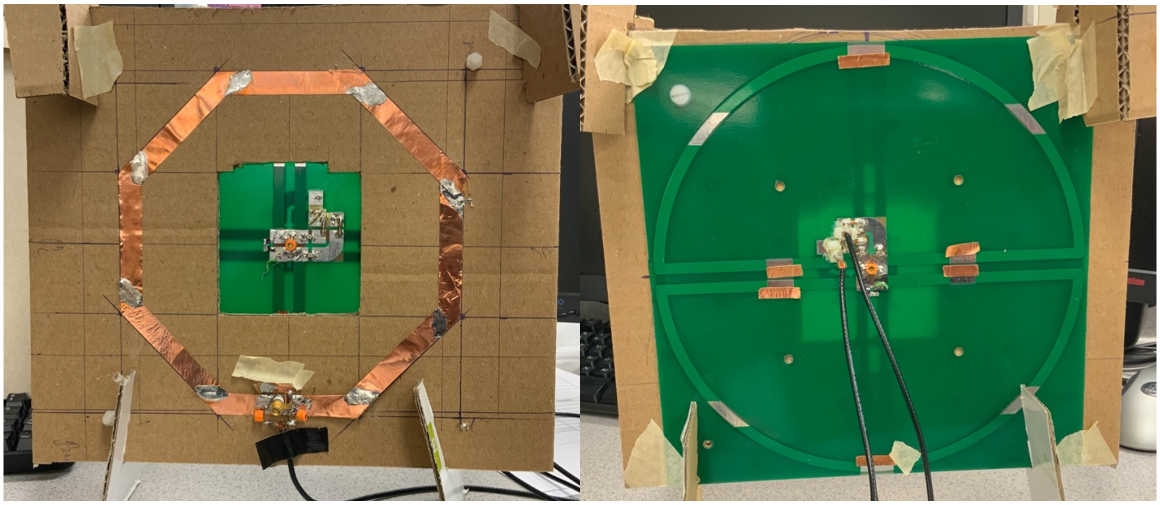

Figure 5.5: Left: The copper tape trace of the octagonal coil including the mounted capacitors. The tuning and matching capacitors for the horizontal butterfly are visible in the cutout of the cardboard. Right: The trace of the vertical butterfly partly masked by green paint. Faintly visible through the board is the horizontal butterfly on the opposite side of the two sided board. Copper tape segments used to slightly shift the current paths to improve decoupling between the butterflies are visible on the vertical butterfly.

were made with a Vector Network Analyzer (VNA) (Rohde & Schwarz ZVL3, Munich, Germany). Matching and tuning were adjusted iteratively cycling through all three channels. Q was measured with an S_{21} measurement between the measured channel and a small sniffer probe. Coupling was also optimized through the addition of copper tape segments to adjust mutual capacitance and/or inductance between the various channels. Copper tape was adhered off-center on exposed soldering pad segments of the butterfly loop. The copper segments provide parasitic current pathways that shift the effective shape of the butterfly coil.

For each pair of channels decoupling was optimized by fine adjustments of the tuning and matching capacitors while retaining at least -20 dB return loss and system frequency for each channel. The third channel was then adjusted to achieve the best isolation to the other channels while also retaining -20 dB return loss at the Larmor frequency within the 3dB resonance peak for each channel. Each of the coils was checked and minor capacitor and alignment adjustments were made if needed.

5.2.4 Imaging

Imaging experiments were conducted on the Alberta 0.5T Linac-MR with x-ray beam off to investigate the gantry dependent imaging properties of the coil array as a function of the changing orientation of the magnetic field. The imaging subject was a cylindrical aqueous phantom (19 cm ⊘, 15 cm high, 55 mM NaCl and 5 mM $NiCl_2$; ASG Superconductors, Genova, Italy) positioned coaxially and 2.6 cm away from the coil array as shown in Figure 5.6. The phantom is positioned with its long axis along the table and its center located at the system iso-center. The coil array was positioned vertically in the bore, standing on the treatment table with the coil array being co-axial with the bore and hence the gantry's axis of rotation (see Figure 5.6).

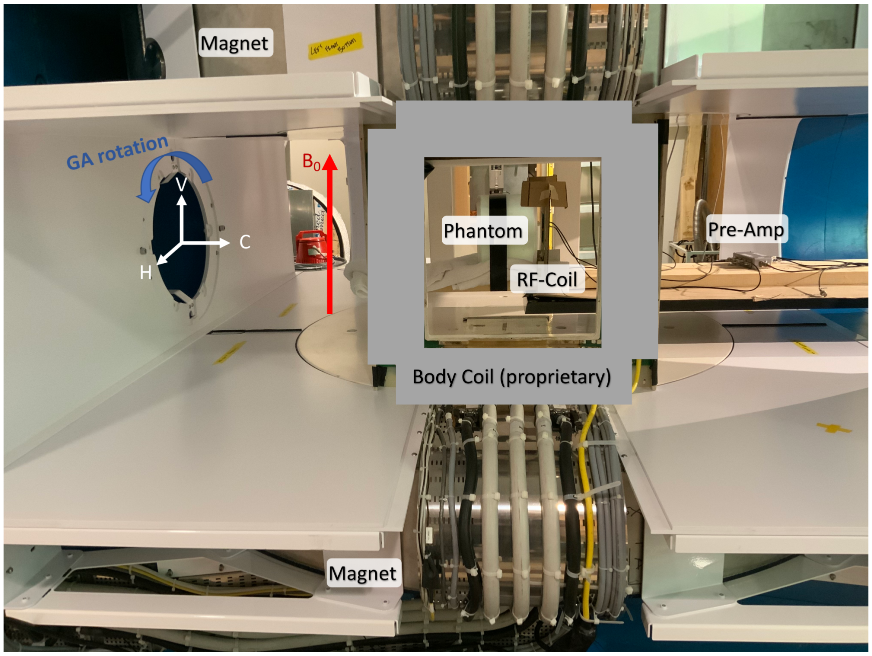

Figure 5.6: The in-bore set-up of the planar three channel array as positioned next to the cylindrical phantom. Axes of sensitivity for the three channels are shown and the gantry angle rotation is depicted.

A gradient-echo imaging sequence (field of view = 25 × 25 cm^2, 10 cm thick slice, TE = 12 ms, TR = 330 ms, nominal flip angle = 60°) was used to evaluate the performance of the coil array at a range of gantry angles (-90° to 90°). The array and phantom were kept stationary on the couch and the gantry was rotated to each gantry angle. Transverse, coronal and sagittal slices were acquired through the center of the phantom in the same planes at each gantry angle. To determine SNR, a noise-only image was also acquired at each gantry angle with identical imaging parameters, but without an excitation pulse.

The isolated performance of each individual coil channel and the combined image at each gantry angle was evaluated using MATLAB scripts (The Mathworks Inc, Natick, Massachusetts, United States). Individual channel SNR was evaluated as the ratio of the mean signal from the 5 cm x 5 cm central region of the phantom and the standard deviation of the noise-only image. A combined SNR image was generated using weighted root sum of squares (wRSS) [64, 65] and the combined SNR was taken as the mean signal from the 10 x 10 cm central region of the phantom in this wRSS image. For the coronal and sagittal slices the depth profiles were also generated to evaluate drop-off in sensitivity as a function of distance from the array. The depth profile was obtained by averaging the central 10 cm at each depth across the phantom. The isolation of the channels was evaluated by generating noise correlation matrices from the noise-only images and plotting the off-diagonal elements as a function of gantry angle.

In addition to SNR measurements, the flip angle was mapped in the same slices as for the SNR measurements at 0° and 90° gantry rotations using the double angle method (using nominal 45° and 90° flip angles). A volume transmit coil was used for all acquisitions.

5.3 Results

The bench measured Q-values and couplings for the coil array, after iterative adjustment of all three channels, are given in Table 5.1. The matched Q of all three coils is 100. These matched Q-values are reasonable for the frequency of interest and given the conductor used. The coupling between any two channels was at or better than -16 dB. The highest coupling of -16 dB occurred between the two butterflies which share opposite sides of the PCB board and thus couple capacitively. This coupling is acceptable for imaging and similar or higher values are found often in the literature [110, 112].

Coil Element	**Unloaded Q-Value**	**Loaded Matched Q-value**	**Coupling to Next Coil Element (dB)**
Octagonal Loop	100 ± 10	100 ± 10	
			-31
Horizontal Butterfly	110 ± 10	100 ± 10	
			-16
Vertical Butterfly	100 ± 10	100 ± 10	
			-40

Table 5.1: Bench Measured Q-values and Decoupling between channels.

Good image quality was achieved with the array at all gantry angles and for all three slices (Figure 5.7-5.10). The SNR of the combined array averaged 32 ± 4 across all gantry angles (Figure 5.11-5.13). The performance of the array is approximately constant across all the gantry angles, with some outliers in the coronal slice images acquired at the -45°, -67.5°, and -90°. The SNR in these images is lower than that in transverse and sagittal images.

The SNR of the individual butterfly channels varies with gantry angle as expected based on the changing plane of precession (Figure 5.6). The horizontal butterfly varies as the cosine of the gantry angle and the vertical butterfly varies as the sine of the gantry angle, while the octagonal loop has approximately constant performance at each gantry angle.

As expected, the SNR fall-off with depth for the butterflies is more rapid than for the octagonal loop (Figure 5.14-5.16) [113]. While the butterflies have higher SNR

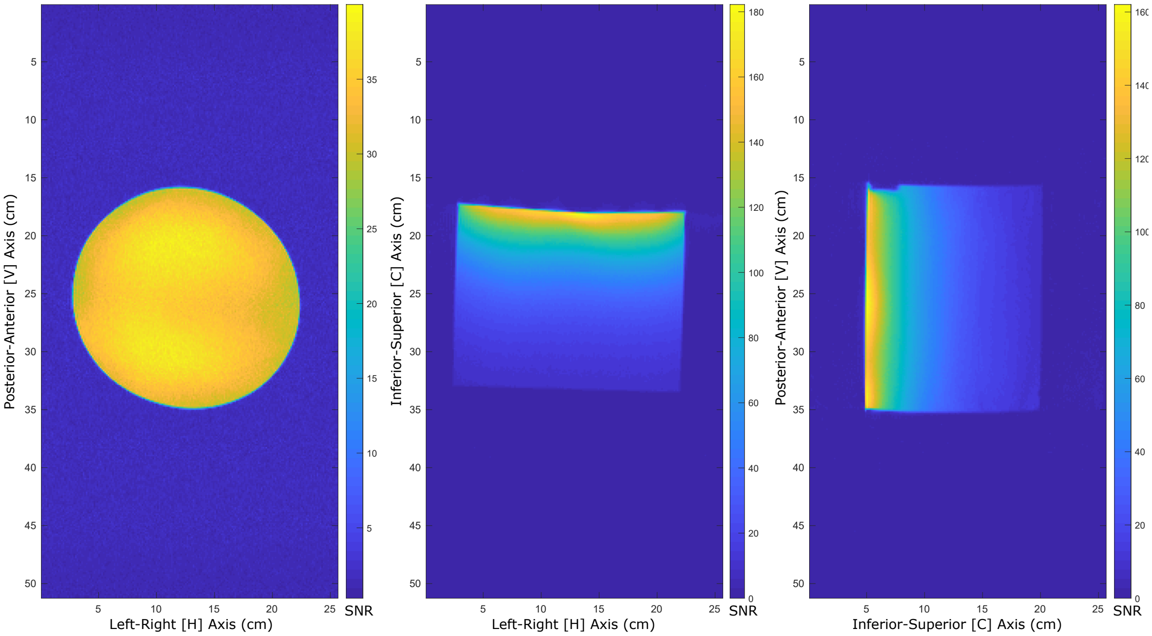

Figure 5.7: Example combined wRSS SNR images at gantry angles 0° (transverse slice shown), 45° (coronal slice shown), and 90° (sagittal slice shown) [from left to right].

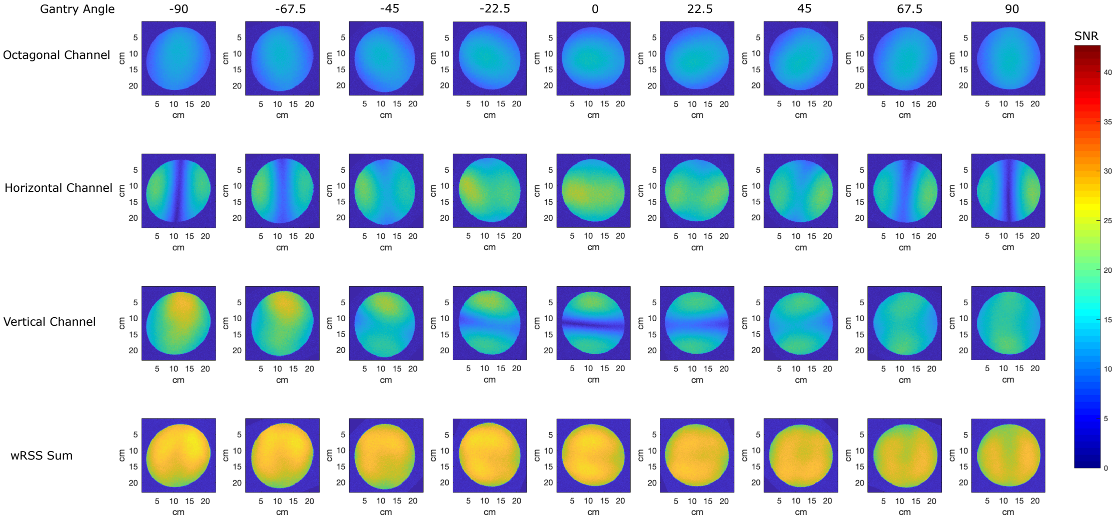

Figure 5.8: Individual channel SNR images and the combined wRSS SNR images at each gantry angle for the transverse slice.

Figure 5.9: Individual channel SNR images and the combined wRSS SNR images at each gantry angle for the coronal slice.

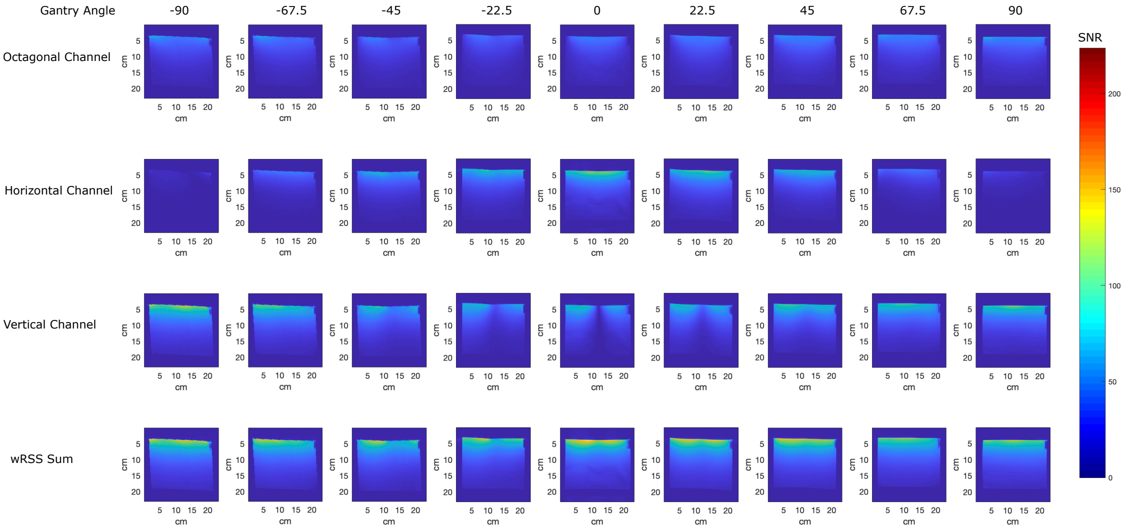

Figure 5.10: Individual channel SNR images and the combined wRSS SNR images at each gantry angle for the sagittal slice.

near the coil, at the center of the phantom where the transverse slice is acquired they achieve similar SNR to that achieved by the loop. Furthermore, the depth profile looks significantly different for the butterflies at the various gantry angles, as their overall sensitivity changes with the rotation of the precession plane (gantry angle).

Because isolation between the channels is very good, the highest noise correlation

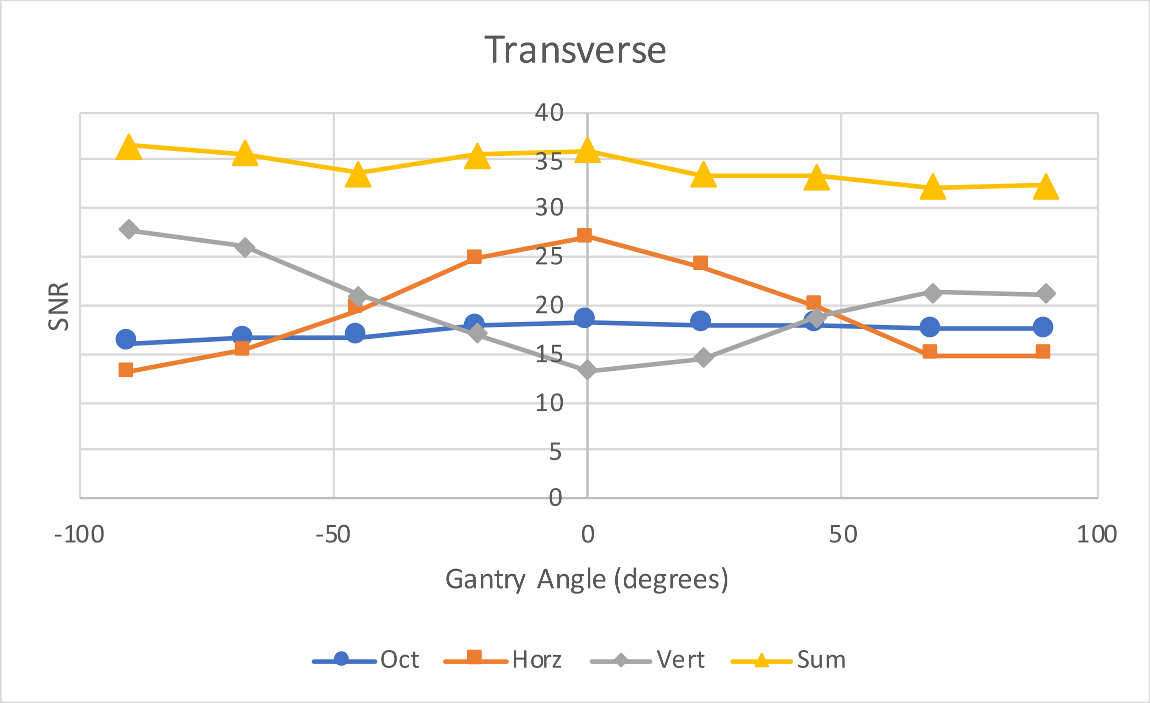

Figure 5.11: SNR variation in the transverse slice across gantry angles for individual channels and for the wRSS combined image. Reported values are the average of the central 5 cm x 5 cm of the image (10 cm slice thickness).

value is merely 5% between the octagonal loop and horizontal butterfly channels at a gantry angle of 22.5° (Figure 5.17)

Acquired flip angle maps (Figure 5.18) show good uniformity is maintained across the extent of the phantom with a reduction in flip angle occurring right next to the coil, which suggests less than perfect detuning achieved using passive crossed-diode traps [43]. The flip angle map was not successfully acquired for the coronal slice at the -90° gantry angle due to a technical error. The flip angles achieved were likely not outside the linear region of the cosine curve, which is needed for the double-angle method to work.

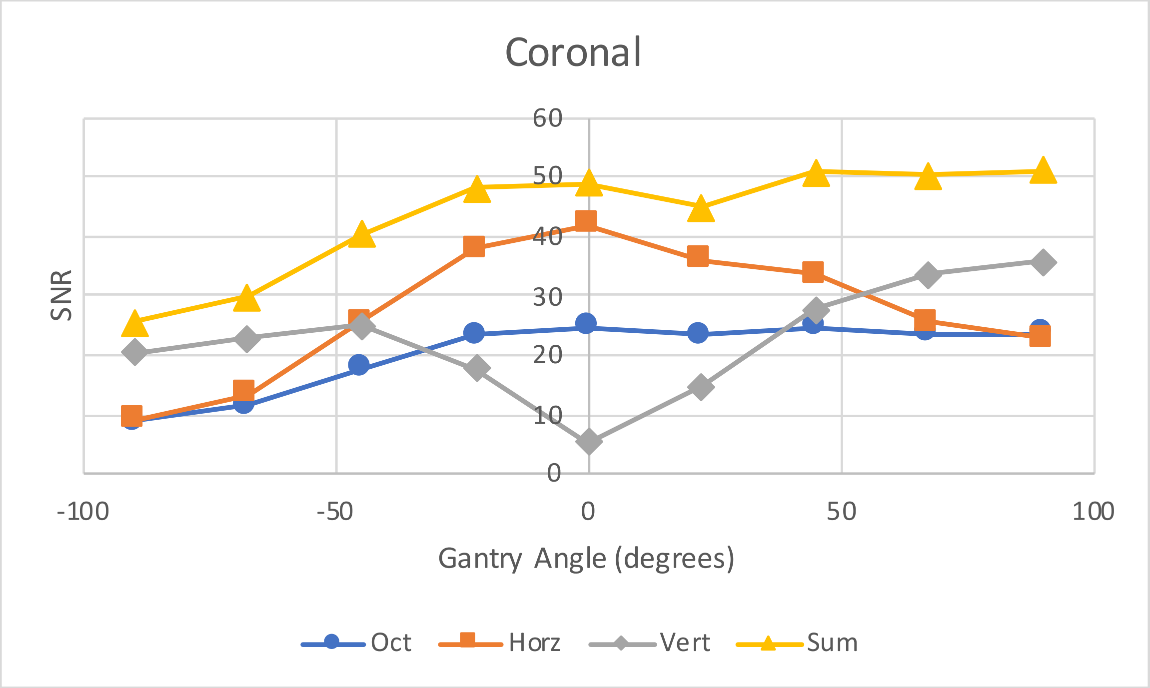

Figure 5.12: SNR variation in the coronal slice across gantry angles for individual channels and for the wRSS combined image. Reported values are the average of the central 5 cm x 5 cm of the image (10 cm slice thickness).

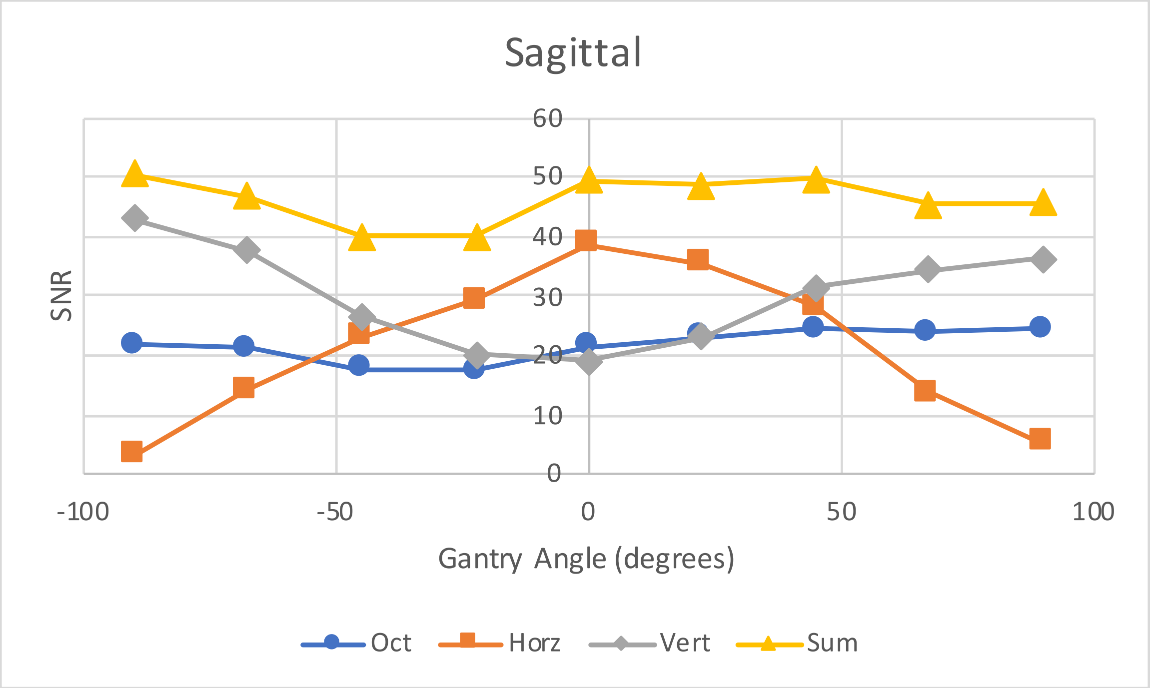

Figure 5.13: SNR variation in the sagittal slice across gantry angles for individual channels and for the wRSS combined image. Reported values are the average of the central 5 cm x 5 cm of the image (10 cm slice thickness).

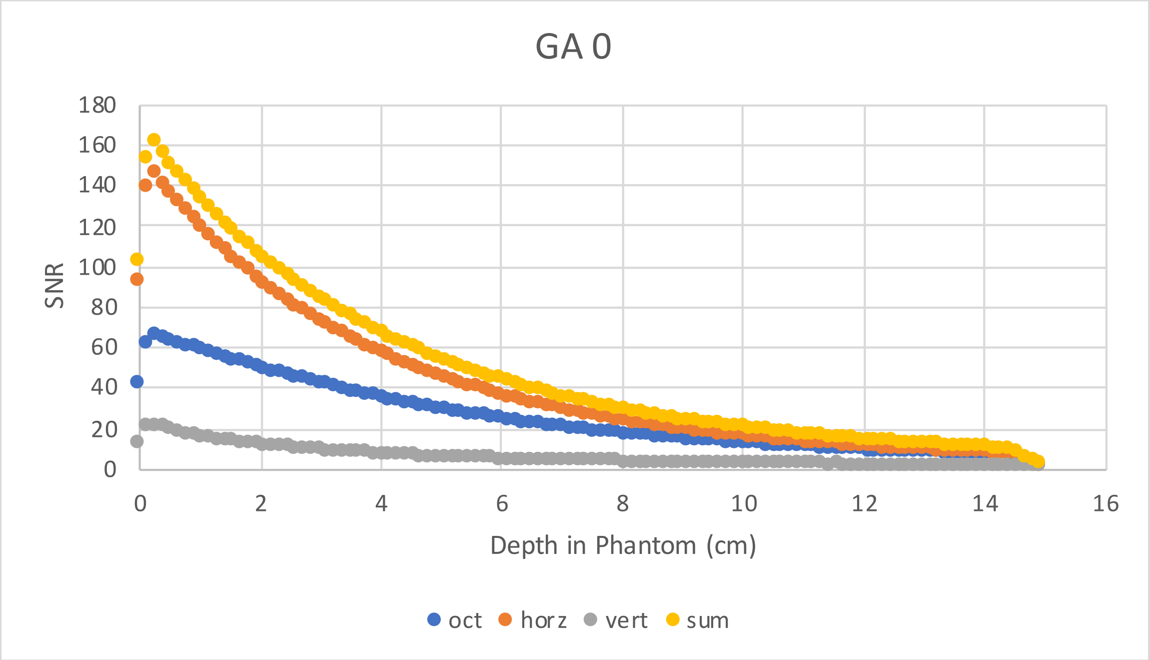

Figure 5.14: SNR as a function of depth from coronal slices acquired at a gantry angle of 0°.

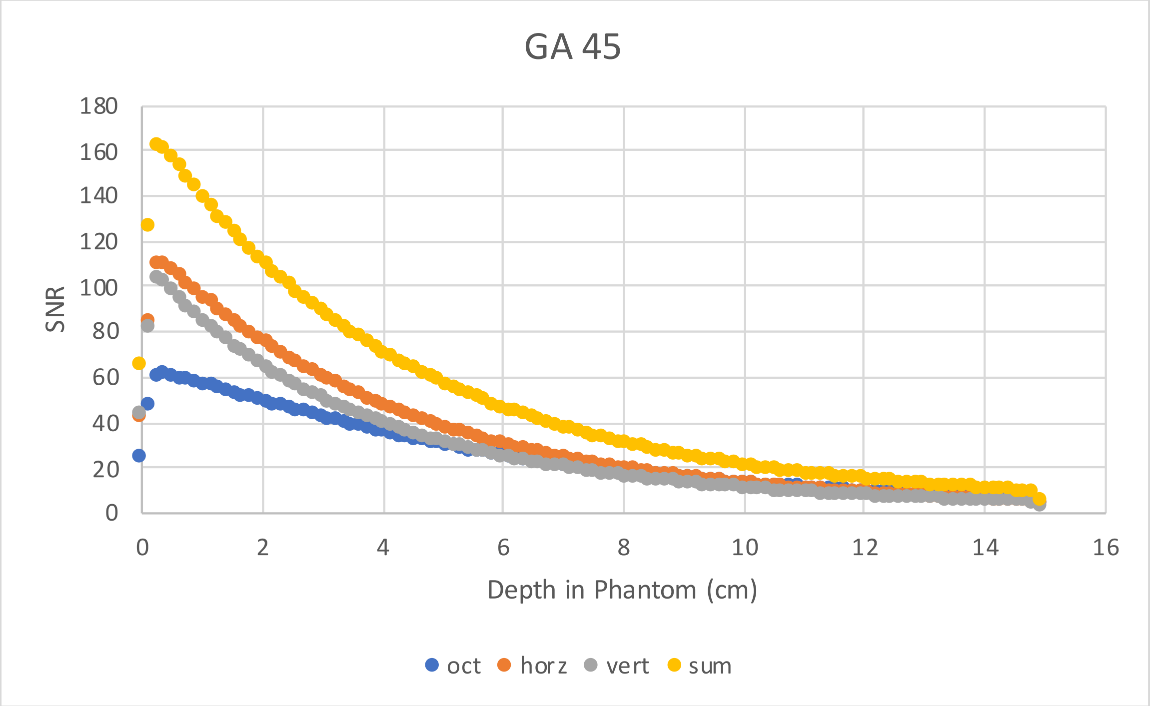

Figure 5.15: SNR as a function of depth from coronal slices acquired at a gantry angle of 45°.

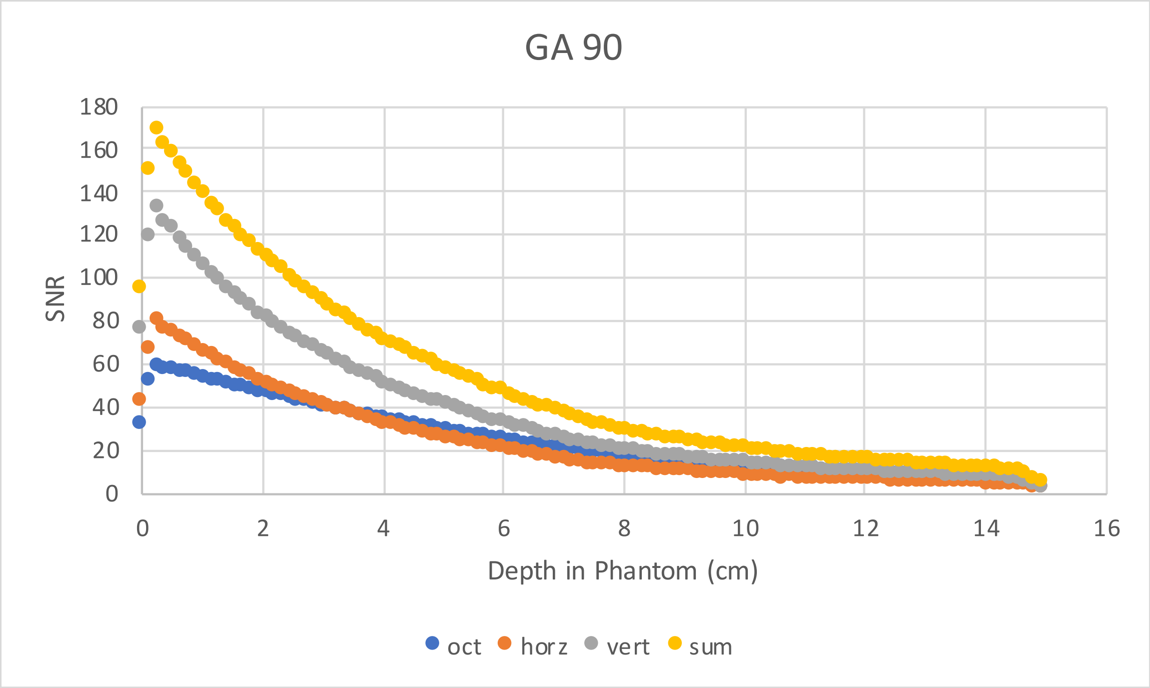

Figure 5.16: SNR as a function of depth from coronal slices acquired at a gantry angle of 90°.

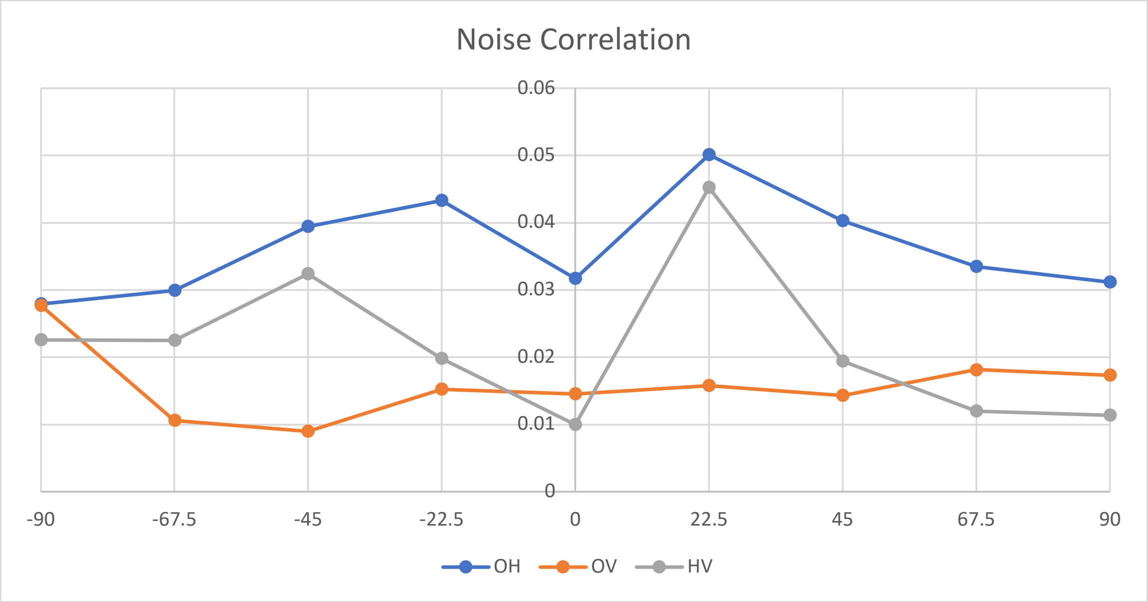

Figure 5.17: Gantry dependence of the noise correlation coefficients between octagonal (O), horizontal (H), and vertical (V) channels of the planar array.

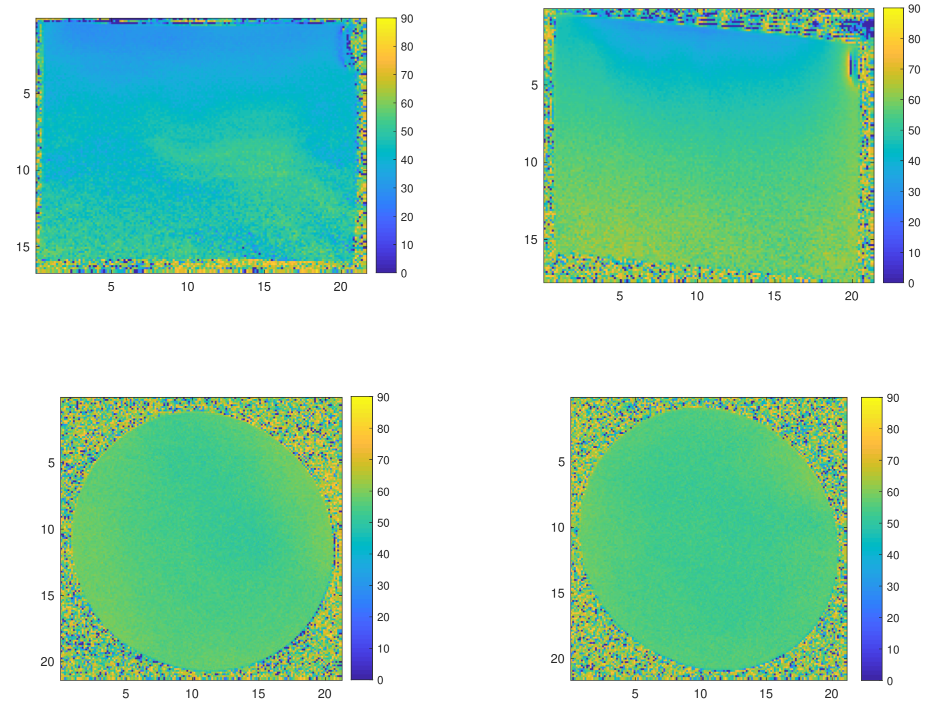

Figure 5.18: Flip angle maps of combined images (wRSS): Top left: Gantry angle of 0°, sagittal slice. Top Right: Gantry angle of -90°, sagittal slice. Bottom Left: Gantry angle of 0, transverse slice. Bottom Right: Gantry angle of -90°, transverse slice.

5.4 Discussion

The coil array is designed to be positioned at the top of the patient's head. This leads to poorer coupling between the coil and the sample than in designs that wrap around the head. Bench measurements highlight that the coils are not heavily sample-loaded, and are operating in the coil loss dominated regime. Copper conductors of sufficient thickness (35 μm and 70 μm) are needed to construct low loss coils.

The combined reconstructed images highlight the image quality that was achieved with the coil and the chosen imaging sequence. The phantom extent is easily identified, and the transverse slices are very uniform which is as expected for a uniform phantom imaged with this array. In the coronal and sagittal slices the expected fall off of the signal way from the planar array is evident.

The essential image quality requirement for this array is its stability with gantry angle. This feature is demonstrated in the plots of SNR against gantry angle (Figure 5.11-5.13). Most cleanly this is seen in the transverse slice where the SNR varies by less than 10% across all gantry angles. This kind of variation (<10%) will not be visually noticeable and hence the combined SNR is deemed constant across all gantry angles (-90° to 90°). While measurements were only done for a 180° rotation, due to the symmetry of the array and the symmetry seen in the measurements, very similar results are expected over 360°. This constant image quality comes from the combination of a constant baseline provided by the octagonal coil channel, and the two butterfly coil channels that vary sinusoidally, but 90° out of phase with respect to each other. This result suggests the array is an excellent option for imaging during typical treatments that involve radiation delivery from multiple gantry angles.

The horizontal butterfly channel has a maximum SNR at a gantry angle of 0° and follows a cosine curve to minimums at -90° and 90°. Conversely the vertical butterfly channel has a minimum at 0° and reaches maxima at -90° and 90°. In the center of the phantom where the transverse slice is acquired, at 45° the three channels all have very similar SNRs. This is possible because the butterflies have higher peak SNR than the octagonal channel. In this design arrangement the octagonal channel acts as a baseline boost to the butterfly channels, and helps ensure SNR of the array doesn't fall too rapidly with depth in phantom. The complementary SNR profile of the butterflies and octagonal channels is further emphasized by the depth profiles at each gantry angle (Figure 5.12 to 5.14). The butterflies are characterized by faster fall-offs with depth than the octagon and their higher peak performance. This is in line with the expectations for two different styles of coil [113].

It should be noted that the horizontal butterfly channel signal does not drop in SNR as much at 90° (Figure 5.16) as the vertical butterfly channel signal does at 0° (Figure 5.14). This is to be expected due to the 90° rotation between the horizontal and vertical butterfly coils and because the coronal imaging plane does not rotate with the gantry. Since the coronal and sagittal slices are defined with respect to the phantom, they are along different lines of symmetry for the two butterfly coils as a function of θ. This can be seen in the individual channel transverse images in Figure 5.8. The coronal slice acquired with the vertical butterfly at a gantry angle of 0° is analogous to the sagittal slice acquired with the horizontal butterfly at a gantry angle of 90° or -90° (compare Figure 5.9 and Figure 5.10).

The behaviour of the horizontal and vertical butterfly channels is not quite complementary. There is an asymmetry around a gantry angle of 0° that is most easily seen in the coronal slice SNR values (Figure 5.12). The asymmetry in SNR is accompanied by a geometric deformation of the phantom in the images taken at negative gantry angle. This suggests an uncompensated variation in B_0 inhomogeneity with gantry angle. A coil shift with the change in gantry angle can also explain the result, but no shifts were observed.

The isolation between all the channels is excellent both in terms of the bench measured transmission loss between channels Table 5.1 but also based on the cross-correlation of the noise images. With a peak correlation of about 5% each of the channels is contributing unique information and SNR is not being degraded by the presence of the other coils.

The B_1 maps (Figure 5.18) show that the phantom was excited fairly uniformly. Some distortion is evident near the coil, highlighting that the passive decoupling via crossed-diodes could be improved upon, but over the majority of the phantom volume, and hence the target area where high-SNR imaging would be needed during treatment, the flip angle is sufficiently uniform.

This coil arrangement achieves the objectives for use in the rotating B_0 linac-MR. The closest the SNR for the sum of all the channels and any individual channel come to one another is 10% (Coronal slice, 0°), but in general for most slices and at most gantry angles the wRSS combination outperforms any individual coil by at least 30%. The fairest comparison is to the octagonal coil which also doesn't vary with gantry angle and the array approaches double the SNR of the octagonal coil alone for nearly every gantry angle and slice.

5.5 Conclusions

The combination of a single turn coil with two orthogonally oriented butterflies is a clear choice for an out-of-field RF-coil array that can maintain consistent image quality over a 360° gantry rotation. The addition of the two butterflies improves the SNR by nearly 100% over that of the octagonal coil at most gantry angles. The SNR of the array was constant (<10% variation in transverse slice images) across the entire 180° gantry rotation tested, and the individual butterfly channels varied in their contribution sinusoidally, as expected.

The three channels of this planar array were very well decoupled on the bench, as was verified in noise correlation measurements. The array also shows uniform B_1 maps, acquired based on the double angle measurement, with limited distortion close to the array due to the limitations of passive detuning. The three channel planar array is an effective out-of-field RF-coil array for gantry angle independent imaging on a rotating B_0 linac-MR.

Chapter 6

Future Work

The findings in this work and their limitations are opportunities for future work. In addition to being an inspiration for more purpose built RF-coils for Linac-MR systems, the limitations seen in my work offer new avenues for investigating effects of other materials in a radiation beam, investigating lumped components in a radiation beam, measuring radiation induced current in surface coils, and modelling and measuring dose below custom built RF-coils in a Linac-MR.

Consider the designs explored in Chapter 3 and Chapter 4; this work paves the way for in-beam RF-coils on all Linac-MR systems, with either parallel or perpendicular magnetic field orientation. They also motivate expanded use of aluminum conductors in X-ray MRI [85] and PET-MRI [99] systems where radiation interactions are undesired. Offspring of these chapters are investigations of thin aluminum and copper conductor surface coil arrays in other contexts. Furthermore the research in this thesis is limited to exploration of copper and aluminum strips directly in the field. Other materials like graphene or silver paint [82, 83] may have applications, despite the clear limitations of much lower conductivity and higher electron density, respectively.

A major question that could not be answered in this work is what is the real trade off between sparing surface dose and degrading SNR with thinner or aluminum coils in the 0.5 T linac-MR. Work in this thesis was limited to delivering representative radiation in a 0.2T magnetic field and acquiring images at 0.5 T. It is known that the electron spectrum at the surface will be very different in a 0.5 T linac-MR than in the 0.2 T magnetic field used in Chapter 3. The Alberta Linac-MR system offers the ability to evaluate the surface dose and imaging capabilities simultaneously. In-beam RF-coils could be evaluated in terms of their surface dose effect and their achieved SNR, including the SNR differences seen with and without a radiation beam.

This study only investigated the effect of material on image quality in MR images. To avoid confounding effects, radiation was not delivered during imaging. This means that the imaging performance during treatment while using these coils will be degraded further by any additional noise sources whether external un-shielded RF-noise or radiation induced current (RIC) due to radiation striking the conductors[31, 35]. Investigations with coils for the 1.5 T MR-linac have shown less than 5% degradation of SNR in a 680 MU/min photon beam[31]. While this suggests that at 0.5 T the SNR reduction due to RIC will also be less than the up to 20% seen in measurements at 0.2 T[35], the effect also depends on the the RF-coil design and imaging sequences. This means specific investigations with surface coils at 0.5 T are warranted.

The work in Chapter 3 also raises the question that if conductors can be in the beam path, what about lumped components? Investigations of component reliability in a radiation beam, and their effect on surface dose is crucial for some surface array designs, especially at higher field strengths where more capacitive segmentation is required. This may motivate investigations of radiologically ”thin” capacitors.

It is also important to develop methods to model the dose impact of RF-coils. Whether doing a CT-sim without RF-coils, or doing an MR-sim where the coils are not visible in the image, there need to be effective ways to add RF-coils to treatment plans and their effect on treatment dose must be calculated accurately. This includes not only measured increases directly below a conductor, but also effects of oblique (relative to the coil) radiation delivery. Surface dose is challenging to measure and poorly simulated in standard treatment planning systems, thus the treatment planning aspect of in-beam RF-coils offers many opportunities for further research.

The gantry angle invariant coil array developed in Chapter 5 lays the ground work for a range of RF-coils for the rotating B_0-Linac MR. In addition to being used alone as an out of the radiation field head coil, an avenue for exploring the design further is to replace the single turn channel with a Helmholtz-like pair, where a second ring can be positioned at the lower edge of the radiation field[36]. This coil design has immediate application to clinical use as an improvement over a single turn planar coil above the head. In addition, the precise arrangement of butterfly coils and a loop coil can be scaled and repeated to form arrays of larger numbers of coils. These could be placed along the back or chest of a patient for body imaging or an array could be arranged to cover extremities.

Future work in RF-coil design for the Linac-MR will combine and expand the concepts explored here, build testable RF-coil array prototypes, and evaluate them for clinical use in terms of SNR and surface dose. Along the way additional questions will be answered, and I hope the data found in this thesis will be of guidance.

Chapter 7

Conclusions

The research in this thesis provides key findings that will be necessary for the development of dedicated RF-coils for linac-MR systems. It is one of the many steps towards true image-guided radiation therapy that will positively impact the lives of the many people battling cancer [2]. The Alberta Linac-MR system is a combination MRI and linac with huge potential thanks to its small (<5%) dosimetric perturbation when using multiple fields and large bore[12, 27]. A key aspect of advancing the Alberta Linac-MR to the clinical environment is the development of RF-coils that achieve the unique requirements of this system. The work in this thesis has specific applications to RF-coils for the Alberta Linac-MR and general applications for MRI used in combination with radiation therapy. It is my hope that this thesis will support future researches to explore a larger design space for RF-coils.

Chapters 3 and 4 give measurements of surface dose and SNR which may be applicable to RF-Coil design in Linac-MR systems. Chapter 3 describe the bolusing effects of conductors in the radiation beam with and without a magnetic field. While the measurements are specific to the magnetic field investigated, similar bolusing effects are expected in other systems, even in perpendicular arrangement Linac-MR systems. Future work is needed to elucidate the effect of the magnetic field on the electron spectrum, which will modify the surface dose impact of coils in the radiation beam. Because Chapter 3 suggests thinner conductors may be preferred in the beam, RF-coil designers for linac-MR systems will find Chapter 4 reassuring. Thin copper and aluminum conductors achieve reasonable SNR in comparison to the typically used thick copper conductors. Image quality has an almost threshold relationship with thickness of conductor, where material properties determine the location of the threshold. Above about one skin depth of conductor large changes in thickness yield small improvements in SNR and below that the fall-off with even small changes in thickness can be dramatic.

The gantry angle invariant coil array developed in Chapter 5 offers a solution to the novel challenge of RF signal detection in a rotating B_0 Linac-MR. The solution is built on well understood principles and shows that combining three orthogonal channels into an array works in practice as well as principle. The design is applicable as shown in this thesis and the identical arrangement of butterfly coils and a loop coil could also be used as one of many identical coil elements in an array similarly to the composite RF-coil triplets explored by Maunder et. al.[114]. In Chapter 5, the complementary sensitives of the double butterflies was specifically exploited for gantry angle independent imaging and the measurements show good balance between between the single turn and the double butterflies as well. This balance would provide consistent SNR with triplet position and orientation, as well as gantry angle, when the array is draped over a curved geometry.

This thesis provides some of the basic measurements that will be helpful to future work on RF-coils for the linac-MR. Principles in this work can be applied in RF-coil design for all MR-linacs with appropriate considerations. The findings in Chapter 3 and Chapter 4 should inspire further investigations into surface arrays for the MRgRT systems. This includes building realistic array designs, evaluating their surface dose impact and evaluating their imaging capabilities. These should also include specific investigations of the RIC impact which was not investigated in this thesis and specific investigations of how the magnetic field of clinical systems changes the electron spectrum at the RF-coil and hence changes its effect on surface dose. Furthermore, Chapter 5 should prompt investigation of three channel surface elements for surface-array designs that are gantry angle independent, as well as investigating clinical use of the design that was presented.

Bibliography

[1] Statistics Canada, “Table 13-10-0801-01 leading causes of death, total population (age standardization using 2011 population),” Statistics Canada, Tech. Rep., 2019. DOI: 10.25318/1310080101-eng.

[2] D. R. Brenner, A. Poirier, R. R. Woods, L. F. Ellison, J.-M. Billette, A. A. Demers, S. X. Zhang, C. Yao, C. Finley, N. Fitzgerald, N. Saint-Jacques, L. Shack, D. Turner, and E. Holmes, “Projected estimates of cancer in Canada in 2022,” *Canadian Medical Association Journal*, vol. 194, no. 17, E601 LP –E607, May 2022. DOI: 10.1503/cmaj.212097.

[3] Canadian Cancer Society, *What is cancer?* 2021. [Online]. Available: https://www.cancer.ca/en/cancer-information/cancer-101/what-is-cancer/?region=ab (visited on 01/21/2021).

[4] Canadian Cancer Statistics Advisory Committee, “Canadian cancer statistics 2019,” Canadian Cancer Society, Toronto, ON, Tech. Rep., 2019.

[5] R. García-Figueiras, S. Baleato-González, A. R. Padhani, A. Luna-Alcalá, J. A. Vallejo-Casas, E. Sala, J. C. Vilanova, D.-M. Koh, M. Herranz-Carnero, and H. A. Vargas, “How clinical imaging can assess cancer biology,” *Insights into Imaging*, vol. 10, no. 1, p. 28, 2019, ISSN: 1869-4101. DOI: 10.1186/s13244-019-0703-0.

[6] H. Chandarana, H. Wang, R. H. N. Tijssen, and I. J. Das, “Emerging role of MRI in radiation therapy,” *Journal of Magnetic Resonance Imaging*, vol. 48, no. 6, pp. 1468–1478, Dec. 2018, ISSN: 1522-2586. DOI: 10.1002/jmri.26271.

[7] L. Fass, “Imaging and cancer: a review,” *Molecular oncology*, vol. 2, no. 2, pp. 115–152, Aug. 2008, ISSN: 1878-0261. DOI: 10.1016/j.molonc.2008.04.001.

[8] M. A. Schmidt and G. S. Payne, “Radiotherapy planning using MRI,” *Physics in Medicine & Biology*, vol. 60, no. 22, R323, Oct. 2015, ISSN: 0031-9155. DOI: 10.1088/0031-9155/60/22/R323.

[9] S. Lim-Reinders, B. M. Keller, S. Al-Ward, A. Sahgal, and A. Kim, “Online Adaptive Radiation Therapy,” *International Journal of Radiation Oncology · Biology · Physics*, vol. 99, no. 4, pp. 994–1003, 2017, ISSN: 0360-3016. DOI: 10.1016/j.ijrobp.2017.04.023.

[10] M. D. den Hartogh, M. E. P. Philippens, I. E. van Dam, C. E. Kleynen, R. J. H. A. Tersteeg, R. M. Pijnappel, A. N. T. J. Kotte, H. M. Verkooijen, M. A. A. J. van den Bosch, M. van Vulpen, B. van Asselen, and H. J. G. D. van den Bongard, "MRI and CT imaging for preoperative target volume delineation in breast-conserving therapy," *Radiation Oncology*, vol. 9, no. 1, p. 63, 2014, ISSN: 1748-717X. DOI: 10.1186/1748-717X-9-63.

[11] M. T. Corkum, G. Morton, A. V. Louie, G. S. Bauman, L. C. Mendez, J. Chin, D. P. D'Souza, R. E. Dinniwell, V. M. Velker, R. Saskin, A. Warner, and G. B. Rodrigues, "Is prostate brachytherapy a dying art? trends and variation in the definitive management of prostate cancer in ontario, canada," *Radiotherapy and Oncology*, vol. 152, pp. 42–48, 2020, ISSN: 0167-8140. DOI: 10.1016/j.radonc.2020.07.036.

[12] B. G. Fallone, "The rotating biplanar linac–magnetic resonance imaging system," *Seminars in Radiation Oncology*, vol. 24, no. 3, pp. 200–202, Jul. 2014, ISSN: 1053-4296. DOI: 10.1016/J.SEMRADONC.2014.02.011.

[13] B. W. Raaymakers, J. J. Lagendijk, J Overweg, J. G. Kok, A. J. Raaijmakers, E. M. Kerkhof, R. W. Van Der Put, I Meijsing, S. P. Crijns, F Benedosso, M. Van Vulpen, C. H. De Graaff, J Allen, and K. J. Brown, "Integrating a 1.5 t mri scanner with a 6 mv accelerator: Proof of concept," *Physics in Medicine and Biology*, vol. 54, no. 12, N229–N237, Jun. 2009, ISSN: 00319155. DOI: 10.1088/0031-9155/54/12/N01.

[14] O. Heid, M. Kleemann, and J. Heller, "Integrated mri-linac radiotherapy machine," *Proc. Int Soc. Mag. Reson. Med.*, vol. 23, p. 3068, 2015.

[15] P. J. Keall, M. Barton, and S. Crozier, "The australian magnetic resonance imaging–linac program," *Seminars in Radiation Oncology*, vol. 24, no. 3, pp. 203–206, 2014, ISSN: 10534296. DOI: 10.1016/j.semradonc.2014.02.015.

[16] J. F. Dempsey, D Benoit, J. R. Fitzsimmons, A Haghighat, J. G. Li, D. A. Low, S Mutic, J. R. Palta, H. E. Romeijn, and G. E. Sjoden, "A device for realtime 3d image-guided imrt," *International Journal of Radiation Oncology Biology Physics*, vol. 63, S202, Sep. 2005, ISSN: 0360-3016. DOI: 10.1016/j.ijrobp.2005.07.349.

[17] B. M. Oborn, P. E. Metcalfe, M. J. Butson, A. B. Rosenfeld, and P. J. Keall, "Electron contamination modeling and skin dose in 6 mv longitudinal field mrigrt: Impact of the mri and mri fringe field," *Medical Physics*, vol. 39, no. 2, pp. 874–890, Jan. 2012, ISSN: 0094-2405. DOI: 10.1118/1.3676181.

[18] B. W. Raaymakers, A. J. Raaijmakers, A. N. Kotte, D Jette, and J. J. Lagendijk, "Integrating a mri scanner with a 6 mv radiotherapy accelerator: Dose deposition in a transverse magnetic field," *Physics in Medicine and Biology*, vol. 49, no. 17, pp. 4109–4118, Sep. 2004, ISSN: 00319155. DOI: 10.1088/0031-9155/49/17/019.

[19] J. St. Aubin, A. Keyvanloo, and B. G. Fallone, “Discontinuous finite element space-angle treatment of the first order linear boltzmann transport equation with magnetic fields: Application to mri-guided radiotherapy.,” *Medical physics*, vol. 43, no. 1, p. 195, Jan. 2016, ISSN: 0094-2405 (Print). DOI: 10.1118/1.4937933.

[20] M. Reynolds, B. G. Fallone, and S. Rathee, “Dose response of selected solid state detectors in applied homogeneous transverse and longitudinal magnetic fields,” *Medical Physics*, vol. 41, no. 9, p. 092 103, Aug. 2014, ISSN: 00942405. DOI: 10.1118/1.4893276.

[21] J. Yun, E. Yip, Z. Gabos, K. Wachowicz, S. Rathee, and B. G. Fallone, “Neural-network based autocontouring algorithm for intrafractional lung-tumor tracking using linac-mr.,” *Medical physics*, vol. 42, no. 5, pp. 2296–2310, May 2015, ISSN: 0094-2405 (Print). DOI: 10.1118/1.4916657.

[22] J. Yun, K. Wachowicz, M. Mackenzie, S. Rathee, D. Robinson, and B. G. Fallone, “First demonstration of intrafractional tumor-tracked irradiation using 2d phantom mr images on a prototype linac-mr.,” *Medical physics*, vol. 40, no. 5, p. 51 718, May 2013, ISSN: 0094-2405 (Print). DOI: 10.1118/1.4802735.

[23] S. Rathee, B. G. Fallone, and S. Steciw, “Technical Note: EPID’s response to 6 MV photons in a strong, parallel magnetic field.,” *Medical physics*, vol. 46, no. 1, pp. 340–344, Jan. 2019, ISSN: 2473-4209 (Electronic). DOI: 10.1002/mp.13285.

[24] U. Jelen, B. Dong, J. Begg, N. Roberts, B. Whelan, P. Keall, and G. Liney, *Dosimetric Optimization and Commissioning of a High Field Inline MRI-Linac*, 2020.

[25] S. Klüter, “Technical design and concept of a 0.35 T mr-linac,” *Clinical and Translational Radiation Oncology*, vol. 18, pp. 98–101, Sep. 2019, ISSN: 24056308. DOI: 10.1016/j.ctro.2019.04.007.

[26] N. Rammohan, J. W. Randall, and P. Yadav, “History of Technological Advancements towards MR-Linac: The Future of Image-Guided Radiotherapy,” *Journal of Clinical Medicine*, vol. 11, no. 16, 2022, ISSN: 2077-0383. DOI: 10.3390/jcm11164730.

[27] C. Kirkby, B. Murray, S. Rathee, and B. G. Fallone, “Lung dosimetry in a linac-mri radiotherapy unit with a longitudinal magnetic field,” *Medical Physics*, vol. 37, no. 9, pp. 4722–4732, Aug. 2010, ISSN: 00942405. DOI: 10.1118/1.3475942.

[28] G. P. Liney, B. Dong, J. Begg, P. Vial, K. Zhang, F. Lee, A. Walker, R. Rai, T. Causer, S. J. Alnaghy, B. M. Oborn, L. Holloway, P. Metcalfe, M. Barton, S. Crozier, and P. Keall, “Technical note: Experimental results from a prototype high-field inline mri-linac,” *Medical Physics*, vol. 43, no. 9, pp. 5188–5194, Sep. 2016, ISSN: 00942405. DOI: 10.1118/1.4961395.

[29] A. J. E. Raaijmakers, B. W. Raaymakers, and J. J. W. Lagendijk, “Integrating a mri scanner with a 6 mv radiotherapy accelerator: Dose increase at tissue–air interfaces in a lateral magnetic field due to returning electrons,” *Physics in Medicine and Biology*, vol. 50, no. 7, pp. 1363–1376, Apr. 2005, ISSN: 0031-9155. DOI: 10.1088/0031-9155/50/7/002.

[30] A. J. Raaijmakers, B. W. Raaymakers, S. Van Der Meer, and J. J. Lagendijk, “Integrating a mri scanner with a 6 mv radiotherapy accelerator: Impact of the surface orientation on the entrance and exit dose due to the transverse magnetic field,” *Physics in Medicine and Biology*, vol. 52, no. 4, pp. 929–939, Feb. 2007, ISSN: 00319155. DOI: 10.1088/0031-9155/52/4/005.

[31] S. J. Hoogcarspel, S. E. Zijlema, R. H. N. Tijssen, L. G. W. Kerkmeijer, I. M. Jürgenliemk-Schulz, J. J. W. Lagendijk, and B. W. Raaymakers, “Characterization of the first rf coil dedicated to 1.5 t mr guided radiotherapy,” *Physics in Medicine & Biology*, vol. 63, no. 2, p. 025 014, Jan. 2018, ISSN: 1361-6560. DOI: 10.1088/1361-6560/aaa303.

[32] S. J. Hoogcarspel, S. P. M. Crijns, J. J. W. Lagendijk, M. Van Vulpen, and B. W. Raaymakers, “The feasibility of using a conventional flexible rf coil for an online mr-guided radiotherapy treatment,” *Physics in Medicine and Biology*, vol. 58, no. 6, pp. 1925–1932, Mar. 2013, ISSN: 00319155. DOI: 10.1088/0031-9155/58/6/1925.

[33] A. Ghila, B. G. Fallone, and S. Rathee, “Influence of standard rf coil materials on surface and buildup dose from a 6 mv photon beam in magnetic field,” *Medical Physics*, vol. 43, no. 11, pp. 5808–5816, 2016.

[34] B. Burke, A. Ghila, B. G. Fallone, and S. Rathee, “Radiation induced current in the rf coils of integrated linac-mr systems: The effect of buildup and magnetic field,” *Medical Physics*, vol. 39, no. 8, pp. 5004–5014, 2012, ISSN: 00942405. DOI: 10.1118/1.4737097.

[35] B. Burke, K Wachowicz, B. G. Fallone, and S. Rathee, “Effect of radiation induced current on the quality of mr images in an integrated linac-mr system,” *Medical Physics*, vol. 39, no. 10, pp. 6139–6147, 2012, ISSN: 0094-2405. DOI: 10.1118/1.4752422.

[36] V. Volotovskyy, R. Barta, K. Wachowicz, N. De Zanche, and B. G. Fallone, “Circumventing radiation beam and rf-coil collisions in a rotating b0 linac-mr hybrid using a three-channel array,” in *Proceedings of the International Society for Magnetic Resonance in Medicine 27*, Montreal, QC, Canada, 2019, p. 1589.

[37] G. P. Liney, B. Dong, E. Weber, R. Rai, A. Destruel, R. Garcia-Alvarez, D. J. Manton, U. Jelen, K. Zhang, M. Barton, P. Keall, and S. Crozier, “Imaging performance of a dedicated radiation transparent rf coil on a 1.0 tesla inline mri-linac,” *Physics in Medicine and Biology*, vol. 63, no. 13, p. 5005, Jun. 2018, ISSN: 13616560. DOI: 10.1088/1361-6560/aac813.

[38] D. M. Pozar, *Microwave Engineering*, 3rd Edition. Hoboken, NJ: J. Wiley, 2005, p. 700, ISBN: 0471448788.

[39] F. Bloch, "Nuclear induction," *Phys. Rev.*, vol. 70, pp. 460–474, 7-8 Oct. 1946. DOI: 10.1103/PhysRev.70.460.

[40] J Mispelter, M Lupu, and A Briguet, *NMR probeheads for biophysical and biomedical experiments: Theoretical Principles and Practical Guidelines*, 2nd Edition. London: Imperial College Press, 2015, p. 750, ISBN: 978-1-84816-662-2.

[41] D. I. Hoult, "The principle of reciprocity in signal strength calculations—a mathematical guide," *Concepts in Magnetic Resonance*, vol. 12, no. 4, pp. 173–187, 2000, ISSN: 1043-7347. DOI: 10.1002/1099-0534.

[42] M. A. Bernstein, K. F. King, and X. J. O. E. Zhou, "Chapter 1 - Tools," in *Handbook of MRI Pulse Sequences*, M. A. Bernstein, K. F. King, and X. J. O. E. Zhou, Eds., Burlington: Academic Press, 2004, pp. 5–28, ISBN: 978-0-12-092861-3. DOI: 10.1016/B978-012092861-3/50004-2.

[43] B. Gruber, M. Froeling, T. Leiner, and D. W. J. Klomp, "Rf coils: A practical guide for nonphysicists.," *Journal of Magnetic Resonance Imaging*, vol. 48, no. 3, pp. 590–604, Jun. 2018, ISSN: 1522-2586 (Electronic). DOI: 10.1002/jmri.26187.

[44] K. Kose, "Physical and technical aspects of human magnetic resonance imaging: present status and 50 years historical review," *Advances in Physics: X*, vol. 6, no. 1, p. 1 885 310, Jan. 2021, ISSN: null. DOI: 10.1080/23746149.2021.1885310.

[45] M. J. E. Golay, "Field homogenizing coils for nuclear spin resonance instrumentation," *Review of Scientific Instruments*, vol. 29, no. 4, pp. 313–315, Jan. 1958, ISSN: 00346748. DOI: 10.1063/1.1716184.

[46] Q. Wang, "Hardware of MRI System," in *Nuclear Magnetic Resonance*, N. Khaneja, Ed., Rijeka: IntechOpen, 2019, ch. 1, Ch. 1, ISBN: 978-1-83880-420-6. DOI: 10.5772/intechopen.89132.

[47] M. V. Vaidya, C. M. Collins, D. K. Sodickson, R. Brown, G. C. Wiggins, and R. Lattanzi, "Dependence of b1- and b1+ field patterns of surface coils on the electrical properties of the sample and the mr operating frequency," *Concepts in Magnetic Resonance Part B: Magnetic Resonance Engineering*, vol. 46, no. 1, pp. 25–40, Feb. 2016, ISSN: 1552504X. DOI: 10.1002/cmr.b.21319.

[48] C. Coillot, E. Nativel, M. Zanca, and C. Goze-Bac, "The magnetic field homogeneity of coils by means of the space harmonics suppression of the current density distribution," *Journal of Sensors and Sensor Systems*, vol. 5, pp. 401–408, Nov. 2016. DOI: 10.5194/jsss-5-401-2016.

[49] R. Brown, Y.-C. N. Cheng, E. M. Haacke, M. R. Thompson, and R. Venkatesan, "One-Dimensional Fourier Imaging, κ-Space, and Gradient Echoes," in *Magnetic Resonance Imaging: Physical Principles and Sequence Design*, 2nd Edition, John Wiley & Sons, Ltd, 2014, ch. 9, pp. 141–164, ISBN: 9781118633953. DOI: 10.1002/9781118633953.ch9.

[50] R. Brown, Y.-C. N. Cheng, E. M. Haacke, M. R. Thompson, and R. Venkatesan, “Multi-dimensional fourier imaging and slice excitation,” in *Magnetic Resonance Imaging: Physical Principles and Sequence Design*, 2nd Edition. John Wiley & Sons, Ltd, 2014, ch. 10, pp. 165–206, ISBN: 9781118633953. DOI: 10.1002/9781118633953.ch10.

[51] R. Brown, Y.-C. N. Cheng, E. M. Haacke, M. R. Thompson, and R. Venkatesan, “Signal, contrast, and noise,” in *Magnetic Resonance Imaging: Physical Principles and Sequence Design*, 2nd Edition. John Wiley & Sons, Ltd, 2014, ch. 15, pp. 325–373, ISBN: 9781118633953. DOI: 10.1002/9781118633953.ch15.

[52] H. Nyquist, “Thermal agitation of electric charge in conductors,” *Phys. Rev.*, vol. 32, pp. 110–113, 1 Jul. 1928. DOI: 10.1103/PhysRev.32.110.

[53] W. A. Edelstein, G. H. Glover, C. J. Hardy, and R. W. Redington, “The intrinsic signal-to-noise ratio in nmr imaging.,” *Magnetic Resonance In Medicine*, vol. 3, no. 4, pp. 604–618, Aug. 1986, ISSN: 0740-3194.

[54] K. Wachowicz, N. De Zanche, E. Yip, V. Volotovskyy, and B. G. Fallone, “Cnr considerations for rapid real-time mri tumor tracking in radiotherapy hybrid devices: Effects of b0 field strength.,” *Medical Physics*, vol. 43, no. 8, p. 4903, Aug. 2016, ISSN: 2473-4209 (Electronic). DOI: 10.1118/1.4959542.

[55] J. Yun, E. Yip, K. Wachowicz, S. Rathee, M. Mackenzie, D. Robinson, and B. G. Fallone, “Evaluation of a lung tumor autocontouring algorithm for intrafractional tumor tracking using low-field MRI: a phantom study.,” *Medical physics*, vol. 39, no. 3, pp. 1481–1494, Mar. 2012, ISSN: 0094-2405 (Print). DOI: 10.1118/1.3685578.

[56] T. Magee, M. Shapiro, and D. Williams, “Comparison of High-Field-Strength Versus Low-Field-Strength MRI of the Shoulder,” *American Journal of Roentgenology*, vol. 181, no. 5, pp. 1211–1215, Nov. 2003, ISSN: 0361-803X. DOI: 10.2214/ajr.181.5.1811211.

[57] B. K. Rutt and D. H. Lee, “The impact of field strength on image quality in MRI,” *Journal of Magnetic Resonance Imaging*, vol. 6, no. 1, pp. 57–62, 1996. DOI: 10.1002/jmri.1880060111.

[58] Z. P. Liang and P. C. Lauterbur, “Image resolution, noise, and artifacts,” in *Principles of Magnetic Resonance Imaging: A Signal Processing Perspective*. 2000, ch. 8, pp. 233–290. DOI: 10.1109/9780470545652.ch8.

[59] NEMA, “Determination of signal-to-noise ratio (snr) in diagnostic magnetic resonance imaging,” National Electrical Manufacturers Association, Rosslyn, VA, Tech. Rep., 2001, pp. 1–15.

[60] B. Burke, B. G. Fallone, and S. Rathee, “Radiation induced currents in mri rf coils: Application to linac/mri integration.,” *Physics in medicine and biology*, vol. 55, no. 3, pp. 735–746, Feb. 2010, ISSN: 1361-6560. DOI: 10.1088/0031-9155/55/3/013.

[61] H. A. Haus, W. R. Atkinson, G. M. Branch, W. B. Davenport, W. H. Fonger, W. A. Harris, S. W. Harrison, W. W. Mcleod, E. K. Stodola, and T. E. Talpey, "Representation of noise in linear twoports," *Proceedings of the IRE*, vol. 48, no. 1, pp. 69–74, 1960. DOI: 10.1109/JRPROC.1960.287381.

[62] C. H. Cunningham, J. M. Pauly, and K. S. Nayak, "Saturated double-angle method for rapid b1+ mapping," *Magnetic Resonance in Medicine*, vol. 55, no. 6, pp. 1326–1333, 2006. DOI: 10.1002/mrm.20896.

[63] J. P. Hornak, J. Szumowski, and R. G. Bryant, "Magnetic field mapping," *Magnetic Resonance in Medicine*, vol. 6, no. 2, pp. 158–163, 1988. DOI: 10.1002/mrm.1910060204.

[64] N. De Zanche, A. Maunder, T. Charlton, K. Wachowicz, and B. G. Fallone, "A unified framework for snr comparisons of four array image combination methods," in *Proceedings of the International Society for Magnetic Resonance in Medicine 19*, Montreal, 2011, p. 4659.

[65] P. B. Roemer, W. A. Edelstein, C. E. Hayes, S. P. Souza, and O. M. Mueller, "The nmr phased array," *Magnetic Resonance in Medicine*, vol. 16, no. 2, pp. 192–225, Nov. 1990, ISSN: 15222594. DOI: 10.1002/mrm.1910160203.

[66] C. Karzmark and R. J. Morton, *A Primer on Theory and Operation of Linear Accelerators in Radiation Therapy*, Third Edit, J. Lamb, Ed. Madison, Wisconsin: Medical Physics Publishing, Inc., 2017, p. 36, ISBN: 978-1-930524-97-2.

[67] W. Strydom, W. Parker, and M. Olivares, "Chapter 8: Electron beams: Physical and clinical aspects," in *Radiation Oncology Physics: A Handbook for Teachers and Students*, E. B. Podgorsak, Ed., Vienna, Austria: International Atomic Energy Agency, 2005, ch. 8, pp. 273–299, ISBN: 92-0-107304-6.

[68] E. B. Podgorsak, "Chapter 1: Basic radiation physics," in *Radiation Oncology Physics: A Handbook for Teachers and Students*, E. B. Podgorsak, Ed., Vienna, Austria: International Atomic Energy Agency, 2005, ch. Chapter 1, pp. 1–100.

[69] M. J. Berger and S. M. Seltzer, "Stopping powers and ranges of electrons and positrons," *Vol NBSIR 82-2550*, pp. 1–162, 1982. DOI: 10.6028/NBS.IR.82-2550A.

[70] M. J. Berger, J. H. Hubbell, S. M. Seltzer, J Chang, J. S. Coursey, R Sukumar, and D. S. Zucker, "XCOM: photon cross sections database," *NIST Standard Reference Database*, vol. 8, pp. 87–3597, 1998.

[71] O. Klein and Y. Nishina, "Über die Streuung von Strahlung durch freie Elektronen nach der neuen relativistischen Quantendynamik von Dirac," *Zeitschrift für Physik*, vol. 52, no. 11, pp. 853–868, Jul. 1929. DOI: 10.1007/BF01366453.

[72] J. H. Hubbell and S. M. Seltzer, "Cross section data for electron–positron pair production by photons: A status report," *Nuclear Instruments and Methods in Physics Research Section B: Beam Interactions with Materials and Atoms*, vol. 213, pp. 1–9, 2004, ISSN: 0168-583X. DOI: 10.1016/S0168-583X(03)01524-6.

[73] E. B. Podgorsak, "Chapter 2: Dosimetric principles, quantities, and units," in *Radiation Oncology Physics: A Handbook for Teachers and Students*, E. B. Podgorsak, Ed., Vienna, Austria: International Atomic Energy Agency, 2005, ch. Chapter 2, pp. 1–100.

[74] E. B. Podgorsak, "Chapter 6: External photon beams: Physical aspects," in *Radiation Oncology Physics: A Handbook for Teachers and Students*, E. B. Podgorsak, Ed., Vienna, Austria: International Atomic Energy Agency, 2005, ch. 6, pp. 161–218, ISBN: 92-0-107304-6.

[75] E. B. Podgorsak, "Chapter 3: Radiation dosimeters," in *Radiation Oncology Physics: A Handbook for Teachers and Students*, E. B. Podgorsak, Ed., Vienna, Austria: International Atomic Energy Agency, 2005, ch. Chapter 3, pp. 1–100.

[76] P. D. Higgins, C. H. Sibata, F. H. Attix, and B. R. Paliwal, "Calculational methods for estimating skin dose from electrons in Co 60 gamma ray beams," *Medical Physics*, vol. 10, no. 5, pp. 622–627, Sep. 1983, ISSN: 00942405. DOI: 10.1118/1.595332.

[77] F. N. Bray, B. J. Simmons, A. H. Wolfson, and K. Nouri, "Acute and chronic cutaneous reactions to ionizing radiation therapy.," *Dermatology and therapy*, vol. 6, no. 2, pp. 185–206, Jun. 2016, ISSN: 2193-8210. DOI: 10.1007/s13555-016-0120-y.

[78] A. Ghila, S. Steciw, B. G. Fallone, and S. Rathee, "Experimental verification of egsnrc monte carlo calculated depth doses within a realistic parallel magnetic field in a polystyrene phantom," *Medical Physics*, vol. 44, no. 9, pp. 4804–4815, 2017, ISSN: 0094-2405. DOI: 10.1002/mp.12413.

[79] B. M. Oborn, S Kolling, P. E. Metcalfe, S Crozier, D. W. Litzenberg, and P. J. Keall, "Electron contamination modeling and reduction in a 1 t open bore inline mri-linac system," *Medical Physics*, vol. 41, no. 5, p. 51 708, 2014, ISSN: 0094-2405. DOI: 10.1118/1.4871618.

[80] N. F. Roberts, E. Patterson, U. Jelen, T. Causer, L. Holloway, G. Liney, M. Lerch, A. B. Rosenfeld, D. Cutajar, B. M. Oborn, and P. Metcalfe, "Experimental characterization of magnetically focused electron contamination at the surface of a high-field inline mri-linac," *Medical Physics*, vol. 46, no. 12, pp. 5780–5789, 2019, ISSN: 0094-2405. DOI: 10.1002/mp.13847.

[81] H. E. Johns and J. R. Cunningham, *The Physics of Radiology*, 4th Edition. Springfield, IL: Charles C. Thomas, 1983, ISBN: 978-0398046699.

[82] J. R. Corea, A. M. Flynn, B. Lechêne, G. Scott, G. D. Reed, P. J. Shin, M. Lustig, and A. C. Arias, "Screen-printed flexible mri receive coils," *Nature Communications*, vol. 7, p. 10 839, Mar. 2016, ISSN: 2041-1723. DOI: 10.1038/ncomms10839.

[83] J. R. Corea, P. B. Lechene, M. Lustig, and A. C. Arias, "Materials and methods for higher performance screen-printed flexible mri receive coils.," *Magnetic resonance in medicine*, vol. 78, no. 2, pp. 775–783, Sep. 2017, ISSN: 1522-2594 (Electronic). DOI: 10.1002/mrm.26399.

[84] R. Barta, A. Ghila, S. Rathee, B Fallone, and N. De Zanche, "Low-attenuation rf surface coils for linac-mr hybrids: Compromise between radiation dose to the skin and snr," in *Proc. Intl. Soc. Mag. Reson. Med 25*, Honolulu, HI, USA: ISMRM, 2017, p. 4435.

[85] V. Rieke, A. Ganguly, B. L. Daniel, G. Scott, J. M. Pauly, R. Fahrig, N. J. Pelc, and K. Butts, "X-ray compatible radiofrequency coil for magnetic resonance imaging," *Magnetic Resonance in Medicine*, vol. 53, no. 6, pp. 1409–1414, 2005, ISSN: 07403194. DOI: 10.1002/mrm.20494.

[86] R. C. Aster, B. Borchers, and C. H. Thurber, *Parameter estimation and inverse problems.* 2nd Edition. Academic Press, 2013, p. 360, ISBN: 0123850487.

[87] J. R. Rumble, D. R. Lide, and T. J. Bruno, *CRC handbook of chemistry and physics : a ready-reference book of chemical and physical data.* ISBN: 9781138561632.

[88] P. Oliver, E. Yip, M. Reynolds, B. Burke, G. Fallone, B. Murray, D. Sinn, K. Wachowicz, B. Warkentin, and S. Y. Tari, "Skin dose investigations on a 0.5 T inline rotating biplanar linac-MR," *Medical Physics*, vol. 49, no. 8, p. 5628, 2022.

[89] R. A. Serway and J. W. Jewett, *Physics for scientists and engineers.* 6th Edition. Thomson-Brooks/Cole, 2004, ISBN: 9780534408428.

[90] D. I. Hoult and R. E. Richards, "The signal-to-noise ratio of the nuclear magnetic resonance experiment," *Journal of Magnetic Resonance (1969)*, vol. 24, no. 1, pp. 71–85, Oct. 1976, ISSN: 00222364. DOI: 10.1016/0022-2364(76)90233-X.

[91] G. Giovannetti, R. Francesconi, L. Landini, M. F. Santarelli, V. Positano, V. Viti, and A. Benassi, "Conductor geometry and capacitor quality for performance optimization of low-frequency birdcage coils," *Concepts in Magnetic Resonance Part B: Magnetic Resonance Engineering*, vol. 20B, no. 1, pp. 9–16, 2004, ISSN: 1552-504X. DOI: 10.1002/cmr.b.20005.

[92] B. Gruber, R. Rehner, E. Laistler, and S. Zink, "Anatomically adaptive coils for mri—a 6-channel array for knee imaging at 1.5 tesla," *Frontiers in Physics*, vol. 8, p. 80, 2020, ISSN: 2296-424X. DOI: 10.3389/fphy.2020.00080.

[93] J. M. Vincent and J. V. Rispoli, "Conductive thread-based stretchable and flexible radiofrequency coils for magnetic resonance imaging," *IEEE Transactions on Biomedical Engineering*, vol. 67, no. 8, pp. 2187–2193, Aug. 2020, ISSN: 1558-2531. DOI: 10.1109/TBME.2019.2956682.

[94] D. Zhang and Y. Rahmat-Samii, "A novel flexible electrotextile 3t mri rf coil array for carotid artery imaging: Design, characterization, and prototyping," *IEEE Transactions on Antennas and Propagation*, vol. 67, no. 8, pp. 5115–5125, Aug. 2019, ISSN: 1558-2221. DOI: 10.1109/TAP.2019.2891700.

[95] A. Port, R. Luechinger, D. O. Brunner, and K. P. Pruessmann, "Conductive elastomer for wearable rf coils," in *Proc. Intl. Soc. Mag. Reson. Med 26*, Virtual Conference, 2020, p. 1137.

[96] A. Mehmann, M. Varga, C. Vogt, A. Port, J. Reber, J. Marjanovic, K. P. Pruessmann, and G. Tröster, "On the bending and stretching of liquid metal receive coils for magnetic resonance imaging," *IEEE Transactions on Biomedical Engineering*, vol. 66, no. 6, pp. 1542–1548, 2019, ISSN: 1558-2531 VO - 66. DOI: 10.1109/TBME.2018.2875436.

[97] J. A. Malko, E. C. McClees, I. F. Braun, P. C. Davis, and J. C. Hoffman, "A flexible mercury-filled surface coil for mr imaging," *American Journal of Neuroradiology*, vol. 7, no. 2, pp. 246–247, 1986, ISSN: 01956108.

[98] J. A. Nordmeyer-Massner, N. De Zanche, and K. P. Pruessmann, "Stretchable coil arrays: Application to knee imaging under varying flexion angles," *Magnetic Resonance in Medicine*, vol. 67, no. 3, pp. 872–879, 2012, ISSN: 0740-3194. DOI: 10.1002/mrm.23240.

[99] C. Y. Sander, B. Keil, D. B. Chonde, B. R. Rosen, C. Catana, and L. L. Wald, "A 31-channel mr brain array coil compatible with positron emission tomography.," *Magnetic resonance in medicine*, vol. 73, no. 6, pp. 2363–2375, Jun. 2015, ISSN: 1522-2594 (Electronic). DOI: 10.1002/mrm.25335.

[100] R. Barta, A. Ghila, S. Rathee, B. G. Fallone, and N. De Zanche, "Impact of a parallel magnetic field on radiation dose beneath thin copper and aluminum foils," *Biomedical Physics & Engineering Express*, vol. 6, p. 037 002, 2020, ISSN: 2057-1976. DOI: 10.1088/2057-1976/ab7cf2.

[101] G. Giovannetti, V. Hartwig, L. Landini, and M. F. Santarelli, "Classical and lateral skin effect contributions estimation in strip mr coils," *Concepts in Magnetic Resonance Part B: Magnetic Resonance Engineering*, vol. 41 B, no. 2, pp. 57–61, Apr. 2012, ISSN: 15525031. DOI: 10.1002/cmr.b.21210.

[102] G. Giovannetti, N. Fontana, A. Monorchio, M. Tosetti, and G. Tiberi, "Estimation of losses in strip and circular wire conductors of radiofrequency planar surface coil by using the finite element method," *Concepts in Magnetic Resonance Part B: Magnetic Resonance Engineering*, vol. 47B, no. 3, e21358, 2017, ISSN: 1552-5031. DOI: 10.1002/cmr.b.21358.

[103] C.-n. Chen and D. I. Hoult, *Biomedical magnetic resonance technology.* Bristol: A. Hilger, 1989, ISBN: 0852741189.

[104] J. M. Park, H.-G. Wu, H. J. Kim, C. H. Choi, and J.-I. Kim, "Comparison of treatment plans between imrt with mr-linac and vmat for lung sabr.," *Radiation oncology (London, England)*, vol. 14, no. 1, p. 105, Jun. 2019, ISSN: 1748-717X. DOI: 10.1186/s13014-019-1314-0.

[105] H. E. Bainbridge, M. J. Menten, M. F. Fast, S. Nill, U. Oelfke, and F. McDonald, "Treating locally advanced lung cancer with a 1.5T MR-Linac – Effects of the magnetic field and irradiation geometry on conventionally fractionated and isotoxic dose-escalated radiotherapy," *Radiotherapy and Oncology*, vol. 125, no. 2, pp. 280–285, 2017, ISSN: 0167-8140. DOI: 10.1016/j.radonc.2017.09.009.

[106] B. W. Raaymakers, I. M. Jürgenliemk-Schulz, G. H. Bol, M Glitzner, A. N. T. J. Kotte, B van Asselen, J. C. J. de Boer, J. J. Bluemink, S. L. Hackett, M. A. Moerland, S. J. Woodings, J. W. H. Wolthaus, H. M. van Zijp, M. E. P. Philippens, R Tijssen, J. G. M. Kok, E. N. de Groot-van Breugel, I Kiekebosch, L. T. C. Meijers, C. N. Nomden, G. G. Sikkes, P. A. H. Doornaert, W. S. C. Eppinga, N Kasperts, L. G. W. Kerkmeijer, J. H. A. Tersteeg, K. J. Brown, B Pais, P Woodhead, and J. J. W. Lagendijk, "First patients treated with a 1.5 t mri-linac: Clinical proof of concept of a high-precision, high-field mri guided radiotherapy treatment.," *Physics in medicine and biology*, vol. 62, no. 23, pp. L41–L50, Nov. 2017, ISSN: 1361-6560 (Electronic). DOI: 10.1088/1361-6560/aa9517.

[107] P. Bottomley and C. J. Hardy, "4973908 NMR probe with multiple isolated coplanar surface coils," *Magnetic Resonance Imaging*, vol. 10, no. 4, p. V, 1992, ISSN: 0730725X. DOI: 10.1016/0730-725x(92)90044-z.

[108] J. Chacon-Caldera, M. Malzacher, and L. R. Schad, "Partially orthogonal resonators for magnetic resonance imaging," *Scientific Reports*, vol. 7, no. 1, p. 42 347, 2017, ISSN: 2045-2322. DOI: 10.1038/srep42347.

[109] J. Chacon-Caldera, A. Fischer, M. Malzacher, Y. Vetter, M. Davids, M. Flöser, C. Stumpf, and L. R. Schad, "Evaluation of stacked resonators to enhance the performance of a surface receive-only array for prostate mri at 3 tesla," *Magnetic Resonance Imaging*, vol. 53, pp. 164–172, Nov. 2018, ISSN: 18735894. DOI: 10.1016/j.mri.2018.07.010.

[110] M. A. Ohliger, R. L. Greenman, R. Giaquinto, C. A. McKenzie, G. Wiggins, and D. K. Sodickson, "Concentric coil arrays for parallel mri," *Magnetic Resonance in Medicine*, vol. 54, no. 5, pp. 1248–1260, 2005. DOI: 10.1002/mrm.20647.

[111] Z. J. Wang, "Improving snr of rf coils using composite coil elements," *NMR in Biomedicine*, vol. 22, no. 9, pp. 952–959, 2009. DOI: 10.1002/nbm.1410.

[112] Y.-H. Chu, Y.-C. Hsu, B. Keil, W.-J. Kuo, and F.-H. Lin, "A 32-channel head coil array with circularly symmetric geometry for accelerated human brain imaging," *PLOS ONE*, vol. 11, no. 2, pp. 1–13, Feb. 2016. DOI: 10.1371/journal.pone.0149446.

[113] A. Kumar and P. A. Bottomley, "Optimized quadrature surface coil designs," *Magnetic Resonance Materials in Physics, Biology and Medicine*, vol. 21, no. 1-2, pp. 41–52, Mar. 2008, ISSN: 09685243. DOI: 10.1007/s10334-007-0090-2.

[114] A. Maunder, B. G. Fallone, M. Daneshmand, and N. De Zanche, "Experimental verification of snr and parallel imaging improvements using composite arrays," *NMR in Biomedicine*, vol. 28, no. 2, pp. 141–153, Feb. 2015, ISSN: 10991492. DOI: 10.1002/nbm.3230.